Exploring the Peroxidase Activity of Ferriprotoporphyrin IX: Towards Understanding its Cytotoxicity in the Malaria Parasite

by

Wikus Bergh

Thesis presented in partial fulfilment of the requirements for the degree of Master of Science (Biochemistry) in the Faculty of Science at Stellenbosch University

Department of Chemistry,
University of Stellenbosch,
Private Bag X1, Matieland 7602, South Africa.

Supervisor: Dr. K.A. de Villiers
Co-supervisor: Dr. W.J. Gerber

April 2019

Declaration

By submitting this thesis electronically, I declare that the entirety of the work contained therein is my own, original work, that I am the sole author thereof (save to the extent explicitly otherwise stated), that reproduction and publication thereof by Stellenbosch University will not infringe any third party rights and that I have not previously in its entirety or in part submitted it for obtaining any qualification.

Wikus Bergh

Date: 20/12/2018

Abstract

The peroxidase reaction, catalysed by ferriprotoporphyrin IX (Fe(III)PPIX), was selected as a model reaction by which to explore Fe(III)PPIX toxicity via the formation of reactive oxygen species. This has direct relevant in, for example, antimalarial chemotherapy. To analyse potential reaction steps, model-based analysis is used. A program was coded incorporating a simplex algorithm for the multivariate global analysis of experimental data using non-linear least squares (NLLS) regression analysis. The reaction between Fe(III)PPIX and hydrogen peroxide was studied, with tests conducted regarding reversibility of proposed reaction steps, as well as the addition of potential side reactions. NLLS regression analysis of proposed models yielded fitted data that could be used to determine the goodness-of-fit of the model, as well as compare fits of models as a function of their complexity. Model comparison analysis showed that reversibility of reactions were irrelevant, and that the best depiction of the reaction proceeds via three steps. The first is complexation of Fe(III)PPIX and H_2O_2. Secondly, the complex forms an active intermediate *I*. The last step is denoted by the conversion of the intermediate to $Fe^{\bullet+}$(IV)PPIX=O. Degradation of $Fe^{\bullet+}$(IV)PPIX=O was incorporated in model extensions as side reaction but did not form part of the model determined to be best.

ABTS is used as chromogen to follow the peroxidase-like reaction of Fe(III)PPIX spectrophotometrically. Studies conducted on plausible side reactions of the chromogen ABTS showed that the compound does not react with hydrogen peroxide at pH levels of 4.8 and 7.5. The disproportionation reaction is shown to occur under highly acidic conditions but is concluded not to transpire at pH levels approaching physiologically relevant conditions. Degradation of ABTS is not observed for physiologically relevant conditions. $ABTS^{\bullet+}$ degradation is considered a viable side reaction under the premise that it can be reduced to a null parameter following non-linear least squares regression in the case that it does not prove relevant.

Results obtained for the reaction between Fe(III)PPIX and H_2O_2 and ABTS studies are incorporated in the proposition of plausible reaction models for the peroxidase-like reaction of Fe(III)PPIX. NLLS analysis of models presented based on literary review indicate that the peroxidase-like activity of Fe(III)PPIX involves two parallel catalytic cycles. One involves the reaction steps presented for the reaction of Fe(III)PPIX with H_2O_2. From the formation of $Fe^{\bullet+}$(IV)PPIX=O, the radical porphyrin compound can react with ABTS to form Fe(IV)PPIX=O and $ABTS^{\bullet+}$. Fe(IV)PPIX=O can react with another molecule of ABTS to form $ABTS^{\bullet+}$ and regenerate Fe(III)PPIX, thus concluding the cycle. The second catalytic cycle is initiated by the complexation of Fe(III)PPIX with ABTS. The complex formed can react with H_2O_2 to produce a $Fe^{\bullet+}$(IV)PPIX=O.ABTS complex. The porphyrin radical compound

can react with the ABTS molecule associated to it to produce $ABTS^{\bullet+}$ and Fe(IV)PPIX=O, thus joining into the first cycle presented.

The model proposed can be used to compare the kinetics of this reaction in the presence of antimalarial compounds to elicit the effect these compounds have on the toxicity of Fe(III)PPIX; such insights may advance rational design efforts towards new antimalarial chemotherapeutics.

Uittreksel

Die peroksidase reaksie, gekataliseer deur ferriprotoporfirien IX (Fe(III)PPIX), was gekies as ‘n model reaksie om die toksisiteit van Fe(III)PPIX wat reaktiewe suurstof spesies form te bestudeer. Hierdie is direk relevant vir byvoorbeeld antimalariese chemoterapie. Om potensiele reaksie stappe te analiseer is model-gebaseerde analise gebruik. ‘n Program was gekodeer wat ‘n simpleks algoritme inkorporeer vir die multivariate globale analise van experimentele data deur gebruik te maak van nie-lineêre kleinste vierkant regressie analise (NLKV). Die reaksie tussen Fe(III)PPIX en waterstof peroksied was bestudeer, met toetse wat die omkeerbaarheid van die voorgestelde reaksie stappe sowel as potensiele sy-reaksies in ag te neem. NLKV regressie analise van die voorgestelde modelle was gebruik om te bepaal hoe goed die model pas, asook om die passing van die model tot sy kompleksiteit te vergelyk. Model vergelykings analise het die omkeerbaarheid van sekere reaksies as irrelevant aangetoon, en verder gewys dat die beste beskrywing van die kinetiese reaksies volgens drie stappe plaasvind. Die eerste reaksie betrek die kompleksasie van Fe(III)PPIX en H_2O_2. Tweedens form die kompleks ‘n aktiewe intermediêre spesies, *I*. Die laaste stap word aangetoon deur die omskakeling van die intermediêre spesies na $Fe^{\bullet+}$(IV)PPIX=O. Degredasie van $Fe^{\bullet+}$(IV)PPIX=O was in model verlengings geinkorporeer as sy-reaksies, maar het nie deel gevorm van die model meganisme wat die beste passings toon nie.

ABTS word as chromogeen gebruik om die peroksidase-tipe reaksie van Fe(III)PPIX spektrofotometries te bestudeer. Studies gedoen om die moontlike reaksies van die chromogeen ABTS te bepaal wys dat die verbinding nie met H_2O_2 reageer by pH vlakke van 4.8 en 7.5 nie. Die disproporsionasie reaksie vind net plaas onder hoogs suur kondisies en dus nie by pH vlakke naby aan fisiologiese relevante kondisies nie. Degredasie van ABTS is nie waargeneem by fisiologiese relevante kondisies nie. $ABTS^{\bullet+}$ degredasie is oorweeg as ‘n potensiêle reaksie onder die premie dat dit gereduseer kan word tot ‘n nul parameter tydens die NLKV regressie analise van voorgestelde modelle in die geval wat die reaksie nie relevant is nie.

Resultate verkryg vir die reaksies tussen Fe(III)PPIX en H_2O_2 asook ABTS studies is geinkorporeer in die voorstelling van moontlike reaksie modelle vir die peroksidase-tipe aktiwiteit van Fe(III)PPIX. NLKV regressie analise van modelle gebaseer op literatuur wys dat die peroksidasie-tipe aktiwiteit van Fe(III)PPIX twee paralelle katalitiese siklusse bevat. Die hoof siklus bevat die reaksie stappe soos bepaal vir die reaksie van Fe(III)PPIX met H_2O_2. Die gevormde van $Fe^{\bullet+}$(IV)PPIX=O radikale porfirien verbinding reageer dan met ABTS om Fe(IV)PPIX=O en $ABTS^{\bullet+}$ te vorm. Fe(IV)PPIX=O kan ook reageer met nog ‘n molekule van ABTS om $ABTS^{\bullet+}$ te vorm en Fe(III)PPIX te hergenereer, en so die eerste siklus te voltooi. Die tweede katalitiese siklus word geinisieer deur die kompleksasie van Fe(III)PPIX met ABTS. Die gevormde kompleks kan met waterstofperoksied reageer om ‘n $Fe^{\bullet+}$(IV)PPIX=O.ABTS kompleks te produseer. Die porfirien radikaal verbinding kan met die ABTS

molekule aan hom verbind reageer om $ABTS^{\bullet+}$ en Fe(IV)PPIX=O te produseer, en dus by die hoof siklus aan te sluit.

Die voorgestelde model kan gebruik word om die kinetika van die reaksies in die teenwoordigheid van antimalariese dwelms te vergelyk, sodat die effek van hierdie dwelms op die toksisiteit van Fe(III)PPIX ontleed kan word. Sulke insigte mag dalk help in die rasionele ontwikkeling van nuwe antimalariese middels.

Acknowledgements

I would like to express my gratitude to the following people, groups and organizations;

1. My project supervisor Dr. Katherine de Villiers for your continued support and inset

2. My project co-supervisor Dr. Wilhelm Gerber for inset on the kinetic analysis and encouragement

3. Ms. Chandre Sammy for the kinetic data used in the peroxidase-like activity of haem, and your assistance with laboratory procedures

4. The Haem Team for support

5. The National Research Fund (NRF) for funding this project

6. My parent for their constant love and encouragement

List of Abbreviations

ABTS	2,2'-azino-di(3-ethylbenztiazoline sulphonic acid-6)
AIC	Akaike information criterion
BIC	Bayesian information criterion
BPR	Bromopyrogallol red
D	Degradation products
DMSO	dimethyl sulfoxide
eIF-2	Eukaryotic initiation factor-2
ELISA	Enzyme-linked immunosorbent assay
Fe(II)PPIX	Haem
Fe(III)PPIX	Haematin
Fe(IV)PPIX=O	Oxidised haematin
Fe+(IV)PPIX=O	Radical haematin
H2O2	Hydrogen peroxide
HAP1	Heme-activating protein 1
HDP	Haem detoxification protein
HNO3	Nitric acid
HO	Haem oxygenase
HRI	Human eukaryotic translaton initiation factor 2-alpha kinase 1
HRP	Horseradish peroxidase
HRP	Histidine rich protein
I	Reactive intermediate
KLD	Kullback-Leibler Divergence
KMnO4	Potassium permanganate
MnO4-	Permanganate ion
NF-E2	Nuclear factor-erythroid-2
NLLS	Non-linear least squares

ODE	Ordinary differential equation
ODS	*o*-Dianisidine
OPD	*o*-Phenylenediamine
pfcrt	*Plasmodium falciparum* chloroquine resistance transporter gene
pfmdr1	*Plasmodium falciparum* multidrug resistance gene 1
PG	pyrogallol
ROS	Reactive oxidative species
rRMS	Relative residual sum of squares
SCF	Self-consistent field
SSQ	Sum of squares
TMB	3,3',5,5'-tetramethylbenzidine
WHO	World Health Organization

Conference proceedings

SACI Inorganic Chemistry Conference 2017, Arabella Hotel, Hermanus, RSA, **Poster Presentation:** Wikus Bergh, Dr Wilhelm J Gerber and Dr Katherine A. de Villiers, The Cytotoxicity of Iron(III) Protoporphyrin IX in the Presence of Antimalarial Compounds.

Table of Contents

List of Figures

deviance. From A to J, the experimental data were collected for Fe(III)PPIX at a concentration of 10 µM, and H_2O_2 at 40, 60, 80, 100, 150, 200, 300, 800, 1000 and 2000 µM

Figure 3.6: The theoretical and experimental absorbance of the reaction of H_2O_2 with Fe(III)PPIX. The sub model analysed is 2(ir)_original. Residual plots are presented as insets to allow for inspection of model deviance. From A to J, the experimental data were collected for Fe(III)PPIX at a concentration of 10 µM, and H_2O_2 at 40, 60, 80, 100, 150, 200, 300, 800, 1000 and 2000 µM.

Figure 3.7: The theoretical and experimental absorbance of the reaction of H_2O_2 with Fe(III)PPIX. The sub model analysed is 2(r)_original. Residual plots are presented as insets to allow for inspection of model deviance. From A to J, the experimental data were collected for Fe(III)PPIX at a concentration of 10 µM, and H_2O_2 at 40, 60, 80, 100, 150, 200, 300, 800, 1000 and 2000 µM.

Figure 3.8: The theoretical and experimental absorbance of the reaction of H_2O_2 with Fe(III)PPIX. The sub model analysed is 2(ir)_rad. Residual plots are presented as insets to allow for inspection of model deviance. From A to J, the experimental data were collected for Fe(III)PPIX at a concentration of 10 µM, and H_2O_2 at 40, 60, 80, 100, 150, 200, 300, 800, 1000 and 2000 µM.

Figure 3.9: The theoretical and experimental absorbance of the reaction of H_2O_2 with Fe(III)PPIX. The sub model analysed is 2(r)_rad. Residual plots are presented as insets to allow for inspection of model deviance. From A to J, the experimental data were collected for Fe(III)PPIX at a concentration of 10 µM, and H_2O_2 at 40, 60, 80, 100, 150, 200, 300, 800, 1000 and 2000 µM.

Figure 3.10: The theoretical and experimental absorbance of the reaction of H_2O_2 with Fe(III)PPIX. The sub model analysed is 3(ir)_original. Residual plots are presented as insets to allow for inspection of model deviance. From A to J, the experimental data were collected for Fe(III)PPIX at a concentration of 10 µM, and H_2O_2 at 40, 60, 80, 100, 150, 200, 300, 800, 1000 and 2000 µM.

Figure 3.11: The theoretical and experimental absorbance of the reaction of H_2O_2 with Fe(III)PPIX. The sub model analysed is 3(r)_original. Residual plots are presented as insets to allow for inspection of model deviance. From A to J, the experimental data were collected for Fe(III)PPIX at a concentration of 10 µM, and H_2O_2 at 40, 60, 80, 100, 150, 200, 300, 800, 1000 and 2000 µM.

Figure 3.12: The theoretical and experimental absorbance of the reaction of H_2O_2 with Fe(III)PPIX. The sub model analysed is 3(ir)_rad. Residual plots are presented as insets to allow for inspection of model deviance. From A to J, the experimental data were collected for Fe(III)PPIX at a concentration of 10 µM, and H_2O_2 at 40, 60, 80, 100, 150, 200, 300, 800, 1000 and 2000 µM.

Figure 3.13: The theoretical and experimental absorbance of the reaction of H_2O_2 with Fe(III)PPIX. The sub model analysed is 3(r)_rad. Residual plots are presented as insets to allow for inspection of model deviance. From A to J, the experimental data were collected for Fe(III)PPIX at a concentration of 10 µM, and H_2O_2 at 40, 60, 80, 100, 150, 200, 300, 800, 1000 and 2000 µM.

Figure 4.1: The reaction between ABTS and hydrogen peroxide. Multiple spectra measurements between 250 and 700 nm were collected as a function of time for the ABTS:hydrogen peroxide concentrations and pH values of. A) 30 µM ABTS:5 µM hydrogen peroxide at pH 7.5. B) 30 µM ABTS:50 µM hydrogen peroxide at pH 7.5. C) 30 µM ABTS:5 µM hydrogen peroxide at pH 4.8. D) 30 µM ABTS:50 µM hydrogen peroxide at pH 4.8.

Figure 4.2: The reaction between ABTS and hydrogen peroxide. Measurements collected every 30 seconds at pH 0.5 for a wavelength range of 250 to 700 nm. A) The collection of multiple spectra of the reaction between 30 µM ABTS and 5 µM hydrogen peroxide. B) Multiple spectra collected for the full spectrum of the reaction between 30 µM ABTS and 50 µM hydrogen peroxide.

Figure 4.3: The spectrum of ABTS and $HABTS^{+}$. ABTS (–) at 30 µM was measured under physiologically relevant conditions, and $HABTS^{+}$ at 30 µM at pH 4.8 and temperature 37.5 °C. A wavelength range of 250 to 700 nm was used.

Figure 4.4: The oxidation of ABTS by nitric acid. A) The reaction of 40 µM ABTS with 0.9 M nitric acid monitored over a wavelength range of 300 to 750 nm as a function of time. B) The reaction of 20 µM ABTS with 1.8 M nitric acid over a range of wavelength as a function of time. For A and B, the increase and decrease of the absorbance signal observed is indicated by the arrows. C) The absorbance at 415 nm (–), 530 nm (···) and 730 nm (--) for reaction A represented as a function of time. D) The absorbance at 415 nm (–), 530 nm (···) and 730 nm (--) for reaction B represented as a function of time.

Figure 4.5: The reaction between ABTS and MnO_4^{-}. The spectrophotometric readings are taken at a pH of 0.5 and temperature of 37 °C for ABTS and permanganate at concentrations of 20 and 10 µM respectively. The first five minutes of the reaction are presented.

Figure 4.6: The reaction of MnO_4^{-} with ABTS at 37 °C followed spectrophotometrically for a wavelength range of 300 to 800 nm as a function of time. A) 20 µM ABTS was mixed with 10 µM MnO_4^{-} at pH 4.8. B) 20 µM ABTS was mixed with 20 µM MnO_4^{-} at pH 4.8. C) 20 µM ABTS was mixed with 10 µM MnO_4^{-} at pH 7.5. D) 20 µM ABTS was mixed with 20 µM MnO_4^{-} at pH 7.5

Figure 4.7: The degradation of ABTS over time. A) 30 µM ABTS is inspected spectrophotometrically at 37 °C and pH 4.8 over a period of time to determine the decay of the signal collected at 345 nm. B) 30 µM ABTS is employed in a physiologically relevant system to observe the decay of the chromogen over time at 345 nm.

Figure 4.8: The degradation of $ABTS^{\bullet+}$ over time. A) 20 µM ABTS is oxidised using MnO_4^{-1} to form $ABTS^{\bullet+}$, which is inspected spectrophotometrically at 37 °C and pH 4.8 as a function of time to determine the decay of the signal collected at 730 nm. B) 20 µM ABTS is oxidised using MnO_4^{-1} to form $ABTS^{\bullet+}$ in a physiologically relevant system to observe the decay of the signal over time at 730 nm.

Figure 5.8: Comparison of theoretical and experimental absorbance data for the peroxidase-like reaction of Fe(III)PPIX. The reaction is followed at a wavelength of 660 nm for reagent concentrations as stipulated in Table 5.1 according to the corresponding letter. The red line on main graphs represent experimental values, while the black line denotes model generated data. The model tested is model 5(ir)_ox_ab. Insets present the residual plots of every corresponding set of fitted data.

Figure 5.9: Comparison of theoretical and experimental absorbance data for the peroxidase-like reaction of Fe(III)PPIX. The reaction is followed at a wavelength of 660 nm for reagent concentrations as stipulated in Table 5.1 according to the corresponding letter. The red line on main graphs represent experimental values, while the black line denotes model generated data. The model tested is model 5(r)_ox_ab. Insets present the residual plots of every corresponding set of fitted data.

Figure 5.10: Comparison of theoretical and experimental absorbance data for the peroxidase-like reaction of Fe(III)PPIX. The reaction is followed at a wavelength of 660 nm for reagent concentrations as stipulated in Table 5.1 according to the corresponding letter. The red line on main graphs represent experimental values, while the black line denotes model generated data. The model tested is model 6(ir)_original. Insets present the residual plots of every corresponding set of fitted data.

Figure 5.11: Comparison of theoretical and experimental absorbance data for the peroxidase-like reaction of Fe(III)PPIX. The reaction is followed at a wavelength of 660 nm for reagent concentrations as stipulated in Table 5.1 according to the corresponding letter. The red line on main graphs represent experimental values, while the black line denotes model generated data. The model tested is model 6(r)_original. Insets present the residual plots of every corresponding set of fitted data.

List of Tables

List of Schemes

Scheme 2.5: The steps of the Nelder Mead algorithm in objective function minimization. 1) represents centroid determination. 2) depicts the reflection of the worst vertex. 3) denotes the extension of the reflected vertex. 4) represents the contraction of the reflected and worst vertex. 5) depicts the shrinking of all coordinate points towards the best vertex.

Scheme 2.6: An example of a script file of DynaFit. Explanations regarding certain components are given in the script following double dashes.

Scheme 2.7: Adjustments of DynaFit default settings, with explanations as before

Scheme 5.1: The proposed mechanism of the peroxidase-like activity of haem. The green cycle is the general mechanism as presented for haem containing peroxidases [9]. The blue cycle is the incorporated ABTS complexation cycle as proposed in literature [5, 6]. The mechanism presented offers the best explanation for the kinetic qualities of the peroxidase-like reaction of Fe(III)PPIX. H represents haem, HP represents peroxohaem, P represents hydrogen peroxide, $H^{\bullet+}$ represents $Fe^{\bullet+}$(IV)PPIX=O, A represents ABTS, H=O represents Fe(IV)PPIX=O, HA represents a Fe(III)PPIX.ABTS complex, I represents the active intermediate, $H^{\bullet+}A$ represents a $Fe^{\bullet+}$(IV)PPIX=O.ABTS complex, $A^{\bullet+}$ represents ABTS radical and D represents degraded products.

1. Introduction

1.1. Malaria overview

Malaria is a disease caused by the infection of a human host with protozoan *Plasmodium* parasites that enter an individual via a blood meal of the disease carrying female *Anopheles* mosquitoes [1]. The disease poses a threat as it eventually leads to patient death if left untreated for too long. Malaria is currently viewed as one of the more persistent and dangerous diseases in the world due to the continued rise of resistance shown in parasites to old and new antimalarial treatments[2]. This is cause for alarm as the formation of antimalarial resistance by malaria renders current drug treatments inefficient in eliminating the disease.

Plasmodium falciparum is historically known as the most devastating species regarding malaria related deaths, and is additionally called upon as the most aggressive species of *Plasmodium* [3]. As stated by Naing *et al.*, however, the danger of *Plasmodium vivax* may have been underestimated, as the 2017 World Health Organization's (WHO) malaria report shows a significant number of cases due to this species in all regions except Africa [2, 4]. While the greatest number of cases are reported for African regions (194 million), the South-East Asia and Eastern Mediterranean regions cannot be ignored, with 14.6 and 4.3 million cases, respectively [2]. As malaria clearly poses a dangerous risk for human wellbeing, efforts are continuously made to unveil plausible target areas of *Plasmodium* parasites in a struggle to present a method or treatment capable of battling and possibly eradicating this disease.

1.1.1. Malaria life-cycle

Malaria infection is started by injection of sporozoites into the skin of a human host by the *Anopheles* mosquito during a blood meal, after which the sporozoites attempt to invade the blood vessels [5]. Successful sporozoites are transported to the liver where they subsequently infect the hepatocytes, in which the malarial cells grow and undergo asexual reproduction [6, 7]. Infected hepatocytes burst and release merozoites, which are transported to blood vessels, where the protozoan cells consequently infect erythrocytes. Infection of erythrocytes signifies the start of the blood stage in the life cycle of the parasite [7]. The parasite can undergo asexual or sexual production within the erythrocyte to produce either merozoites or gametocytes [8]. Once proliferation is complete, the erythrocyte bursts, releasing newly produced merozoites to restart the cycle. Gametocytes produced are transported close to the skin to be ingested by *Anopheles* mosquitoes during blood meals [9]. The sexual reproductive cycle of the parasite is completed in the mosquito, and the process is restarted (Scheme 1.1). As the erythrocytic

cycle is the portion of the protozoan life cycle that is associated with the appearance of clinical symptoms of malaria, most studies focus on the different processes and components involved with the development of the parasite within an infected red blood cell. The symptoms include, but are not limited to, nausea and vomiting, fever, jaundice, as well as mild to severe cases of anaemia [10]. Anaemia in patients indicates an insufficient functioning erythrocyte count to meet the physiologic requirements of the human body [11]. The most common cause for anaemia is iron deficiency, which links to parasites feeding on haemoglobin, a protein which transports small molecules such as oxygen to areas of the body where it is required [12, 13].

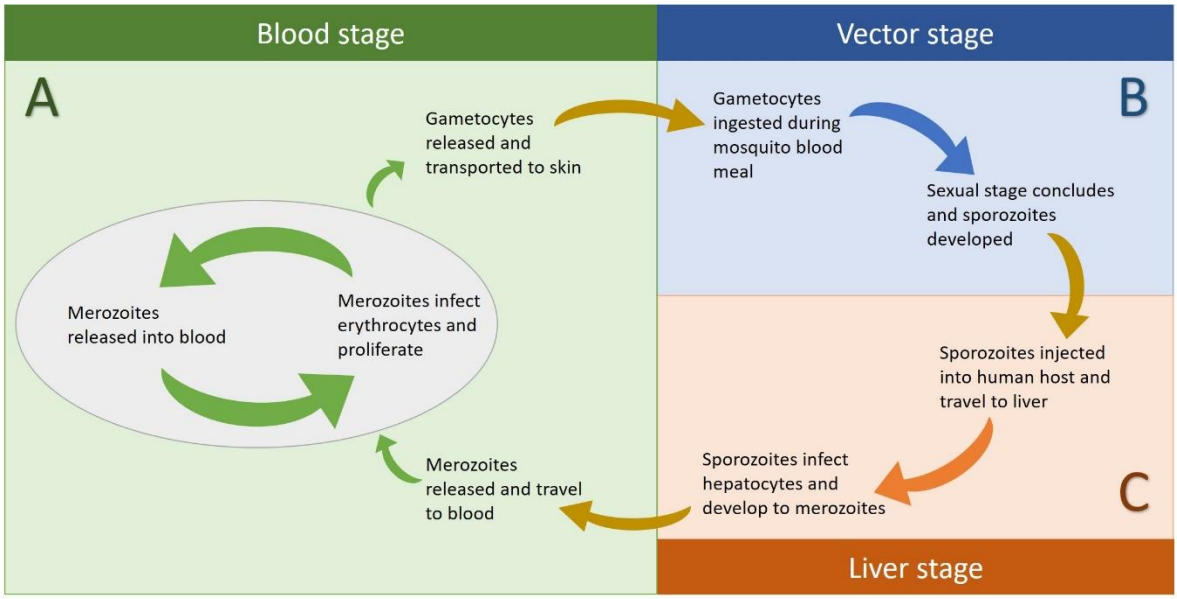

Scheme 1.1: A general scheme of the malaria parasite life cycle. A) represents the erythrocytic stage, B) denotes the reproductive stage within the Anopheles mosquito, and C) represents the hepatocytic stage. The cycle has been drawn based on the description of host-parasite interactions by Oaks et al. [14].

1.1.2. The erythrocytic stage

Within an infected erythrocyte, the merozoite undergoes various stages of reproduction to develop new merozoites or gametocytes. Energy is needed for these maturing and proliferation processes, and as such the parasites transport haemoglobin (Figure 1.1) from the erythrocyte it inhabits into the parasitic digestive vacuole for digestion. Haemoglobin therefore serves as a nutrient source for reproducing and maturing parasites.

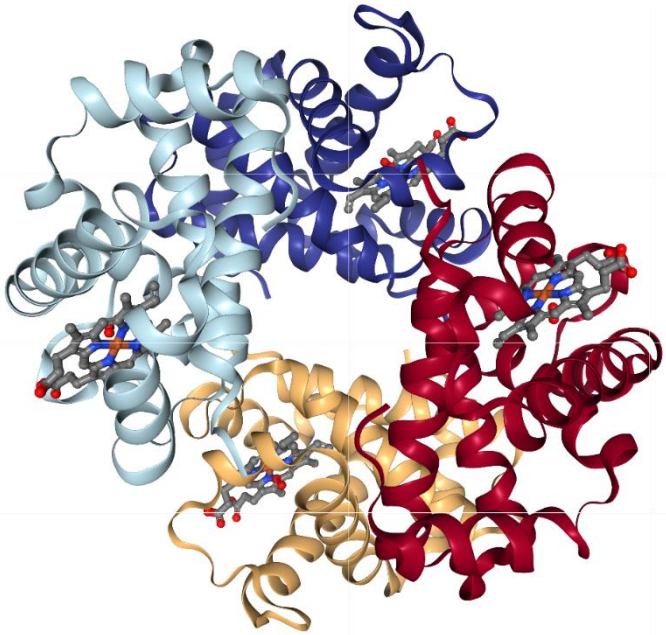

Figure 1.1: The protein structure of human haemoglobin proteins. The structure consists of four subunits, each with the ability to bind a prosthetic group. The protein shows haem bound to every subunit. The structure was obtained from PDB with ID: 1GZX [15].

Haemoglobin can bind up to four functional moieties commonly termed haem that cannot be degraded by the parasite and are thus released within the parasite at the location of haemoglobin digestion. Haem is an iron protoporphyrin IX compound, with the iron in the ferrous state [Fe(II)PPIX]. Fe(II)PPIX causes a multitude of problems in the parasitic cell if left unregulated as a build-up can effectively lead to parasite death. As haem is released following haemoglobin degradation into an oxygen rich environments, Fe(II)PPIX is rapidly oxidised to Fe(III)PPIX. To prevent the toxic effect of Fe(III)PPIX, the iron porphyrin is aggregated to form haemozoin crystals, generally also used as an indicator of infection in a patient [16]. As the parasite removes free Fe(II)PPIX from the cell, the toxicity of this compound is of interest as it offers a target for treatment and possible eradication of the disease.

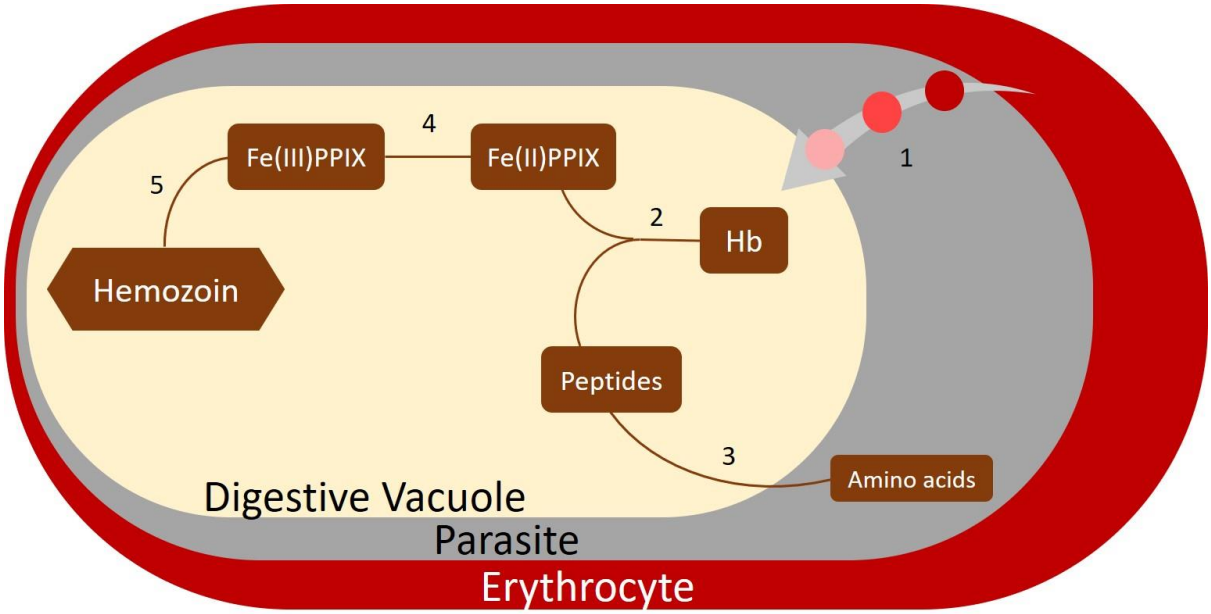

Scheme 1.2: A general depiction of the digestion of haemoglobin by intraerythrocytic malaria parasites. 1) Cytosomal vesicles transport haemoglobin from the infected erythrocytic cell to the digestive vacuole of the parasitic cell. 2) Haemoglobin is degraded, releasing peptides and haem. 3) The peptides are further degraded to form amino acids for use within the parasitic cell. 4) Haem is oxidised to form haematin, 5) which is aggregated to produce haemozoin crystals. The figure was drawn based on a description by Francis et al. [17].

1.2. Haem in the body

Fe(II)PPIX is an organometallic compound consisting of a ferrous iron ion coordinated to the centre of an organic porphyrin ring via nitrogen atoms [18]. The ring itself is constructed of four methane bridged pyrrole rings with substituents including methyl, vinyl, and propionic acid substituents (Figure 1.2). The iron coordinated in the centre of the porphyrin compound is stable either in the ferrous (II) or ferric (III) state [19]. The combination of the hydrophobic nature of the methyl and vinyl groups and hydrophilic nature of the propionate groups of the porphyrin ring allows for the amphiphilic nature of this organometallic compound [20].

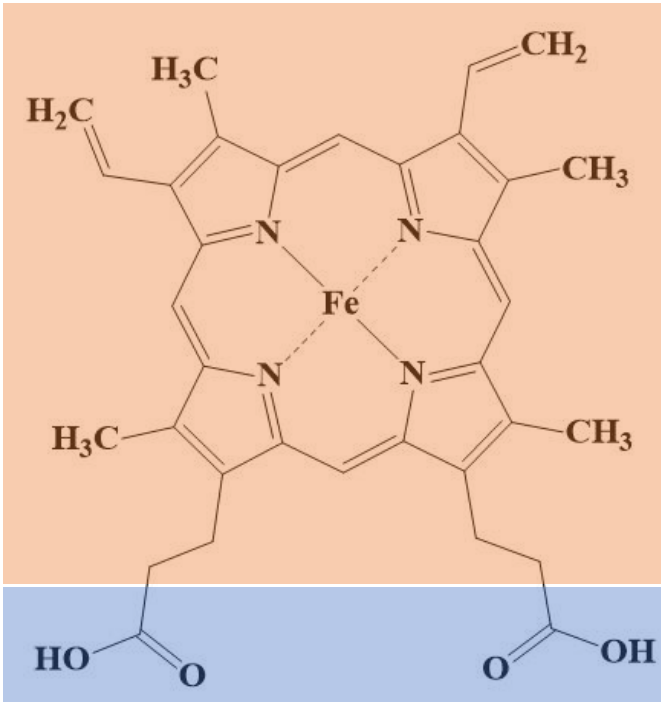

Figure 1.2: The structure of haem, with the hydrophobic and hydrophilic sections of the moiety indicated in red and blue respectively.

1.2.1. The biological role of Fe(II)PPIX

Fe(II)PPIX plays an important role in biological processes for its amphiphilic nature and ability to participate in redox reactions. For example, Fe(II)PPIX as enzyme cofactor forms a necessary component in transport and storage of small molecules, intracellular respiration for energy, neurotransmitter and lipid synthesis and degradation, as well as regulating oxidative damage in mammals [21–24]. The moiety can associate with proteins as the iron ion in haem can coordinate six ligands, with four axial ligands occupied by the porphyrin ring. This allows the moiety to associate with proteins to assist in certain essential biological functions, with the most well-known association being the functional role of Fe(II)PPIX as cofactor of haemoglobin. Fe(II)PPIX participates as a moiety in various proteins, and is essential for the function of certain enzyme systems like nitric oxide synthases and several catalases [19, 22]. Fe(II)PPIX also plays a functional role as moiety in the peroxidase activity of horseradish peroxidase (HRP) [26]. While the most stable states of the iron centre of the porphyrin are ferrous or ferric, it can also adopt a ferryl (IV) state during the catalysis of certain reactions [27]. The less stable ferryl oxidation state of the central iron allows for the porphyrin moiety to participate in electron transport reactions in the mitochondria, as well as in redox reactions [27]. Fe(II)PPIX furthermore regulates molecular and cellular processes such as transcription, by for example interacting with the transcriptional activator haem-activating protein 1 (HAP1) that binds to DNA with high affinity to

activate transcription [25, 28]. Another way in which haem regulates transcription is by up-regulation of nuclear factor-erythroid-2 (NF-E2) binding activity, where NF-E2 is a transcription factor specific to erythroids that partakes in the activation of globin and other erythroid specific genes [28]. Protein translocation is also influenced by haem, as the haemoprotein human eukaryotic translation initiation factor 2-alpha kinase 1 (HRI) can inhibit eukaryotic initiation factor-2 (elF-2) by phosphorylation of a serine in the α subunit of elF-2 [29]. The function of elF-2 is to initiate translation via interaction with the initiator transfer RNA. The inhibition is initiated either by heat shock, or due to a shortage of haem presence in the body. Haem also has a role in protein assembly, such as a deficiency of haem leading to the inhibition of complex IV assembly of the electron transport chain, to prevent the formation of free radicals that may damage the mitochondria of the cell in the absence of radical regulators [30]. Fe(III)PPIX additionally controls biological processes through the activity of haemoproteins such as neuferricin, an extracellular haemoprotein which promotes neurogenesis [31]. The moiety has moreover been proven to have a controlling role in the activities of signal transducers and transcriptional regulators [29–32]. Consequently, the need for Fe(II)PPIX in the mammalian body is clear. However, a problem that arises with the necessity of the iron porphyrin is that its dysregulation can cause numerous problems.

1.2.2. Dysregulation of Fe(II)PPIX

Dysregulation of Fe(II)PPIX levels causes severe complications that can subsequently lead to various diseases [32]. For the biosynthesis of Fe(II)PPIX, defective synthesis has been suggested to play a role in diseases such as anaemia and porphyrias, while deficiency of Fe(II)PPIX may factor into mitochondrial and neural decay which leads to Alzheimer's disease and aging [32–34, 35–37]. Excess free Fe(II)PPIX can readily be oxidised to Fe(III)PPIX, implicated in indirect mediation of severe cell and tissue damage via induction of oxidative stress through the production of reactive oxidative species (ROS) [38, 44, 45]. Reactions involving ROS can cause protein, lipid and DNA damage drastically impairing the cell [41–43]. Fe(III)PPIX can additionally congregate in cell membranes due to the hydrophobic nature of the porphyrin ring, where it promotes one-electron oxidation reactions, leading to membrane damage and haemolysis [50, 51]. Fe(III)PPIX is connotated to formation of small peptide fragments by degradation of proteins, and Fe(III)PPIX-mediated inflammation is implicated in pathogenesis of diseases such as renal failure, heart transplant failure and arteriosclerosis [28, 48, 49, 54, 55]. Elevated Fe(III)PPIX levels can thus act as a pro-inflammatory agent, plausibly via production of ROS [56, 57].

Most complications caused by the iron porphyrin are due to its capability to partake in redox reactions. The activity of Fe(III)PPIX is akin to a Fenton type reaction (Eq. 1.1) , generating hydroxyl radicals via

interaction involving hydrogen peroxide [52]. This reaction is also implicated in the hydroxyl radical producing capabilities of haemoglobin and cytochrome c, which are both haemoproteins [52].

$$H_2O_2 + Fe^{2+} \rightarrow HO^{\bullet} + HO^{-} + Fe^{3+} \qquad Eq.1.1$$

Consequently, this moiety can clearly be considered problematic if in excess, unregulated or simply absent. However, for mammals with dysregulation of Fe(II)PPIX, several detoxification pathways exist for the catabolism of the toxic porphyrin moiety.

1.2.3. Fe(II)PPIX detoxification in mammalian cells

To ensure that redox homeostasis is maintained within an organism, cells of the organism possess antioxidants and metal sequestering proteins to intercept or inhibit the formation of pro-oxidants by Fe(III)PPIX. As oxidative stress caused by the products of Fe(III)PPIX redox reactions can lead to extensive damage in the cell, mechanisms exist for the protection against and repair of such damage. Haem oxygenase (HO) has been identified in humans to regulate the unbound iron levels in the body [47, 48]. Of the three isoforms identified in mammals, it is HO-1 that controls the detoxification of Fe(II)PPIX [55]. The detoxification (Scheme 1.3) is initiated by selective cleavage of the α-methene bridge of the porphyrin ring and requires the presence of oxygen and NADPH (1) to form α-Hydroxyhemin [47, 48]. Thereafter, α-Hydroxyhemin reacts with oxygen to form biliverdin, releasing the central iron from the porphyrin structure in the process (2) [47, 48]. Biliverdin reductase can react with biliverdin in the presence of NADH to produce bilirubin (3). The released iron is incorporated into transport proteins ferritin or transferrin [56].

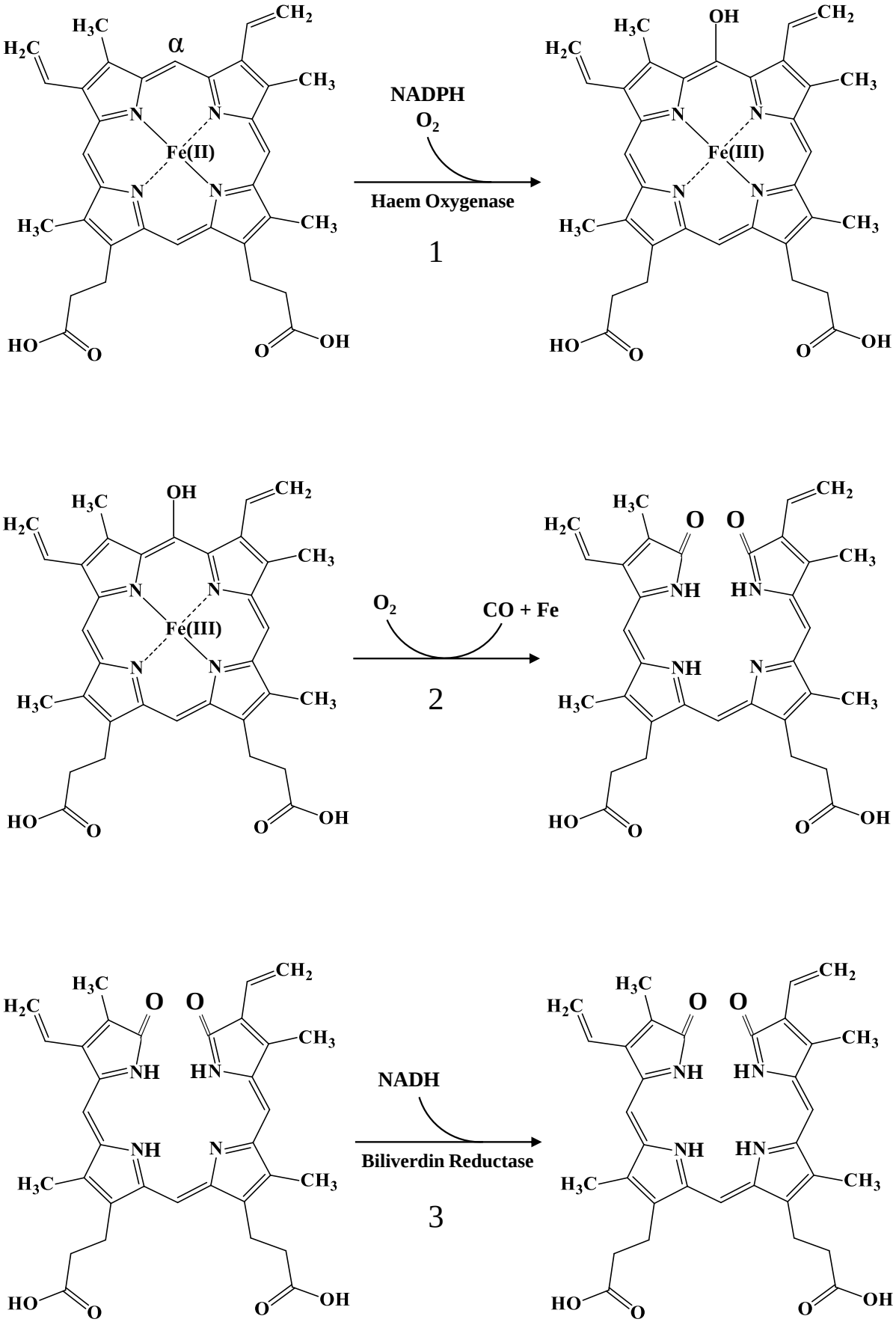

Scheme 1.3: The detoxification pathway for Fe(III)PPIX detoxification in vertebrates [27].

However, HO only offers protection in organisms that contain it. For organisms such as *Plasmodium* parasites, which do not express HO proteins, other mechanisms of Fe(II)PPIX detoxification are utilised. These mechanisms in such organism can include sequestration of Fe(III)PPIX into crystal form to inactivate the compound, or Fe(II)PPIX containment by haem binding proteins to inhibit the activity of the moiety. The sequestration of Fe(II)PPIX is the method employed by malarial parasites, by which the formation of the inert crystal haemozoin is observed. Multiple hypotheses have been proposed regarding the aggregation of toxic Fe(II)PPIX in *Plasmodium* parasites. The first is that the crystallization is mediated by an autocatalytic process, with haemozoin adsorbing to already existing haemozoin crystals [57]. The second theory suggests the involvement of enzymes in the aggregation. Histidine Rich Protein 1 (HRP1) is suggested as possible candidate, as it is ingested by the parasite during the process of haemoglobin degradation, and it has been demonstrated to induce haemozoin synthesis *in* vitro [58]. The parasitic cell also transcribes for at least two HRPs that seem redundant in function, which may be involved in the crystallization process [58]. However, as double mutants for HRPII and HRPIII still lead to haemozoin formation, it was reasoned that HRPs might not be involved in haemozoin formation [59, 60]. Originally haemozoin formation was thought to be regulated by a haem polymerase enzyme; however, a lack of evidence for the existence of this enzyme led to the suggestion that the process does not involve polymerization, that haemozoin is not a polymer, and that the process is better described as biocrystallization than as polymerization [61]. The third hypothesis is that haemozoin formation is catalysed by lipids [62–64]. Some lipids have been observed spectroscopically to promote the formation of β-haematin crystals, a synthetic form of haemozoin [65, 66]. Lipids associated with the digestive vacuole of the parasite have been characterized as a neutral lipid blend and monopalmitoylglycerol, synthesized by the parasite and packed in the digestive vacuole [65, 66]. It is thought to receive the nutrients for the formation of the lipids via transport vesicle digestion [65, 66]. These lipids are effective at converting haematin to β-haematin *in vitro* [67]. As haemozoin nucleation has been found to occur in an oriented manner with crystallization in aqueous phase at the inner surface of the digestive vacuole, the involvement of enzymes cannot be ruled out completely [68]. The last plausible mechanism by which the crystallization process may occur is by the activity of the Haem Detoxification Protein (HDP), which is believed to be excreted into the infected erythrocyte from the parasite prior to haemoglobin uptake by *Plasmodium* [69]. For HDP function, haemoglobin is transported from the red blood cell, thought to be accompanied by HDP, in cytosomal vesicles to the digestive vacuole of the parasite, subsequently ensuring the detoxification protein is located close to the site of Fe(II)PPIX release from digested haemoglobin [69]. However, most evidence point to an autocatalytic biocrystallization process that may be mediated by the lipid membrane of the digestive vacuole within the parasitic cell.

1.2.4. Measuring the toxicity of Fe(III)PPIX

Fe(III)PPIX displays both catalase and peroxidase-like ability due to its potential to participate in redox reactions. Studies by van Eldik and co-workers show that the catalase-like activity of hematin is only observed for pH levels above 9 [70]. Thus, the toxicity of Fe(III)PPIX can be extrapolated by observation of the peroxidase-like activity of the porphyrin. An area of dispute exists regarding the location within the parasitic cell in which haemoglobin digestion is initiated. It could either be commenced in cytosomal vesicles involved in haemoglobin transport from the erythrocyte to the parasite digestive vacuole, or within the digestive vacuole itself, thus offering a choice of pH values between 4.8 (in the digestive vacuole) or 7.5 (in the plasma) for the degradation to occur within [43, 44]. The importance of this discrepancy is that digestion of the carrier protein and subsequent release of Fe(II)PPIX signifies the start of the development of oxidative stress within the parasite, mediated by haem or hematin toxicity. The organelle in which haemoglobin is degraded may play a role in the activity of this moiety due to the difference in pH as an increase in pH from acidic levels to neutral has been shown to increase the reactivity of iron porphyrins [73]. The general mechanism of the peroxidase-like activity of Fe(III)PPIX is discussed briefly.

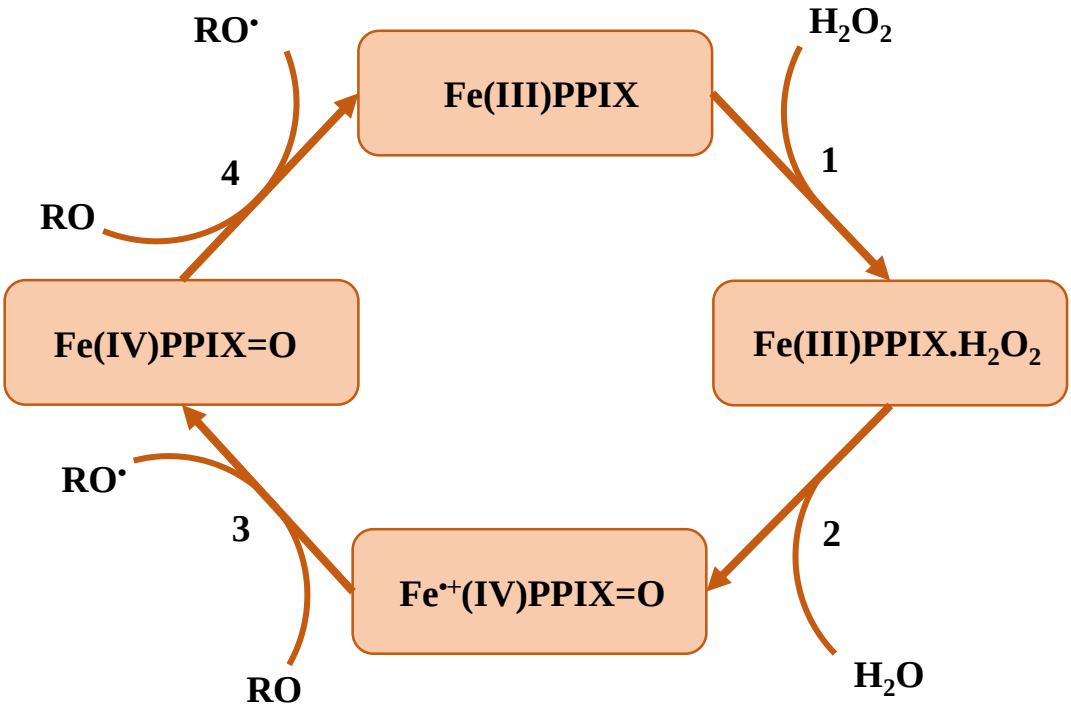

Figure 1.3: The general depiction of the peroxidase-like activity of Fe(III)PPIX.

The peroxidase-like cycle presented in Figure 1.3 is initiated by the association of hydrogen peroxide with Fe(III)PPIX (1), resulting in the formation of radical ferryl iron-oxo porphyrin [$Fe^{\bullet+}$(IV)PPIX=O] and water (2). $Fe^{\bullet+}$(IV)PPIX=O can react with electron donating species such as oxygen containing compounds within the cell to produce oxygen radicals (3), resulting in the generation of Fe(IV)PPIX=O. The latter species can undergo one more electron transfer reaction to generate a second radical (4), subsequently regenerating Fe(III)PPIX. Production of radicals causes a build-up of oxidative potential within the cell, which may ultimately lead to cell death if not modulated by detoxification systems within the cell. Therefore, unregulated Fe(III)PPIX present in a body may lead to the generation of radical compounds, as presented in Figure 1.3, via the peroxidase-like activity of the iron protoporphyrin IX. As discussed previously, the presence of dysregulated ferrous or ferric iron porphyrin in the human body causes various diseases related to its toxic capabilities. This toxicity can as such be elucidated by observing the peroxidase-like activity of Fe(III)PPIX species.

The redox activity of Fe(III)PPIX moiety has been studied spectrophotometrically for years as a potential model to represent the activity of peroxidase and catalase enzymes due to the similar mechanism it exhibits. However, discrepancies regarding the exact reaction steps of the peroxidase-like activity of haem have led to doubt regarding the most accurate representation of the reaction. Thorough analysis of this reaction will yield a reaction mechanism that best describes the kinetic activity of Fe(III)PPIX. A potential application of such a kinetic model would be to investigate the proposed modulatory effects of antimalarial drugs in either up-regulation or down-regulation of Fe(III)PPIX toxicity [74–76]. Subsequently, an important subject to consider in the observation of this reaction is to choose a chromogen that could function as both a radical scavenger and absorb at wavelength maxima differing from that of other absorbing species in the reaction, for ease of analysis.

1.3. Chromogen selection

A chromogen is a compound that absorbs light at a specific wavelength, used as a reference compound in reactions studied spectrophotometrically to follow the kinetics of the reaction studied. In cases where species in a reaction does not absorb light, or multiple overlapping absorbances exist, a chromogen can be used to visualize the progression of the reaction, either by simply absorbing light for the first case, or by absorbing at a unique wavelength not overlapping with any other species in the system for the latter case.

Choosing a chromogen is a vital part of creating a protocol for an experimental procedure. The chromogen is chosen based on the characteristics it presents. For example, using a chromogen that cannot be oxidized to a radical would not suffice in this case, as the peroxidase-like cycle of Fe(III)PPIX necessitates a chromogen capable of undergoing a one-electron oxidation. Thus, the chromogen used

must have radical scavenging abilities. Hydrogen peroxide does not absorb at wavelengths higher than 300, and as such the absorbance of Fe(III)PPIX must be considered when choosing a chromogen. The absorbance maximum for the monomeric species is at 385 nm; however, Fe(III)PPIX shows significant absorbance up to 650 nm (Figure 1.4) [77].

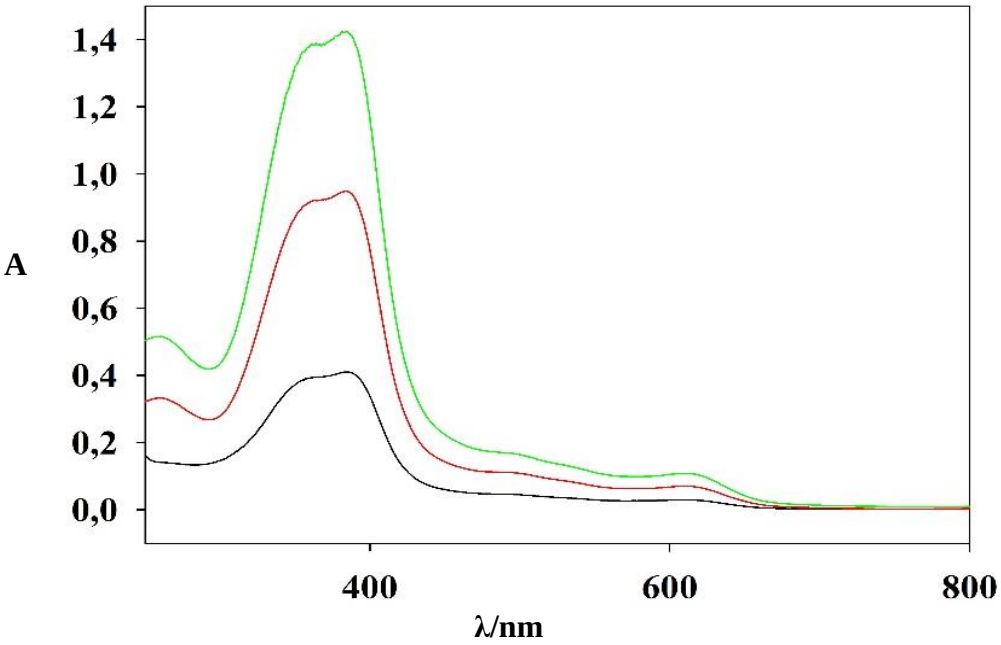

Figure 1.4: The absorbance spectra of Fe(III)PPIX. The spectra were recorded in Tris buffer at pH 7.5 and temperature 37 °C, using 10 (black), 20 (red), and 30 (green) µM of Fe(III)PPIX.

Therefore, the chromogen used must have absorbance maxima at longer wavelengths around the region of 700 nm. The last requirement is that the radical scavenging capabilities of the chromogen chosen must be to such an extent that the reaction proceeds relatively fast, as haem tends to adsorb to surfaces and degrade. Benzidine was used as chromogen in studying the peroxidase activity of HRP using hydrogen peroxide as oxidant, in the 1970s by Mesulam [78 & 79]. However, after it was discovered to be acutely toxic to humans by ingestion or inhalation, use of the compound has all but halted [80]. Porstmann *et al.* performed a comparative analysis of *o*-phenylenediamine (OPD), 2,2'-azino-di(3-ethylbenztiazoline sulphonic acid-6) (ABTS), *o*-dianisidine (ODS) and 4-aminoantipyrine as chromogens for the determination of HRP activity to ascertain the sensitivity of the chromogens [26]. They followed the reaction of HRP at 20 °C using the various chromogens for a pH range between 4 and 5. Their results show that OPD and ABTS demonstrated the highest sensitivity to the activity of HRP, followed by ODS. However, due to the light sensitivity of OPD, the use of ABTS and ODS were promoted, as the oxidised form of these two chromogens was stated to remain stable for up to a day at

room temperature, with ODS absorbing 3 percent less and ABTS 5.6 percent less after 2 days. They concluded that although ODS remains stable for longer, ABTS would serve as the best chromogen as its high sensitivity saves materials in the preparation of the experiment, as well as the fact that ODS absorbance is followed for wavelengths of 405 and 530 nm, both of which overlap with Fe(III)PPIX absorbance. As OPD shows high susceptibility to light, this chromogen is not considered for use in this study. ABTS as a neutral compound has an absorbance maximum at 345 nm and can be oxidised firstly to form $ABTS^{\bullet+}$, and secondly to produce $ABTS^{2+}$ [81]. $ABTS^{\bullet+}$ has absorbance maxima at 390, 415, 660 and 730 nm, while $ABTS^{2+}$ has an absorbance maximum in the range of 450 to 550 nm depending on the solvents used [81]. Thus, $ABTS^{\bullet+}$ is a viable option for monitoring the catalytic activity of haem, as the increase in absorbance for the radical species at longer wavelengths can be used as a measure of the peroxidase-like activity of the moiety. Oxidation of ODS generates a radical compound with an absorbance maximum at 405 nm [82]. Therefore, the absorbance of this chromogen would overlap with that of haem, thus complicating data analysis. Shalaby and Shanab used ABTS and 2,2-diphenyl-1-picrylhydrazyl (DPPH) assays to determine the antioxidant potential of plant extracts [83]. In this study, ABTS and DPPH radicals were generated using strong oxidising agents, such as potassium permanganate. They state that ABTS is generally considered a good chromogen as the absorbance maxima of the radical at longer wavelengths does not lead to absorbance interference with other light absorbing species in the reaction. The flexibility of the acidic to neutral pH range under which ABTS could be used further substantiates the selection of this chromogen, while DPPH is sensitive to changes in pH [84]. Porstmann *et al.* found that ABTS reacted rapidly with HRP, reaching a steady state within half an hour, whereas DPPH took up to 8 hours to approach the steady state [26]. DPPH absorbs maximally at 515 nm [85], a wavelength at which Fe(III)PPIX also shows absorption, subsequently complicating analysis should this chromogen be used. Furthermore, taking the time consumption of the reaction using DPPH into account, this chromogen will not be suited to the experimental protocol required. Drozd *et al.* revisited the use of catechol derivatives as chromogens in studying nanozyme catalytic activity [86]. Nanozymes refer to nanoparticles exhibiting enzymatic action. In their findings, they state that the derivatives pyrogallol (PG) and bromopyrogallol red (BPR) can be oxidised by hydrogen peroxide, while popular chromogens such as ABTS or 3,3',5,5'-tetramethylbenzidine (TMB) cannot. While this assisted in their particular research, the oxidation of the chromogen by hydrogen peroxide is an unwanted reaction in the study of the peroxidase-like activity of haem, eliminating the chromogens PG and BPR from this study. The chemical structures of all chromogens discussed are presented in Scheme 1.4.

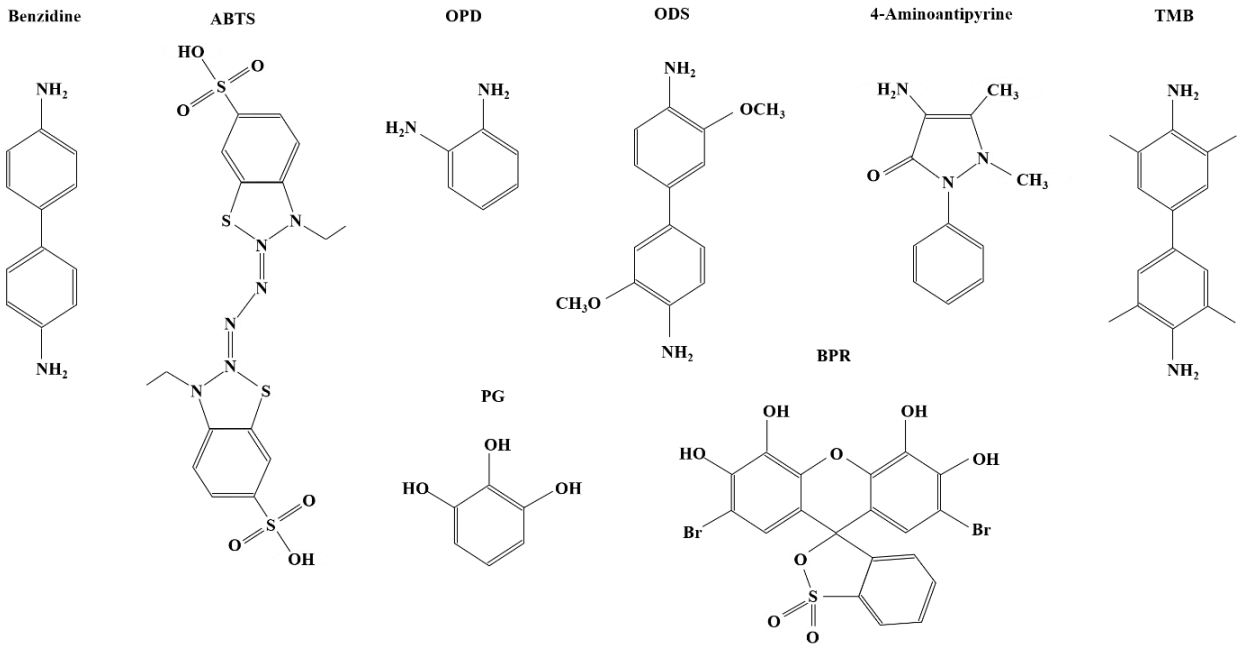

Scheme 1.4: The structures of chromogens discussed as potential candidates for following the peroxidase-like activity of Fe(III)PPIX. All structures were redrawn using data obtained from PubChem [87].

The radical species of ABTS has been studied in terms of its effectiveness as reference chromogen for use in kinetic studies by Wolfenden and Willson [88]. They used electrophilic free radicals to illustrate the radical scavenging rate and ability of ABTS in one-electron oxidation reactions. The results emanating from this study indicate this chromogen as a useful free radical for reference in spectrophotometric observations of oxidation reactions. Miller *et al.* presented a method for measuring antioxidant capacity using ABTS as chromogen in studying this capacity in premature infants [89]. According to a study by Turnbow and Garner on the stability of ABTS as chromogen in studying peroxidase-based enzyme-linked immunosorbent assay (ELISA) systems, ABTS stability is reduced at a higher pH [90]. For a pH approaching physiologically relevant conditions, decay of the absorbance maxima of $ABTS^{\bullet+}$ could be observed in multiple buffers at pH 7.5. The use of Tris and phosphate buffers stabilized the half-life of the chromogen radical to, respectively, 33 and 79 minutes at pH 7.5 and is thus propagated as necessary for using ABTS under physiologically relevant conditions. In studying a method for estimating antioxidant activity, Cano *et al.* measured the stability of $ABTS^{\bullet+}$ spectrophotometrically, monitoring the decrease in radical absorbance [91]. They determined $ABTS^{\bullet+}$ to become unstable as the temperature increases and pH level rises to strive to physiologically relevant conditions, indicating that even when using Tris or phosphate buffer, the degradation of ABTS and $ABTS^{\bullet+}$ need to be considered when analysing kinetic data representing the toxicity of haem. Cano *et al.* also studied the stability of $ABTS^{\bullet+}$ as a function of ABTS concentration present in the solution and found it to be greatly improved by a concentration ratio of, at the least, twenty to one of ABTS to

$ABTS^{\bullet+}$. This suggests using an excess of chromogen in the reaction mixture to ensure the ratio of unreacted ABTS to $ABTS^{\bullet+}$ remains high enough to have a stabilizing effect on the radical chromogen species.

1.3.1. Reactions of ABTS

Based on the literature review discussed above, ABTS is chosen as the chromogen for this study. ABTS is a water-soluble compound commonly used to measure antioxidant activity due to the two one-electron reductions it can undergo, and the characteristic wavelengths for the radical ($ABTS^{\bullet+}$) and dication ($ABTS^{2+}$) species of ABTS formed by the reduction reactions involving an electron exchange (Figure 1.5).

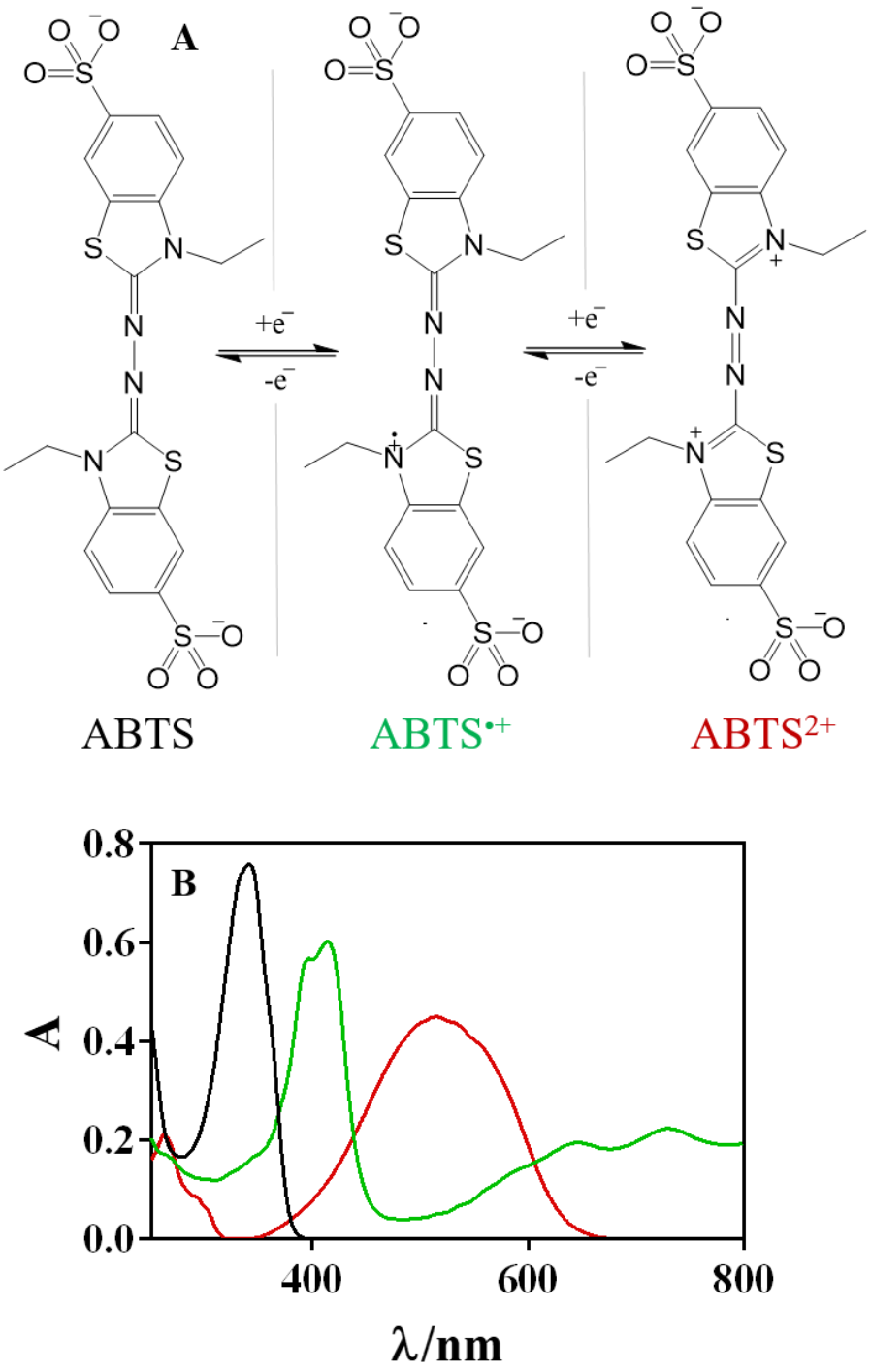

Figure 1.5: The different species of ABTS (A), along with the respective spectrum of each species (B). For B, ABTS is represented by a black line, $ABTS^{\bullet+}$ by a green line, and $ABTS^{2+}$ by a red line.

ABTS has a characteristic peak in the wavelength range of 300 to 350 nm, while $ABTS^{\bullet+}$ has a wide absorbance range with two maxima between 360 and 450 nm, as well as two maxima between 600 and 800 nm (Figure 1.5B). The absorbance range of $ABTS^{2+}$ falls between 375 and 650 nm (Figure 1.5B), which overlaps to a certain extent with both ranges of $ABTS^{\bullet+}$, as well as the absorbance of Fe(III)PPIX. $ABTS^{\bullet+}$ is usually measured at 660 nm, as this characteristic peak falls on a maxima of the radical absorbance spectra where few other compounds of the peroxidase reaction absorb [47, 64–66]. It would be

just as effective to measure $ABTS^{\bullet+}$ absorbance at the maximum around 730 nm, to ensure minimal overlapping of $ABTS^{2+}$ or Fe(III)PPIX absorbance with $ABTS^{\bullet+}$ will not occur.

The variety of wavelength maxima for $ABTS^{\bullet+}$ and $ABTS^{2+}$ shown in Figure 1.5B allows for effective determination of oxidation kinetics of compounds and enzymes tested in anti-oxidant assays. $Fe^{\bullet+}$(IV)PPIX=O, generated in the first step of the general mechanism of the Fe(III)PPIX peroxidase-like reaction, can oxidize two units of ABTS to $ABTS^{\bullet+}$ in a two-step process to regenerate the original Fe(III)PPIX compound in the cyclic process (Scheme 1.5). The generation of $ABTS^{\bullet+}$ can be measured spectrophotometrically without overlap of other absorbing species, thus easing the analysis of kinetic data collected.

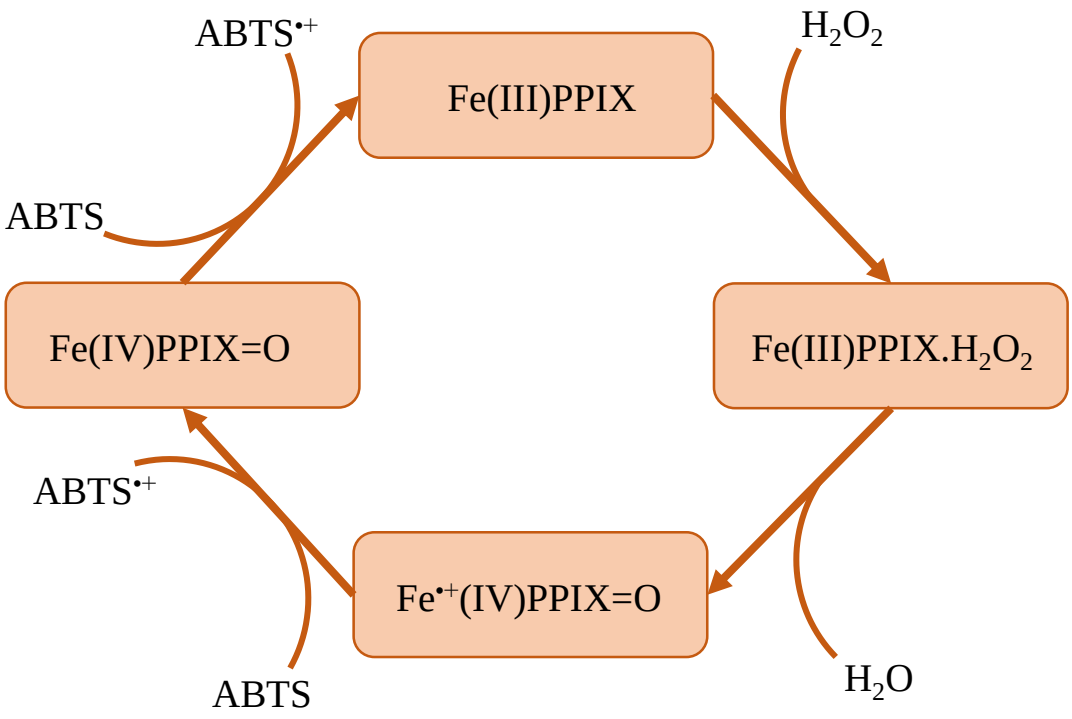

Scheme 1.5: The general mechanism of Fe(III)PPIX peroxidase-like activity incorporating the oxidation of ABTS

A disproportionation or comproportionation reaction (eq. 1.2 and 1.3, respectively) of $ABTS^{\bullet+}$ has been shown to be feasible in certain solution systems, which could affect the analysis of kinetic data collected [81, 94].

$$2ABTS^{\cdot+} \rightleftharpoons ABTS + ABTS^{2+} \qquad Eq.1.2$$

$$ABTS + ABTS^{2+} \rightleftharpoons 2ABTS^{\cdot+} \qquad Eq.1.3$$

For example, if ABTS is oxidised by $Fe^{\bullet+}$(IV)PPIX=O to form $ABTS^{\bullet+}$ the disproportionation reaction might commence. Two molecules of $ABTS^{\bullet+}$ react to form one molecule each of ABTS and $ABTS^{2+}$, which would affect the $ABTS^{\bullet+}$ absorbance signal observed and thus consequent analysis of kinetic data.

In studies conducted by Branchi *et al.*, the formation of $ABTS^{2+}$ at pH of 5 was observed after the addition of cerium disulphate to ABTS in a 1:2 ratio, respectively [81]. This experiment was conducted in a mixture of H_2SO_4 and acetonitrile at room temperature. They determined the dication species to have a half-life of ninety seconds under these conditions, and reasoned, with the addition of studies performed by Janata & Williams, that $ABTS^{2+}$ degrades via a hydrolysis pathway [95]. The rate of hydrolysis is shown to be dependent on the acidity of the medium used, with higher acidity having a stabilizing effect on $ABTS^{2+}$ [95]. As such, the opposite should hold true, suggesting that the rate of hydrolysis will increase with an increase in the pH level. Indeed, no $ABTS^{2+}$ is observed for the study conducted by Branchi *et al.* above a pH of 5 [81]. This would suggest that $ABTS^{2+}$ will be absent from the reaction under physiologically relevant conditions.

1.4. Antimalarial compounds

Currently, no effective vaccine against the malarial parasite exists, thus necessitating the appropriate use of antimalarial drug treatment. Certain antimalarials, such as quinoline derivatives, are thought to influence the toxicity of free haem [75]. The drugs primarily inhibit the aggregation of Fe(III)PPIX to haemozoin, however it may also modulate Fe(III)PPIX toxicity. Quinolines have been used to treat malaria infected patients for hundreds of years; however, the mechanism by which quinoline derivatives elicit their antimalarial effect is not elucidated fully [96]. Quinoline derivatives such as chloroquine, mefloquine, quinine and quinidine are thought to function by disrupting the sequestration of released Fe(II)PPIX following haemoglobin degradation in the parasitic food vacuole. Firstly, the derivatives were found to inhibit the aggregation of Fe(III)PPIX *in vitro* under physiologically relevant conditions [97 & 98]. Secondly, any inhibition mediated by these antimalarial compounds is only observed for malarial parasites in the feeding stage of the erythrocytic cycle, thus when the parasite is engaged in degrading haemoglobin and aggregating Fe(III)PPIX [96]. Furthermore, the first morphological changes observed in the intraerythrocytic parasite after administering quinoline antimalarial drugs is the swelling of the parasitic food vacuole and the formation of autophagic digestive vacuoles [99 & 100]. Following this, chloroquine and congeners are at nanomolar concentrations in the blood plasma, but hyperconcentrate to millimolar concentrations in the digestive vacuole of *P. falciparum* [101 & 102]. Lastly, the admission of quinoline antimalarials inhibited β-haematin formation for conditions relating to the aqueous phase of the parasitic digestive vacuole and is suggested to mediate this activity via the formation of a drug-haematin complex [103].

To support drug-Fe(III)PPIX interaction, the non-covalent ring stacking of the chloroquine nucleus and haem has been shown using NMR [104]. Chloroquine-Fe(III)PPIX complexes have even been detected *in situ*, although the complex could not be isolated from the parasite [105]. It has also been shown that the association between the quinoline derivative and Fe(III)PPIX can form either with the monomeric or dimeric form of haematin, with chloroquine driving the dimerization equilibrium in favour of dimeric haematin [106–108]. Chloroquine is believed to associate with the porphyrin μ-oxo dimer via a π-π complex, and amodiaquines are shown to associate with Fe(III)PPIX dimers in the same manner as chloroquine [109, 110]. Chloroquine was proposed to also bind to the fastest growing face of the haemozoin crystal forming in the parasite cell to decrease the rate of crystallization, based on crystallization of Fe(III)PPIX in dimethyl sulfoxide (DMSO) solvate [111]. The chloroquine-haematin complex has been demonstrated to enhance association between Fe(III)PPIX and membranes in malaria infected red blood cells, as well as to inhibit the degradation of haematin [74, 76]. However, the formation of the chloroquine-Fe(III)PPIX adduct leads to a decrease in peroxidase-like activity of haematin [74]. Data collected by Sullivan *et al.* on the association of chloroquine and quinidine with haemozoin suggests that these quinoline derivatives first bind to Fe(III)PPIX, after which the complex attaches to haemozoin elongation sites to prevent further crystallization, resulting in a build-up of toxic Fe(III)PPIX [112]. Quinine-Fe(III)PPIX adducts are believed to form via alkoxide coordination, with quinine shifting the dimerization equilibrium in favour of monomeric haematin [106, 108]. By systematic elimination of quinine functional groups, it was determined that the quinuclidine ring system with the tertiary nitrogen as well as the hydroxyl group is essential for the formation of drug-haematin adducts, as well as for antiplasmodial activity and haemozoin formation inhibition [109]. As such, these drugs, amongst others, seems to function by modulating the toxicity of free Fe(III)PPIX present in the cell by inducing haematin crystal formation. Studies on the modulation of Fe(III)PPIX peroxidase-like activity by chloroquine showed that the activity is decreased in the presence of the quinoline derivative; however, the degradation of Fe(III)PPIX is lowered [74]. An inhibitory effect on haemozoin formation is also observed by chloroquine binding to haematin with a higher affinity than HRP1 [113]. Consequently, quinoline antimalarials are believed to function by slowing or inhibiting haemozoin formation, as well as to bind Fe(III)PPIX to prevent detoxification, coupled with a decrease in the rate of peroxidase-like activity of haematin.

Rise of parasitic resistance to quinoline derivatives led to the development of artemisinin and derivatives to battle the disease. Derivatives include but are not limited to artesunate, artemether, arteether and dihydroartemisinin [114]. The speed at which these derivatives eliminates parasitic cells, coupled with the rapid disappearance of the antimalarial from the host, is believed to slow the formation of resistance in *Plasmodium* species. Artemisinin derivatives differ in structure to that of other antimalarial treatments, as it contains an endoperoxide bridge deemed necessary for its antimalarial activity [115]. As peroxides can function as a source of ROS, it was believed, and proven by electron paramagnetic resonance, that artemisinin generates free radicals as part of the mode of action [113, 114]. It

was demonstrated that artemisinin treatment to lipid membranes resulted in lipid peroxidation, for which the rate of the peroxidation was increased with the addition of Fe(III)PPIX [118–120]. The involvement of haematin was substantiated by the appearance of Fe(IV)PPIX=O for testing the interactions between artemisinin and Fe(III)PPIX [121]. No antimalarial activity of artemisinin derivatives was observed against *Babesia microti*, an intraerythrocytic apicomplexan parasite that lacks haemozoin, further substantiating the involvement of haematin in the mode of action [122]. The derivatives are thus suggested to be specifically toxic to parasitic cells due to the concentrated presence of Fe(III)PPIX released form degraded haemoglobin within parasitic cells. Regarding the interaction of artemisinin derivatives and haematin, artemisinin-haematin adducts have been observed in parasite cultures [123]. Adduct formation was shown to occur via covalent bonding of artemisinin to haematin, from which the artemisinin compound could react with haematin to form a carbon-based artemisinin radical and Fe(IV)PPIX=O [123, 124]. Formation of an artemisinin-haematin adduct have been proven to have an inhibitory effect on the biocrystallization of haematin, thus allowing for the accumulation of free haem that can activate more artemisinin in the parasitic cell [125]. Artemisinin has also been shown to form covalent bonds with, and modify, proteins of the parasitic cell that partake in metabolic pathways, to result in malfunction of enzyme activities [126]. Consequently, the activity of artemisinin is believed a function of the peroxidase-like activity of haematin, leading to rapid death of the parasitic cell via three proposed methods. One is through the inhibition of haemozoin formation, another by modification of parasitic protein structures to, for example, halt metabolic functions within the parasitic cell, and the last is enhancing lipid peroxidation due to the formation of radicals mediated by peroxidase-like activity of Fe(III)PPIX.

Antimalarial compounds of this type and strength thus offer an efficient method of eliminating malaria infection. However, over time these drugs have been losing their effectiveness, as recombination of the genetic makeup of parasitic DNA led to a build-up of resistance against the mode of action elicited by the antimalarial compounds [75]. Resistance against quinine appeared slowly and resistant strains seem to only diminish the capabilities of this antimalarial compound, rather than inhibit it [127]. Chloroquine resistance in *P. falciparum* has risen over the last hundred years to the point where vast areas report patients infected with resistant strains of the parasite [3]. The resistance in chloroquine is believed to be due to mutations in the parasitic genes *pfmdr1* (*Plasmodium falciparum* multidrug resistance gene 1) and *pfcrt* (*Plasmodium falciparum* chloroquine resistance transporter gene), of which the latter expresses a protein modulating drug concentration within the parasite, thus promoting the efflux of chloroquine from the parasitic cells [128, 129]. Upregulation of the gene *pfmdr1* is also believed to inhibit the mode of action of mefloquine [130].

Even if the activity of these treatments loses effectiveness, the compounds remain important to malarial research, due to the information it can yield regarding the mechanism by which it conducts its activity. Elucidating the mechanism would assist in the development of analogues and novel antimalarial

compounds to serve as a new line of defence for eliminating malaria in the case that the pathogen develops resistance against current frontline drugs and combination therapies. Most antimalarial compounds affecting Fe(III)PPIX during the degradation of haemoglobin focus on modulating the toxicity of the iron porphyrin either directly or indirectly. Subsequently, determining the exact effect these compounds elicit on the toxicity of Fe(III)PPIX would assist in the production of antimalarial analogues. However, to do so requires knowledge of the kinetic mechanism by which this toxicity is brought about.

1.5. Aims and objectives

Following analysis of literature on the toxicity of Fe(III)PPIX, malaria and antimalarial resistance in malaria, the purpose of this study was to present a model that best depicts the toxicity of Fe(III)PPIX. To complete this purpose, the objectives of the study included:

a) Analysis of the interaction between Fe(III)PPIX and hydrogen peroxide to generate a mechanistic model best depicting this portion of the peroxidase-like activity.
b) Model regression analysis for reaction steps proposed for the interaction between Fe(III)PPIX and hydrogen peroxide to retrieve the model best denoting this reaction.
c) Analysis of ABTS side reactions that may influence the kinetic observation of the peroxidase-like reaction.
d) Analysis of the Fe(III)PPIX peroxidase-like activity data collected by Miss C. Sammy during the course of her MSc [92].
e) Model regression analysis for reaction steps proposed for the peroxidase-like activity of Fe(III)PPIX to propose a model best depicting the underlying mechanism.

The underlying purpose of this study is to alleviate the current confusion regarding which peroxidase model would best represent the toxicity of Fe(III)PPIX, as the model generated could then be used in subsequent studies to investigate the effect elicited by antimalarial compounds on the toxicity of Fe(III)PPIX.

2. Chemical Kinetic Analysis

2.1. Introduction

Kinetic analysis of reactions can be carried out via two different methods, one involving model-free, and the other utilising model-based analysis. Model free analysis is useful for the determination of specific response curves for species involved in a reaction, such as the determination of molar extinction coefficients in UV-Vis spectroscopy [131, 132, 133]. Model-based analysis is employed to quantify parameters of the process observed, such as rate constants or equilibrium constants [132, 134]. These constants are crucial for the prediction of the chemical behaviour of species under unexplored conditions, as well as to elucidate reaction mechanisms such as the peroxidase-like cycle of haem in this study [132]. In the context of this chapter, the term kinetic study is regarded as a model-based investigation of chemical reactions to determine the most plausible reaction mechanism and quantify the associated parameters, such as rate constants, of proposed elementary reaction steps and extinction coefficients of species involved.

The use of multiwavelength UV-Vis data in experimental kinetic analysis is gaining popularity in terms of analysis robustness and relatively accurate determination of pure spectra of all reacting species and intermediates as the reaction progresses [135]. Another method alongside multiwavelength studies is the use of multivariate data, where multiple sets of kinetic data adhering to different initial conditions are simultaneously fitted in a single analysis [132, 135]. Initial conditions such as starting reagent concentration can thus differ between data sets collected experimentally to ensure the dependency of parameter estimates on the initial conditions is reduced. Results obtained by this type of analysis are termed "global" optimization of parameters, a term coined in the 1980's by Knutson *et al.* [136]. In this study, the collection of multiwavelength data is difficult as the reactions of interest are relatively rapid and only multivariate data analysis is employed. The difference between using multivariate or univariate data can be indicated by explaining the difference between global and local optimization. The optimization process involves the estimation of parameters of a proposed chemical reaction or set of reaction mechanisms that would best describe the measurement data under scrutiny. For model-based analysis, the objective is to find the global minimum, as the parameters obtained are applicable to predictions under unexplored conditions, while a local minimum will only be useful for a specific set of experimental conditions [132, 135, 137]. Utilizing multivariate data also assists with the reduction of model ambiguity [135, 137].

Multiple programs exist for model-based kinetic analysis of data, such as DynaFit or MatLab [138, 139]. DynaFit is a program used to perform non-linear least-squares (NLLS) fitting of data from spectrophotometric absorbance signals or the chemical shifts observed in nuclear magnetic resonance

spectra, using built-in functions to estimate parameters for proposed reaction steps. DynaFit can, however, only use data where the signal response is linearly dependent on species concentration. MatLab is a more complex analytical tool for researchers who want to use self-coded algorithms or alterations of algorithms for a model-based NLLS analysis. Programs such as DynaFit are utilised for their ease of use, as the program incorporates algorithms to allow the researcher to simply input elementary reaction steps and declare initial parameter values prior to NLLS analysis. MatLab offers more freedom, as self-coded algorithms can be used in combination with built-in functions to generate a program capable of NLLS fitting of data according to a proposed chemical mechanism, at the cost of convenience.

Both programs are utilised for the analysis of multivariate kinetic data sets in this study. DynaFit allows for the relatively fast analysis of the data provided. The in-house written program using MatLab termed $RunFit$ offers in-depth knowledge into the NLLS regression methods employed in this study and can easily be extended to systems where the signal response is non-linear with regards to species concentration, such as potentiometric measurements. A single variate version of the program is presented in the addendum. The program $RunFit$ will be used to explain the method of analysis employed in this study.

2.2. Data collection and preparation

Spectrophotometric measurements of selected wavelengths were collected as a function of time as the reaction proceeds. Thus, NLLS fitting is required pertaining to the minimization of the difference between experimentally recorded absorbance values and theoretically calculated values as a function of time. First, consider Beer's Law (Eq. 2.1).

$$A(t,\lambda) = \sum_{i=1}^{nc} c_i(t)\varepsilon_i(\lambda)l \qquad Eq.2.1$$

In the above equation, nc refers to the number of components or species partaking in the reaction mechanism, $c_i(t)$ represents concentration at a specified time, $\varepsilon_i(\lambda)$ denotes the molar extinction coefficients of each species in the reaction mixture and l refers to the cuvette path length. Beer's Law states that the absorbance of a sample at a specific time is equal to the sum of the products of the concentration and extinction coefficients of each species in the reaction. For clarity purposes, this law can be presented in the format of matrices (Scheme 2.1).

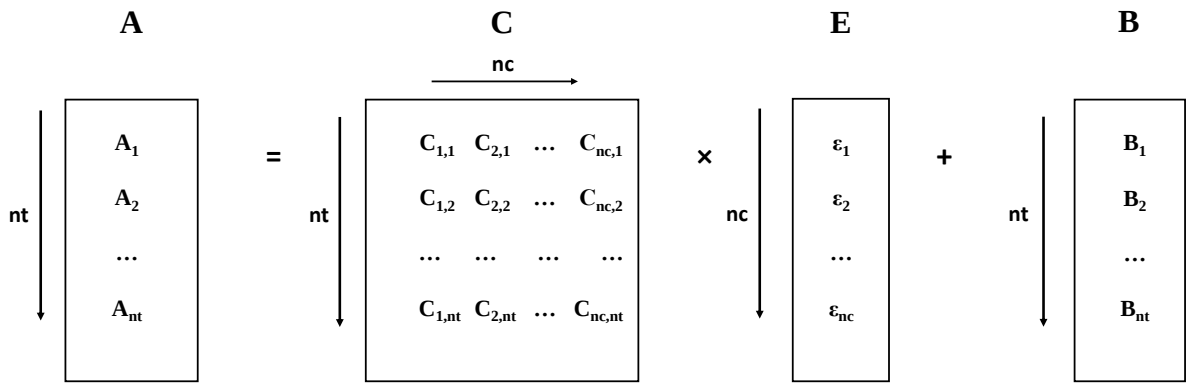

Scheme 2.1: A visual representation of calculating the absorbance matrix in a system of multiple reactive species. Matrix A represents absorbance values for spectrophotometric readings at each of the nt time points. Matrix C represents the concentration profiles for each reacting and forming species in columns, with each row of the matrix corresponding to a time-point of signal recording in matrix A. Matrix E contains the response coefficients for all species present in the reaction mixture. Matrix B contains all measurement signal errors for each of the readings taken during spectrophotometric time assays.

In Scheme 2.1, matrix A represents the time dependent experimental absorbance data recorded spectrophotometrically. Matrix C columns represents the time dependent concentration profile of each participating species in the sample. Matrix E contains molar extinction coefficients for all species present in the reaction mixture. The last matrix B represents the signal error of spectrophotometric

recordings for each reading in matrix A. nt denotes the number of time points of readings taken in data collection. The method of matrix A calculation is discussed in the following section.

2.3. NLLS regression

To perform the NLLS calculation, an objective function must first be constructed, which is then minimized by numerical methods, varying in this case rate constants and extinction coefficients. The elementwise difference between the two absorbance matrices squared is the sum of squared errors (SSQ) (Eq. 2.2),

$$SSQ = \sum_{i=1}^{nt} (A_{data,i} - A_{model,i})^2 \qquad Eq\ 2.2$$

where A_{data} and A_{model} represents the experimental and model generated absorbance matrices and nt refers to the number of readings taken in a time assay. The calculation returns a numerical value partially describing the goodness of the fit achieved between the proposed chemical model and the experimental data. For multivariate data sets, multiple absorbance matrices need to be incorporated in the NLLS analysis, necessitating the grouping of these absorbance matrices to form a single matrix for NLLS to fulfil the requirements for global optimization (Scheme 2.2). Reaction models proposed contain estimated parameters that are used to calculate theoretical absorbance values based on the initial conditions of each data set. Thus, the absorbance matrices are generated for each set of kinetic data on its own, before collocating all the matrices into one for comparison to the also collocated experimental

absorbance matrix A_T. As such, the simultaneous analysis of multivariate kinetic data sets, compared to univariate approaches, offers more comprehensive approximation of parameters.

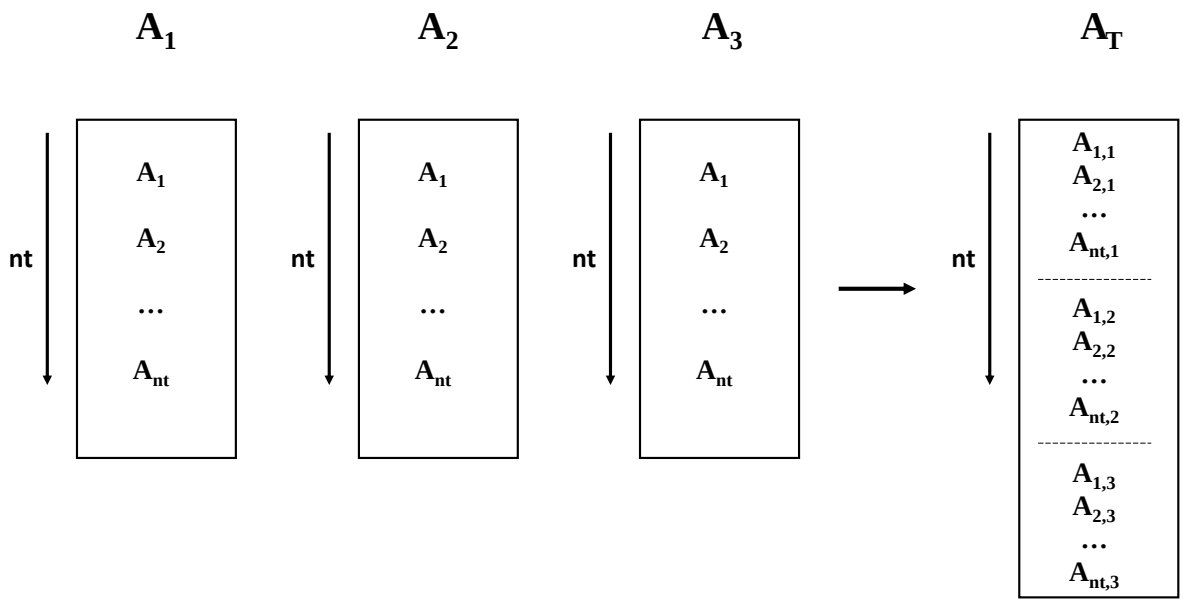

Scheme 2.2: The collocation of multiple absorbance matrices to generate a single matrix for comparison purposes. Absorbance matrices are simply stacked on one another for easy comparison of each reading stipulated in every row.

2.4. Model fitting procedure

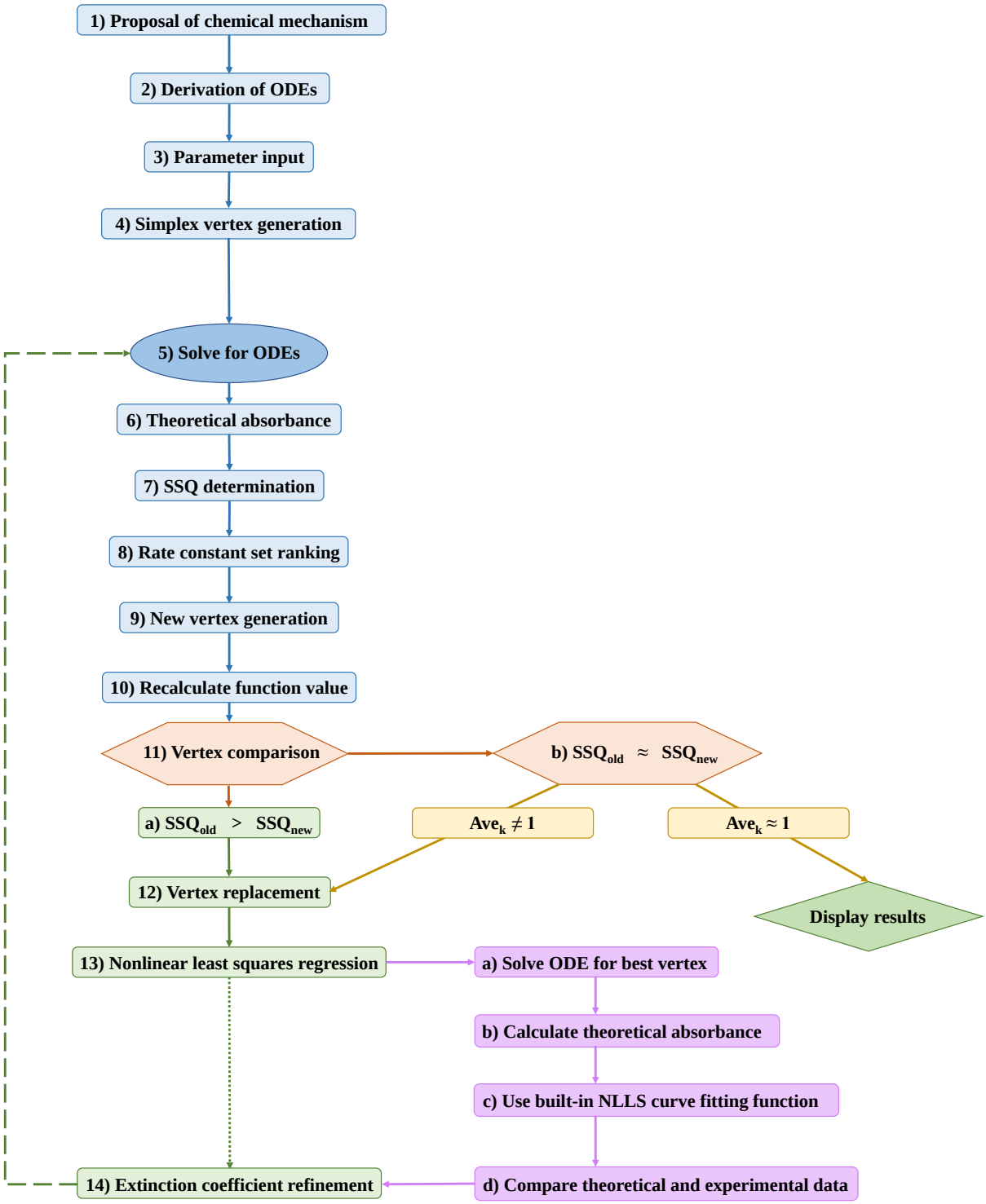

Scheme 2.3: A flow diagram of the RunFit program. The progression of the in-house written program is presented above with the purpose of elucidating the general flow of a kinetic fitting approach to analysing spectrophotometric reaction data.

The first step of the in-house program *RunFit* written in MatLab is to incorporate the proposed chemical model to represent the experimental reactions [Scheme 2.3(1)]. All plausible chemical models regarding viable interactions between reactive species in the sample must be tested as far as possible to provide thorough analysis and hopefully find the reaction mechanism best approximating the experimental data [132]. Regarding the selection of a set of reactions to describe an observed chemical change in a solution, it is based on the concept that increasing the amount of assumptions regarding the underlying mechanism of an observed reaction will decrease the likeliness of the proposed chemical mechanism to be correct. However, it must be considered that a simpler model will not always be able to describe a reaction as accurately as a model with a greater number of reaction steps. Statistical model comparison techniques described further on alleviate this problem when visual inspection fails.

Proposed models are comprised of a set of reaction steps from which a set of ordinary differential equations (ODEs) can be derived [Scheme 2.3(2) and 2.4]. Numerical integration of the derived ODEs using user guess rate constants and initial concentrations yields concentration profiles as a function of time for each species in the sample, generating matrix C. This concentration profile can be used to calculate the theoretical absorbance matrix using the user guess molar extinction coefficients (Scheme 2.4). For the numerical integration of the ODEs, the built-in solver of MatLab, ode23t is employed for its specific use for moderately stiff ODEs [139]. Stiff ODE solvers can use both small and large step sizes in function value analyses to account for the presence of fast and slow reactions in the model proposed.

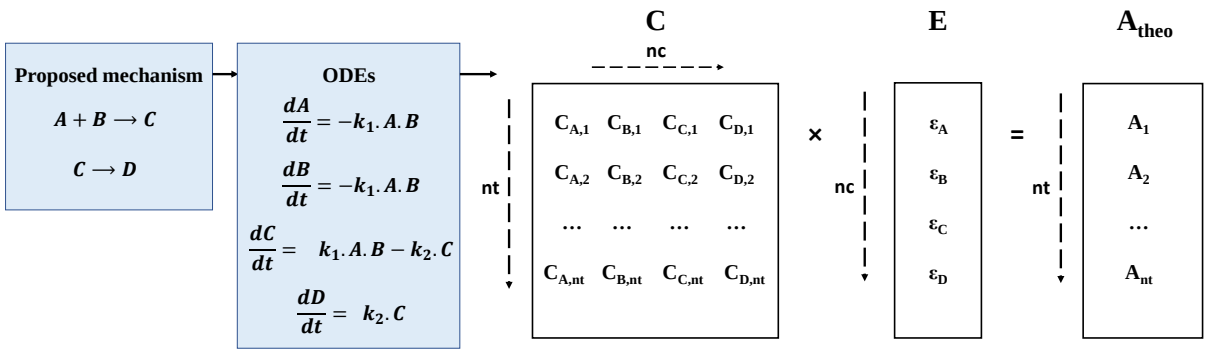

Scheme 2.4: The progression from model to theoretical absorbance data. The reaction steps presented for a chemical mechanism are used to derive ODEs. Numerical integration of ODEs yields concentration profiles. The product of the concentration profile matrix C and extinction coefficient matrix E equals the theoretical absorbance A_{theo} of the proposed model for every time point required.

Subsequently, initial parameter guesses are used for the generation of theoretical absorbance data according to the reaction mechanism proposed [Scheme 2.3(3)]. The initial guess values generally lead to an inaccurate fit of model-generated data versus experimental absorbance and can be manually manipulated by the user to determine a better set of initial parameter values that crudely matches

experimental data in order to decrease computational time. The initial input parameters are refined by an algorithm employed for minimizing the SSQ (Eq. 2.2) in the NLLS fitting procedure.

The algorithm employed in $RunFit$ for minimization of the SSQ is named the Nelder-Mead method, or the downhill simplex algorithm, which is used to explain steps 4 to 12 in Scheme 2.3 [140]. This heuristic algorithm is usually employed in the optimization of nonlinear problems and does not require derivatives. It uses the idea of a simplex, with one more dimension than the number of parameters that must be optimized. In our case, the parameters acting as vertex coordinates are the rate constants contained in the reaction steps of the proposed chemical model. The vertices are formed based on the number of rate constants, thus generating $nr + 1$ coordinate points, where nr simply refers to the number of rate constants. These rate constants (forming the vertices) are stored in a matrix K with nr columns and $nr + 1$ rows. The initial guess rate constants are subjected to a random generation function for the creation of the vertex coordinates [Scheme 2.3(4)].

Consequently, for each row of K, the built-in ODE solver employed by MatLab (ode23t) integrates the set of ODEs derived from the mechanism proposed to determine concentration profiles for each species in the model [Scheme 2.3(5)]. From the concentration profile matrix, the theoretical absorbances are calculated using the vector product of matrix C and extinction coefficient matrix E as shown in Scheme 2.4. The difference between the experimental and theoretical absorbance matrices, A and A', can be used to construct the residual matrix R (Eq. 2.3) for use in goodness-of-fit analysis discussed later.

$$R = A' - A \qquad Eq\ 2.3$$

As such, absorbance matrices are calculated for each set of rate constants [Scheme 2.3(6)] in K, and the function value SSQ of the fit of each set is calculated using equation 2.2 [Scheme 2.3(7)]. The objective function value of a set of rate constants is used to rank it according to the smallest SSQ, as this set would represent the parameters leading to the generation of absorbance data best matching experimentally measured data. The rows of matrix K are then reordered from smallest to highest SSQ with the purpose of replacing the rate constants contained in the last row with an improved set of vertex coordinates [Scheme 2.3(8)].

After generating the simplex and ranking the coordinate sets contained in the rate constant matrix K, the first step of the simplex downhill method is to establish the centroid (c) of the simplex; c is calculated by determining the average of each coordinate point of all vertices excluding the worst point w (Eq. 2.4) (Scheme 2.5(1)). After calculating the simplex centroid, the point of reflection r is calculated by reflecting the coordinates of w over the centroid (Eq. 2.5) (Scheme 2.5(2)). The SSQ function value of r is determined and compared to that of w and the second worst point w_2. As moving from w to any other vertex in the simplex leads to a lowered SSQ function value, the consensus is that moving from w to the centroid is overall an improvement in the SSQ function value estimated from the

coordinates. A reflection away from w is therefore believed a good initial approach at determining a vertex yielding a lower SSQ function value for the fitted absorbance data. If r yields a lower SSQ function value than w as well as w_2, r is extended further from c to create the extended vertex e (Eq. 2.6) (Scheme 2.5(3)) under the premise that if a lower SSQ function value is produced by moving in the coordinate direction followed, perhaps an even better value can be reached by moving the coordinates further. If the extended point yields a lower SSQ than w and w_2, w is replaced by e. If the coordinates of e yields a higher function value than the worst vertex, w is replaced by r. If the SSQ of r is larger or equal to the function value of w, then w and r are contracted towards the simplex centroid (Eq. 2.7 & 8) (Scheme 2.5(4)). The SSQ of both contracted coordinate points $co(r)$ and $co(w)$ are evaluated to determine whether these coordinate sets produce a lower SSQ. The concept states that if the reflection of the worst part of the simplex shape towards a better part does not yield positive results, perhaps the best part is closer towards the centre of the simplex itself. If the contraction vertices lead to better function values than w, the contraction vertex with the lower function value will replace w. In the case that the contraction of w and r does not establish coordinates yielding lower function values, the last plausible step of the simplex downhill method is employed, in which all vertices of the simplex are shrunk towards the best point b (Eq. 2.9) (Scheme 2.5(5)), i.e. the first row of rate constants in the reordered matrix K.

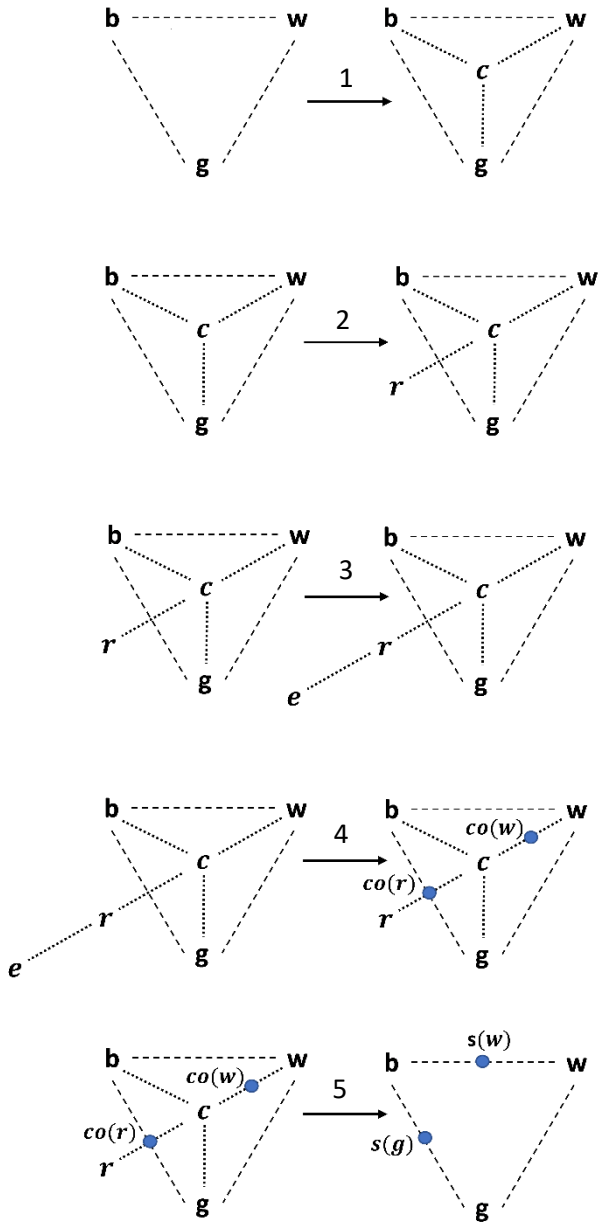

Scheme 2.5: The steps of the Nelder Mead algorithm in objective function minimization. 1) represents centroid determination. 2) depicts the reflection of the worst vertex. 3) denotes the extension of the reflected vertex. 4) represents the contraction of the reflected and worst vertex. 5) depicts the shrinking of all coordinate points towards the best vertex.

$$c = \frac{rc_1 + rc_2 + \cdots + rc_{nr-1}}{nr - 1} \qquad Eq\ 2.4$$

$$r = c + \alpha[c - w] \qquad Eq\ 2.5$$

$$e = c + 2\alpha[r - w] \qquad Eq\ 2.6$$

$$co_r = \frac{r + c}{2} \qquad Eq\ 2.7$$

$$co_w = \frac{w + c}{2} \qquad Eq\ 2.8$$

$$s_{nr} = \frac{rc_{nr} + b}{2} \qquad Eq\ 2.9$$

Consequently, the condensed description is that with every iteration of the simplex algorithm, the worst point will be replaced with a better point [Scheme 2.3(9)], the simplex is reshaped, and the new vertex is analysed to determine the SSQ error [Scheme 2.3(10)] for comparison to the best vertex to determine if criteria for termination of the algorithm are met [Scheme 2.3(11)]. The difference between rate constant values in each row of the rate constant matrix K will become smaller as the vertices converges on a single coordinate set. As the purpose of the simplex method is to converge coordinates to a single set in $nr + 1$ dimensions, the decision was made to use the variation, or rather the lack of variation, of the rate constants as a cessation function. When the division of rate constants from the first row by the last row in matrix K falls in the range of 0.999 and 1.001, convergence is deemed successful as the values can be considered equivalent, and at this point the calculation is terminated with regards to rate constant optimization [Scheme 2.3(11b)]. In the case that the value of this "rate constant division" does not yield a value approaching 1, iteration is continued as the convergence criteria is not met.

After ranking and reordering of matrix K at the start of an iteration, the molar extinction coefficients are optimized. Boundaries are set to ensure that the molar extinction coefficients estimated do not fall beyond a reasonable range. This optimization process is conducted using the built-in non-linear least squares curve fitting function of MatLab. This portion incorporates the use of the best set of rate constants for the numerical integration of ODEs for the ultimate calculation of the theoretical absorbance matrix [Scheme 2.3(13a & b)]. The built-in function compares the theoretical and experimental absorbance matrices [Scheme 2.3(13c)]. The function thus performs NLLS regression on the guess molar extinction coefficients in matrix E for all species presented in the proposed model. Matrix E is then incorporated in the re-evaluation of each row of matrix K with regards to the calculation of the SSQ error of each set, as well as the ranking and reordering. As such the cycle simply repeats from the start of the simplex method again and continues until convergence is obtained in similar manner to a self-consistent field (SCF) optimization [141]. At the termination of the program loop the rate constant sets are averaged and used in combination with the estimated extinction coefficients to

determine the theoretical absorbance of the model. This theoretical absorbance matrix represents the best theoretical fit calculated from the model proposed and can be compared to the experimental data via visual inspection to determine if the model can be considered plausible.

To test the *RunFit* program, UV-Vis data for a reaction model was generated with set rate constants and extinction coefficients using an ODE solver in MatLab. Using the same reaction model along with "false" rate constants and extinction coefficients in *RunFit*, good approximations of the true rate constants and extinction coefficients were obtained. Regarding the fitting of multiple datasets, small changes were made in *RunFit* to conjoin multiple datasets for a single fitting process. This allows for the global optimisation of multivariate kinetic data sets.

While the in-house coded program using MatLab offered great insight into the workings of model-based analysis of measurement data, a problem arising with the simultaneous fitting of multivariate kinetic data sets is the computational expense of such an analysis. The March 2018 release of DynaFit now includes multivariate NLLS regression with the benefit of quick analysis [138]. Due to the fast analysis of multiple models using a method adhering to global optimization, the details of DynaFit are explained for transparency of the fitting procedure. DynaFit was developed in such a way to be user friendly unlike *RunFit*, requiring a relatively simple script file as input (Scheme 2.6). The reaction model in the input script file is converted automatically by the program to a set of ODEs and the program calculates absorbance values from the model using similar techniques as applied for *RunFit*. DynaFit attempts to correlate the calculated absorbance to experimental data using NLLS regression. It allows for changes to be made to the settings regarding multiple aspects of the data fitting process, one of which is the algorithm employed in the least-squares regression (Scheme 2.7). The default algorithm used by DynaFit is the hybrid Trust-Region algorithm NL2SOL, which was first outlined by Dennis *et al.* [142]. However, a choice is given to the user to make use of the Levenberg-Marquardt or the Differential Evolution algorithms [143, 144]. The Differential Evolution algorithm is designed to find a global optimum for model fitting. It is, however, still under development and currently computationally expensive and therefore only the Trust-Region algorithm was employed in model fitting attempts using DynaFit. The next part of this chapter entails the comparison of model fits achieved through NLLS regression to estimate the goodness of each fit.

```
[task]
  data          = progress
  task          = fit
  model         = "model_name"

[settings]
      --Adjust default settings of DynaFit--

[mechanism]
      --Propose plausible elementary reaction steps of model--
            heme + peroxide       <==> radheme              : k1 k2   --Declare names of species and relevant constants
            radheme + abts          --> oxheme + radabts    : k3
            oxheme + abts           --> heme + radabts      : k4

[constants]
      --Declare guess values of rate constants--
  k1 = 0.0014 ? (0.00014 .. 0.014)      --Rate constant may vary between 0,00014 and 0,014
  k2 = 0.0001 ?                         --Rate constant may vary
  k3 = {100, 1, 0.01, 0.0001} ?         --Rate constant may be any of these, estimate which to start with
  k4 = 0.0003                           --Rate constant set, cannot vary

[responses]
      --Declare responses such as molar extinction coefficients--
  radabts = 0.015 ? (0.01 .. 0.02)

[data]
      --Load data from specific folder--
  directory C:\Users\wbergh\Documents\DynaFit4\Data\FC
  extension txt

  sheet "file1_name"
  graph "graph1_name"
   column 1:2,3:4                   | conc heme = 0.30| conc peroxide = 100| conc abts = 2000
   column 7:8,9:10                  | conc heme = 1.00| conc peroxide = 100| conc abts = 2000
      --Single columns of data can be loaded from a text file
  graph "graph2_name"
   column 15:16,17:18,19:20         | conc heme = 0.30| conc peroxide = 100| conc abts = 1500
   column 21:22,23:24               | conc heme = 0.60| conc peroxide = 100| conc abts = 1500
      --Certain variables can be declared for each data set loaded, such as the concentration values here--

  sheet "file2_name"
  graph "graph3_name"
      --Each graph declaration creates a new graph containing data from declared columns--
   column 17:18,19:20               | conc heme = 0.30| conc peroxide = 100| conc abts = 3000
   column 21:22,23:24               | conc heme = 0.60| conc peroxide = 100| conc abts = 3000
  graph "graph4_name"
   column 33:34,35:36               | conc heme = 0.30| conc peroxide = 200| conc abts = 3000
   column 37:38,39:40               | conc heme = 0.60| conc peroxide = 200| conc abts = 3000

[output]
      --Declare designated output folder for files generated by calculations--
  directory C:\Users\wbergh\Documents\FC\Model\t1
;_____________________________________________________________________________________________
```

Scheme 2.6: An example of a script file of DynaFit. Explanations regarding certain components are given in the script following double dashes.

```
[settings]
    --Adjust default settings of DynaFit--
{DynaFit}                                   --Alter basic settings
  PointsParametersRatio       = 100         --Not relevant for the regression statistics
                                            --Used for model analysis and comparison
  DefaultFittingAlgorithm     = TR          --Refers to the algorithm used for nonlinear least squares regression
                                            --Currently set on trust-region

 {TrustRegion}                              --Names of variables altered explain the function of said variables
  IterationsPerParameter      = 1000
  FunctionCallsPerParamter    = 2000

 {Marquardt}
  IterationsPerParameter      = 500         --Amount of iterations for each adjustable parameter
  RobustFit                   = n           --If yes, robust regression analysis is conducted
                                            --Uses Huber's mini max method
  Restarts                    = 15          --Number of restarts after the presumed least-squares minimum is reached
                                            --To ensure approximations do not vary between runs
  RestartPertubation          = 0.1         --Maximum random fractional change in each adjustable model parameter upon restarting
                                            --Allows for refitting of model using estimated parameters for cases where the
                                              results yielded can still be refined
  EqualizeDatasets            = y           --Allows for global fits by considering different data set sizes to ensure equal weight is given

 {ConfidenceIntervals}
  LevelPercent                = 95          --Probability level for confidence intervals
  MaxSteps                    = 50          --Steps taken in profile-t search algorithm
  JointProbability            = n           --If yes, determines joint confidence region, which is less optimistic, but more realistic
                                            --If no, determines limits of marginal confidence intervals
  SquaresIncreasePercent      = 10          --Using a continuous assay, so necessary
                                            --Could also be 5. If not continuous, set to 0
  MaxRefitIterations          = 2           --Amount of restarts allowed based on results of the confidence value interval search

 {DifferentialEvolution}                    --Algorithm unstable, computationally expensive
  MaximumEvolutions           = 5
  OutputTextFileType          = txt

 {Constraints}
  Concentrations              = 0.01        --Variation in concentrations declared. Set to 1 percent allowed

 {Output}                                   --Graph settings, output file settings
  BlackBackground             = n
  XAxisLabel                  = Time
  XAxisUnit                   = min
  YAxisLabel                  = A_385

 {Filter}
  AverageReplicates           = y           --More than one reading for the same conditions, automatically average

 {EstimateScan}
  EstimatesMax                = 10000       --Amount of initial estimates allowed for rate constants before fitting
```

Scheme 2.7: Adjustments of DynaFit default settings, with explanations as before

2.5. Evaluating goodness of fits between models

While NLLS analysis of data yields a wealth of information regarding the proposed model, it does not necessarily help when choosing between multiple plausible models. Thus, model fits need to be evaluated to determine which offers the best depiction of the "true" reaction or reaction sequences. However, the individual models must be analysed to first determine the goodness-of-fit for each. To evaluate the goodness-of-fit of a proposed reaction model, one can start with simple visual inspection of the theoretical absorbance matrix A' versus the experimental A. This will yield insight into whether the model can be considered for further evaluation. If the matrices correlate well, residual plots can be generated using the residual matrix R (Eq. 2.3) to inspect whether the differences between A and A' are random or systematic. In many cases this is enough to select one model over another. Systematic error here refers mostly to a sinusoidal distribution of residuals. Observing systematic error would signify that the reaction model proposed is incorrect. Random error is recognized by the uncorrelated scatter of residuals, indicating that the model fitted can function as a plausible depiction of the experimental kinetic data. To understand how random and systematic deviation would present itself regarding absorbance data, a visual presentation is given in Figure 2.1.

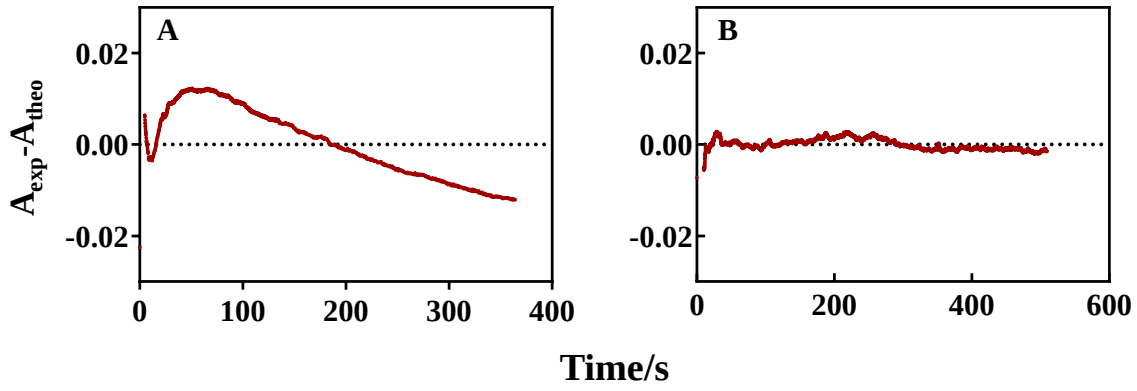

Figure 2.1: Comparison of deviations. A) represents systematic deviation, noted by its non-random deviation from zero (experimental data). B) denotes random deviation, known for the random scattering of theoretical data around experimental data.

For models that pass visual inspection, the relative root of mean square (rRMS), otherwise called the root-mean-square percentage deviation, can then be used to interpret the goodness of fit (Eq. 2.10) in a similar manner to the SSQ value.

$$rRMS = \sqrt{\frac{\sum_{i=1}^{nt}(A_i - A'_i)^2}{nt}} \times 100 \qquad Eq.2.10$$

This equation represents the aggregated prediction error of the model as a percentage. The rRMS value is influenced by the size of data sets, where adding more reaction steps to the proposed reaction model tends to improve this statistic regardless of possible over-parameterization. For data set size limits, a normal consent is that the ratio of the number of data points to the number of parameters to be refined must remain above 100 to ensure results obtained are accurate [132]. While the size of data used will not present a problem in this study, as the data points surpass a thousand in number for data used in model-based analysis, the issue remains that this statistic cannot account for the increased complexity of a model. Thus, the rRMS can be used as a more useful version of visual inspection, as the goodness-of-fit of a model can be crudely quantified. The SSQ statistic of a model follows the same trend as rRMS for increasing complexity of reaction models. As with the rRMS, the SSQ offers only a rough indication of goodness of model fit.

A regression statistic offering a better evaluation of model goodness of fit is the Chi-Square test (Eq. 2.11), a test to determine whether the observed distribution of A' differs significantly from that of A.

$$\chi^2 = \sum_{i=1}^{nt} \frac{(A_i - A'_i)^2}{A'_i} \qquad Eq.2.11$$

For the equation above, the smaller the value obtained for this statistic, the better the model represents the experimental data. According to Hibbert and Thordarson, χ^2 represents the limiting distribution of the model [145]. Consequently, it gives an indication of how much of the experimental data the model does not account for, therefore somewhat similar to, although more valuable than, the result obtained from calculating the rRMS. The higher regard for this statistic stems from its use to test whether results obtained from a proposed reaction model may be significant. This is done using the degrees of freedom of the system (Eq. 2.12), and the Chi-Square distribution table.

$$df = nt - v \qquad Eq\ 2.12$$

In the above equation, df denotes the degrees of freedom, while v represents the number of parameters approximated for a model. As distribution tables are also used for the F-test, to be discussed further in the chapter, a short explanation is due. A confidence level is chosen for the data, representing the percentage error one is willing to overlook for the model fits achieved. For example, if a 95 % confidence level is chosen, the goodness of a model fit will be considered significant if it falls within an error margin of 5 %. The confidence level chosen along with the degrees of freedom of the proposed model is used to navigate the distribution table to find the corresponding range of values within which the statistic may fall. If the Chi-Square statistic falls within this range, the result is considered

meaningful. Viña *et al.* analysed the significance of their results on studying alignment-free drug-target complex predictions by utilizing this method [146]. The distribution table offers the benefit of taking the complexity of models into account, thus accounting for possible over-parameterization of reaction models. However, for models encompassing the same number of parameters, the Chi-Square statistic can be used for simple model comparisons, assuming the size of the data remains constant. For example, in a regression analysis test conducted by Yuh-Shan Ho on the selection of sorption isotherms, the Chi-Square statistic is employed as a model goodness of fit statistic to indicate which isotherm is best for adsorption [147]. The lowest Chi-Squared statistic is believed to represent the best fitting isotherm. For this study, the Chi-squared is utilised as a test for model stability, such as the method used by Yuh-Shan Ho [147]. This test therefore offers a more reliable method of determining goodness-of-fit than either the rRMS or SSQ value.

For the analysis of individual model stability, the rRMS, SSQ and Chi-Square statistics will be used. These three methods will serve as controls to analyse the goodness of fit of a proposed model. However, as the complexity of a model can lead to bias amongst these statistical values, methods of model comparison accounting for this problem are also needed.

Three robust methods used for the quantitative comparison of model goodness of fit include the Kullback-Leibler Divergence (KLD), the Akaike Information Criterion (AIC) and the Bayesian Information Criterion (BIC) methods (Eq. 2.15, 2.16 and 2.17), respectively [148, 149, 150]. All three methods can account for the complexity level of models. Both the AIC and BIC can only be used for comparative functions, while the KLD offers more information regarding the goodness of fit of models [151, 152]. The AIC and BIC are penalized-likelihood criteria, thus penalizing more complicated models to determine if the improvement in fit is due to the complexity level of the model, or due to the model representing the kinetic data more significantly [134]. The KLD value represents the information lost by a model in describing the kinetic reaction studied [152].

$$KLD = \sum_{i=1}^{nt} \ln\left(\frac{A_i}{A'_i}\right).A_i \qquad Eq.\,2.15$$

$$AIC = nt.\ln\left(\frac{SSQ}{nt}\right) + 2(v) \qquad Eq.\,2.16$$

$$BIC = nt.\ln\left(\frac{SSQ}{nt}\right) + \ln(nt)\,.\,(v) \qquad Eq.\,2.17$$

The information criteria presented above are used for the comparison of regression models. The original equations were adapted from maximum likelihood estimations. As such, the KLD method can be used in a comparative manner, offering information regarding model goodness of fit, while the AIC and BIC

statistics can only be used comparatively. All three statistics are incorporated in the analysis of goodness of model fits to ensure statistics obtained from the analysis agree for a model.

The use of hypothesis testing, such as the traditional null hypothesis (H_0) method, was not used as hypothesis testing for model selection is often poor [134]. Furthermore, using hypothesis testing with a fixed α level (or allowed error percentage) as a basis for model selection is not fully supported by statistical theory. There are no general formal rules, nor guidelines, that clearly define how to use the various methods available for hypothesis testing [153]. Another issue that arises is the fact that non-nested models cannot be tested either [134]. A nested model is one you can always obtain by removing or constraining some parameters from a more complex model [151]. For example, one model is nested in another if the second model contains an added reaction step to the first model mechanism proposed. As this thesis contains non-nested models as well, this poses a problem when considering the use of hypothesis testing, as hypothesis testing shows if an addition of a reaction step to a model leads to a significantly improved fit, thus only applying to nested models. Moreover, the order of models tested are arbitrary, along with the α level used in testing, as different α levels can lead to vast differences between selected models [154–156]. As recent advances in computational technology allows for more refined procedures which can indicate without varying result that one model surpasses another, hypothesis testing was excluded from the model comparison analysis. The AIC, BIC and KLD will be used to ensure any model that may comprise too many parameters, thus being overparameterized, is pinpointed and thus rejected from the analysis.

2.6. Concluding remarks

The method of analysis used for this study is model-based, and due to the type of kinetic data collected, NLLS regression fitting is necessary. As such, the in-house coded program *RunFit* in MatLab for the analysis of multivariate kinetic data has been used to elucidate the process by which such an analysis can progress. *RunFit* can still be developed further to incorporate other model-based analysis methods to improve its regressional capabilities. Using *RunFit* is computationally expensive, consuming too much time in the analysis of a single proposed model. The problem may be circumvented in future development of *RunFit*, or development of MatLab software itself. To alleviate the time consumption, DynaFit was used to optimise parameters using the Trust-Region algorithm, due to its relatively fast analysis. *RunFit* was used in cases where the output of DynaFit appears dubious to ensure the accuracy of said output. Goodness of fit analysis of model fits has been elucidated to explain the statistical approaches utilised. As statistical functions such as the SSQ and Chi-Square test does not account for

the level of complexity of proposed models, AIC, BIC and KLD are used in analysis involving the assessment of model plausibility.

3. The Reaction between Fe(III)PPIX and Hydrogen Peroxide

3.1. Introduction

Fe(III)PPIX is an important moiety in a diverse variety of proteins that plays a crucial role in biological functions, as discussed in chapter 1. van Eldik and co-workers showed that high-valent iron oxo species such as Fe(III)PPIX are vitally important in enzymatic execution of oxidation reactions due to the high-valent iron centre of the porphyrin molecule [70, 157]. The reaction between Fe(III)PPIX and hydrogen peroxide is key to understand the peroxidase-like activity of the metalloporphyrin. Insight into the underlying mechanism will assist in elucidating the toxicity of free haem in the malaria parasite.

The peroxidase reaction (Eq. 2.1) catalysed by iron(III) porphyrins has been studied extensively, as it could yield information regarding the function or mechanisms mediated by catalase and peroxidase enzymes containing iron-porphyrin moieties [158–160]. Iron(III) porphyrins can facilitate catalase and peroxidase activity; however, this study will only focus on the peroxidase activity of Fe(III)PPIX (Eq. 3.1) in aqueous media at a pH of 7.5.

$$2RH + H_2O_2 \rightarrow 2H_2O + 2R \qquad Eq\ 3.1$$

$$RH - reducing\ substrate\ such\ as\ Fe(III)PPIX$$

Multiple reaction mechanisms have been suggested for the reaction between iron-containing porphyrins and hydrogen peroxide H_2O_2. In the 1983 study conducted by Jones *et al.*, it was proposed that the reactions of certain iron(III) porphyrins with H_2O_2 might be a one-step, non-reversible reaction (Eq. 3.2) generating an oxidized radical iron porphyrin species [$Fe^{\bullet+}$(IV) porphyrin] and water [159].

$$Fe(III)PPIX + H_2O_2 \longrightarrow Fe^{\bullet+}(IV)PPIX + H_2O \qquad Eq\ 3.2$$

In 1995, de Almeida Ribeiro *et al.* inferred a scheme for the reaction between Fe(III)PPIX and H_2O_2 based on spectrophotometric studies of the peroxidase activity of Fe(III)PPIX, and the effect chloroquine elicits on this activity [74]. They proposed that the interaction between Fe(III)PPIX and H_2O_2 occurs via a two-step mechanism. The first step involves association between the compounds to form a peroxohaem complex [Fe(III)PPIX.H_2O_2] (Eq. 3.3) and the second step leads to the formation of $Fe^{\bullet+}$(IV)PPIX (Eq. 3.4) or oxidized porphyrin [Fe(IV)=O] (Eq. 3.5), depending on whether the mechanism of the H_2O_2 O-O bond cleavage occurs heterolytically or homolytically, respectively.

$$Fe(III)PPIX + H_2O_2 \rightleftharpoons Fe(III)PPIX.H_2O_2 \qquad Eq\ 3.3$$

$$Fe(III)PPIX.H_2O_2 \rightarrow Fe^{\bullet+}(IV)PPIX{=}O + H_2O \qquad Eq\ 3.4$$

$$Fe(III)PPIX.H_2O_2 \rightarrow Fe(IV)PPIX{=}O + HO^{\bullet} + H^{+} \qquad Eq\ 3.5$$

In 1986, Zipplies *et al.* used spectrophotometric measurements at a temperature of 30 °C to determine the influence of pH on Fe(III) tetraphenylporphyrin (TPP) catalyzed degradation of H_2O_2 [73]. The

mechanism proposed by Zipplies *et al.* involves the complexation between Fe(III)TPP and H_2O_2 to form the peroxohaem complex (Eq. 3.3), via various modes of coordination, which then undergoes cleavage of the H_2O_2 O-O bond to produce $Fe^{\bullet+}$(IV)TPP at a pH of 7.0 (Eq. 3.4) [73]. Tatsuma and Watanabe used Fe(III)PPIX nonapeptide infused electrodes to detect the presence of H_2O_2 in a solution, and came to a conclusion that Fe(III)PPIX and H_2O_2 reacted in a similar manner to models proposed by de Almeida Ribeiro *et al.* and Zipples *et al.*, apart from changing the initial complexation step to a non-reversible reaction [73,74,161].

Baek and van Wart studied the formation of horseradish peroxidase (HRP) compound 1 [$Fe^{\bullet+}$(IV)PPIX] using low-temperature (-36 to 25 °C) stopped-flow kinetics at pH values of 5.5, 7.5 and 9.0, leading to the proposal of two mechanisms [158]. The first model proposed at 25 °C is akin to the mechanism recommended by de Almeida Ribeiro *et al.*, however, they refer to the last formed porphyrin complex as a "discrete, catalytically active reaction intermediate", represented as $Fe^{\bullet+}$(IV)PPIX by de Almeida Ribeiro *et al.* [74]. The second model for the interaction between Fe(III)PPIX and H_2O_2 involves the formation of an intermediate (Eq. 3.6 and 3.7) at pH 7.5 and -35 °C, believed to be an oxidized form of hematin prior to the formation of the porphyrin radical. This intermediate formation is deemed reversible, although the conversion of the intermediate to $Fe^{\bullet+}$(IV)PPIX is not reversible in this model.

$$Fe(III)PPIX.H_2O_2 \rightleftharpoons Intermediate \qquad Eq\ 3.6$$

$$Intermediate \rightarrow Fe^{\bullet+}(IV)PPIX{=}O + H_2O \qquad Eq\ 3.7$$

van Eldik and co-workers studied the reaction between Fe(III) octa-anionic porphyrin (P^{-8}) and H_2O_2 at a variety of pH values at 4 °C using stopped-flow spectrophotometry [70]. The reaction model proposed by van Eldik is similar to the model proposed by de Almeida Ribeiro *et al.*, with the addition of a degradation pathway for $Fe^{\bullet+}$(IV)PPIX (Eq. 3.8) [74].

$$Fe^{+\bullet}(IV)P^{-8}{=}O \rightarrow Degradation\ Products \qquad Eq\ 3.8$$

Both van Eldik and co-workers, as well as de Almeida Ribeiro *et al.* focused on the effect of pH for possible homo- and heterolytic pathways of the Fe(III) porphyrin and H_2O_2 reaction. They concluded that under physiological conditions and in acidic systems, heterolytic cleavage of the H_2O_2 O-O bond will predominate (Eq. 3.4) whereas homolytic cleavage only occurred under basic/aprotic conditions [70, 74].

Aspects of the reaction mechanism to also consider include the non-covalent dimerization of Fe(III)PPIX in aqueous solution (Eq. 3.9a, k_f represents the forward reaction and k_r represents the reverse reaction), as well as the role that dimeric Fe(III)PPIX might play in the reaction kinetics. According to Jones *et al.*, dimeric Fe(III)PPIX present in the solution can also react with H_2O_2, producing an oxidized "dimer" intermediate [159]. This reaction is reported to be insignificant in protoferrihaems, as used in this study, in comparison to other ferrihaem analogues, suggesting the

exclusion of this reaction from the mechanism for Fe(III)PPIX and H_2O_2 interaction. They furthermore state, in accordance to findings by de Almeida Ribeiro *et al.*, that monomeric Fe(III)PPIX present in the solution serves as the main catalyst involved in the reaction, hence indicating that while dimeric Fe(III)PPIX is present it will not affect the consumption of H_2O_2 present nor the oxidation of radical scavengers [74]. de Almeida Ribeiro *et al.* concluded that the reaction between Fe(III)PPIX dimers and H_2O_2 can be excluded from the mechanism, as it takes simple one-electron redox processes to reproduce the original catalyst [74]. Brown *et al.* determined conditional dimerization constants $K_d = 4.7 \times 10^6$ and 10.5×10^6 (Eq. 3.9b) at respective pH's 6.98 and 7.38 and a temperature of 25 °C in phosphate buffer, for the dimerization of Fe(III)PPIX [162]. It is important to note that conditional dimerization constants are obtained at a particular pH, thus the extent of dimerization will increase or decrease with variation in pH (Eq. 3.9c). de Villiers *et al.*, calculated Fe(III)PPIX conditional dimerization constants of $K_d = 3.98 \times 10^6$ and 6.61×10^6, at respective pH's 6.89 and 7.43 in aqueous solution at 26 °C using HEPES (4-(2-hydroxyethyl)-1-piperazineethanesulfonic acid) buffer, which is in good agreement with the values calculated by Brown *et al.* [159, 162]. In subsequent equations presented, H_M represents monomeric Fe(III)PPIX and H_D denotes dimeric Fe(III)PPIX.

$$2H_M \rightleftharpoons H_D \qquad Eq.3.9a$$

$$K_d = \frac{H_D}{{H_M}^2} \qquad Eq.3.9b$$

$$K_d' = K_d.[H^+] \qquad Eq.3.9c$$

In a review by Jones, regarding the mechanism for porphyrin radical formation and the role of water released during the reaction, it is assumed that the complexation between HRP and H_2O_2 is followed by a non-reversible conversion of a peroxohaem complex to a porphyrin radical-water complex (Eq. 3.10) [163]. This step is followed by a reversible water coordination and release of the radical-water complex (Eq. 3.11).

$$HRP.H_2O_2 \rightarrow HRP^{\bullet+}.H_2O \qquad Eq\ 3.10$$

$$HRP^{\bullet+}.H_2O \rightleftharpoons HRP^{\bullet+} + H_2O \qquad Eq.3.11$$

Jones concluded that under physiologically-relevant conditions, the resident water molecule does not affect the peroxidase activity, and rather assists in the function of haemoproteins, such as horseradish peroxidase, myeloperoxidase and chloroperoxidase [163]. The water molecule is believed to shield the prosthetic haem porphyrin group from potential oxidants following the formation of radical haem. This allows for the reduction of the ferryl iron centre of the porphyrin to occur via two 1-electron equivalent reactions.

As the reaction between Fe(III)PPIX and H_2O_2 forms part of a portion of a full Fe(III)PPIX-mediated peroxidase cycle, of which Figure 1.3 presented in the introduction is one possible sequence of reactions, it was deemed necessary to first conduct a kinetic study of the interaction between Fe(III)PPIX and H_2O_2. In this manner it is hoped to reduce the number of parameters (rate constants and extinction coefficients) that must be calculated for the full cycle, e.g. Figure 1.3, from non-linear least squares analysis of UV-vis kinetic data.

3.2. Experimental Methods

3.2.1. Instrumentation

For the spectrophotometric studies, a Shimadzu UV-1800 spectrophotometer was used for the determination of experimental absorbance values, in combination with an electronic thermos-controlled cell holder to regulate the temperature of solutions contained in the cuvettes. A Memmert WND 14 water bath was employed for the equilibration of solutions to physiologically relevant temperatures before addition to the cuvettes for spectrophotometric reading. A BOECO vortex mixer V1 Plus was used to ensure homogeneity of liquid solution mixtures prior to addition to cuvettes. Other than the vortex employed, an UD100SH-3LQ Ultrasonic Cleaner bath was utilized for sonicating reagent solutions to ensure all reagents used dissolved in solution. SUPRASIL Quartz cuvettes of 1 cm pathlengths were used for the spectrophotometric measurements. Regarding the preparation of the reagent solutions, Gilson Pipetman single-channel pipettes were utilized for the dilution and preparation of solutions. An A&D HR-200 analytical balance was used for the accurate weighing of chemicals for the making of stock solutions. For the preparation of buffer solutions, a JK-MSH-Pro magnetic stirrer hotplate was used in combination with a Mettler Toledo FE20 pH meter calibrated with CRISON pH standards.

3.2.2. Experimental procedures

Stock solution preparation

130 mM Tris buffer solution

Dissolve 1.57 g Tris-(hydroxymethyl)-aminomethane in distilled water in a 100 ml volumetric flask and adjust pH to 7.4 using HCl. Make up to volume using distilled water.

1.0 M Sodium Hydroxide

Dissolve 1.00 g sodium hydroxide in distilled water in a 500 ml volumetric flask. Make up to volume using distilled water.

1.0 mM haem

Dissolve 3.2 mg hemin in 1.0 M sodium hydroxide in a 5 ml volumetric flask. Make up to volume using sodium hydroxide. Use a sonicator to dissolve compound completely.

50 mM Hydrogen Peroxide

Dilute 100 µL 30 % hydrogen peroxide in a 50 ml volumetric flask using distilled water. Make up to volume using distilled water.

10 mM Hydrogen Peroxide

Dilute 20 µL 30 % hydrogen peroxide in a 50 mL volumetric flask using distilled water. Make up to volume using distilled water.

1.0 mM Hydrogen Peroxide

Dilute the 10 mM stock solution in a 1:9 ratio to dH_2O in a 50 ml volumetric flask. Make up to volume using distilled water.

Experimental protocol for kinetic runs

1 M Sodium hydroxide stock solution was made for the washing of glassware that has been in contact with hemin solution, as prescribed for cleaning hemin contaminated glassware [92]. The homogeneity of any mixture of chemical stock solutions were ensured using the vortex spinner to properly mix solution components together. Prior to time or concentration assays, reaction solutions used in the experiments were equilibrated to 37 °C using a water bath to ensure the kinetic data collected spectrophotometrically represents the reaction under a physiologically relevant temperature.

For initial spectrophotometric readings, full spectra of Fe(III)PPIX for wavelengths ranging between 250 and 700 nm were recorded at a scan speed of 1000 nm/min. Kinetic data for analysis was recorded at a single wavelength corresponding to the soret band of Fe(II)PPIX, for 0.1 s time periods to ensure the initial reaction can be followed in more detail. Experiments were conducted in triplicate. For every different reaction of Fe(III)PPIX presented in this section, the reference cuvette contained all elements present in the measuring cuvette, except for Fe(III)PPIX, the component for which the absorbance is measured. All experiments were conducted under physiologically relevant pH (7.5) and temperature (37 °C) unless stated otherwise to ensure results obtained are relevant to the malarial system it is based on. Varying concentrations of Fe(III)PPIX and H_2O_2 were used in experimentation to ensure fits performed condone to requirements of multivariate global analysis as discussed in chapter 2.

3.2.3. Computational details

As discussed in the previous chapter, model fitting complications can occur when either over parameterizing the proposed reaction steps or when using a very simplified model. As such, several regression tactics were employed to determine which model fits the experimental data best. For each general reaction model, the fitted sub models are presented with graphs depicting the experimental data sets and theoretical fitted data for every model extension constructed according to literature study of proposed models for the reaction of H_2O_2 with Fe(III) porphyrins. The optimized sets of rate constants and extinction coefficients generated by DynaFit for the models of every set are tabulated, including the extinction coefficients for all light absorbing species. Residual plots of the graphs presented for every model set are also presented to ease the comparison of goodness-of-fit of models. The most viable proposed reaction steps would subsequently be used in modelling the full peroxidase cycle, as parameter estimates obtained by this fitting can be incorporated into the full peroxidase-like mechanism.

3.3. Results and Discussion

The UV-Vis spectrum of Fe(III)PPIX in aqueous solution was measured to show the absorbance of Fe(III)PPIX in the wavelength range used in this study (Figure 3.1).

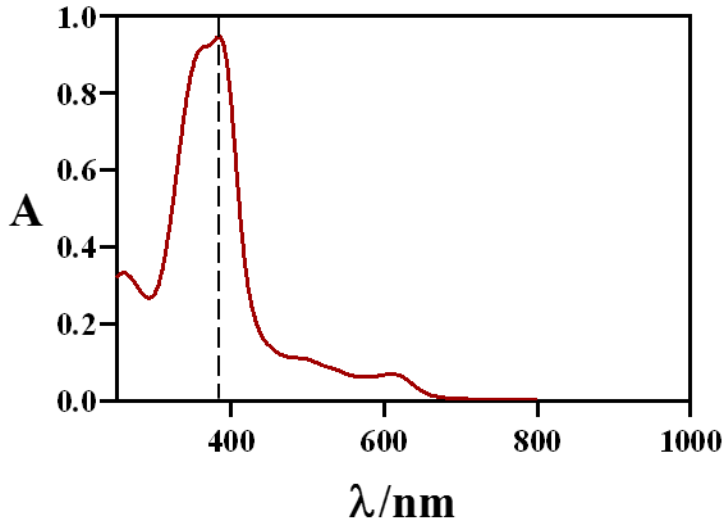

Figure 3.1: The full spectrum of Fe(III)PPIX absorbance. A concentration of 20 µM Fe(III)PPIX was made up in aqueous solution and measured spectrophotometrically in the wavelength range of 250 to 800 nm.

The maximum absorbance of Fe(III)PPIX in aqueous solution occurs at 385 nm, as indicated by the dashed line. A second absorbance maximum at a slightly lower wavelength can be observed. The former is indicative of monomeric Fe(III)PPIX, while the latter denotes the dimeric Fe(III)PPIX present in the reaction solution [164]. For the collection of reaction data, absorbance measurements are taken per time interval at 385 nm, as monomeric Fe(III)PPIX is the catalytically active species present in the solution [159]. Regarding the full spectrum of Fe(III)PPIX, the porphyrin absorbs in a wide wavelength range including wavelengths from lower than 250 nm to around 660 nm.

After the full spectrum was obtained, various concentration ratios were investigated to ensure conditions required for use of multivariate global analysis is justified. For the variation of H_2O_2 concentration, Fe(III)PPIX was fixed at a concentration of 10 µM (Figure 3.2A). For variations of Fe(III)PPIX concentration in the reaction mixture, H_2O_2 was fixed at a concentration of 100 µM (Figure 3.2B). Absorbance was recorded in 30 second intervals at 385 nm under physiologically relevant conditions.

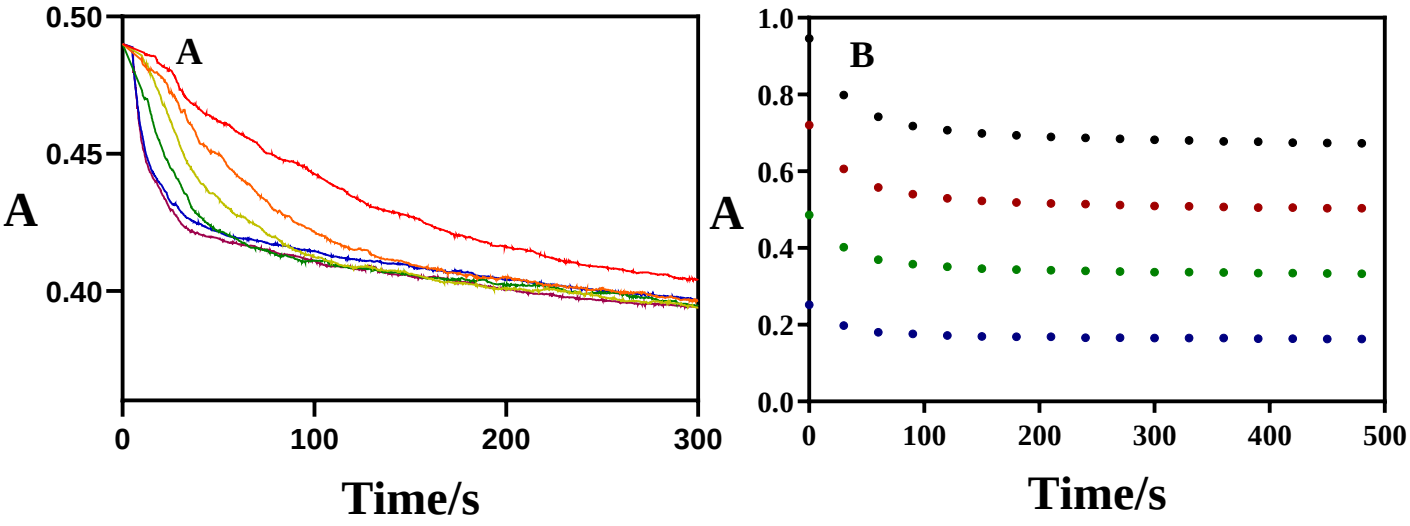

Figure 3.2: The reaction between Fe(III)PPIX and H_2O_2. A) The reaction of Fe(III)PPIX and H_2O_2 with Fe(III)PPIX at a fixed concentration of 10 µM, and H_2O_2 at concentrations of 40 (red), 80 (orange), 150 (gold), 300 (green), 800 (purple) and 1000 (blue) µM. B) The reaction of Fe(III)PPIX and H_2O_2 at a fixed H_2O_2 concentration of 100 µM and Fe(III)PPIX concentrations of 5 (blue), 10 (green), 15 (red) and 20 (black) µM. The data were collected spectrophotometrically at 385 nm.

The final product of this reaction is $Fe^{\bullet+}$(IV)PPIX=O [70,74]. The UV-Vis spectrum of this compound has lower extinction coefficient over the wavelength range compared to Fe(III)PPIX. Therefore, as the reaction progresses the absorbance readings continually decrease barring possible intermediates which may have higher extinction coefficients at some wavelengths. When the concentrations of either Fe(III)PPIX or H_2O_2 are increased the reaction rate also increases, thus attesting for the decrease observed in initial absorbance readings. The decrease in absorbance will be used to determine the initial rate of the reaction. It must be noted that a 30 second recording interval was too large to obtain enough data in the initial stages of the reaction. Consequently, new data was collected using the same protocol, however measuring absorbance for 0.1 second intervals (Figure 3.3).

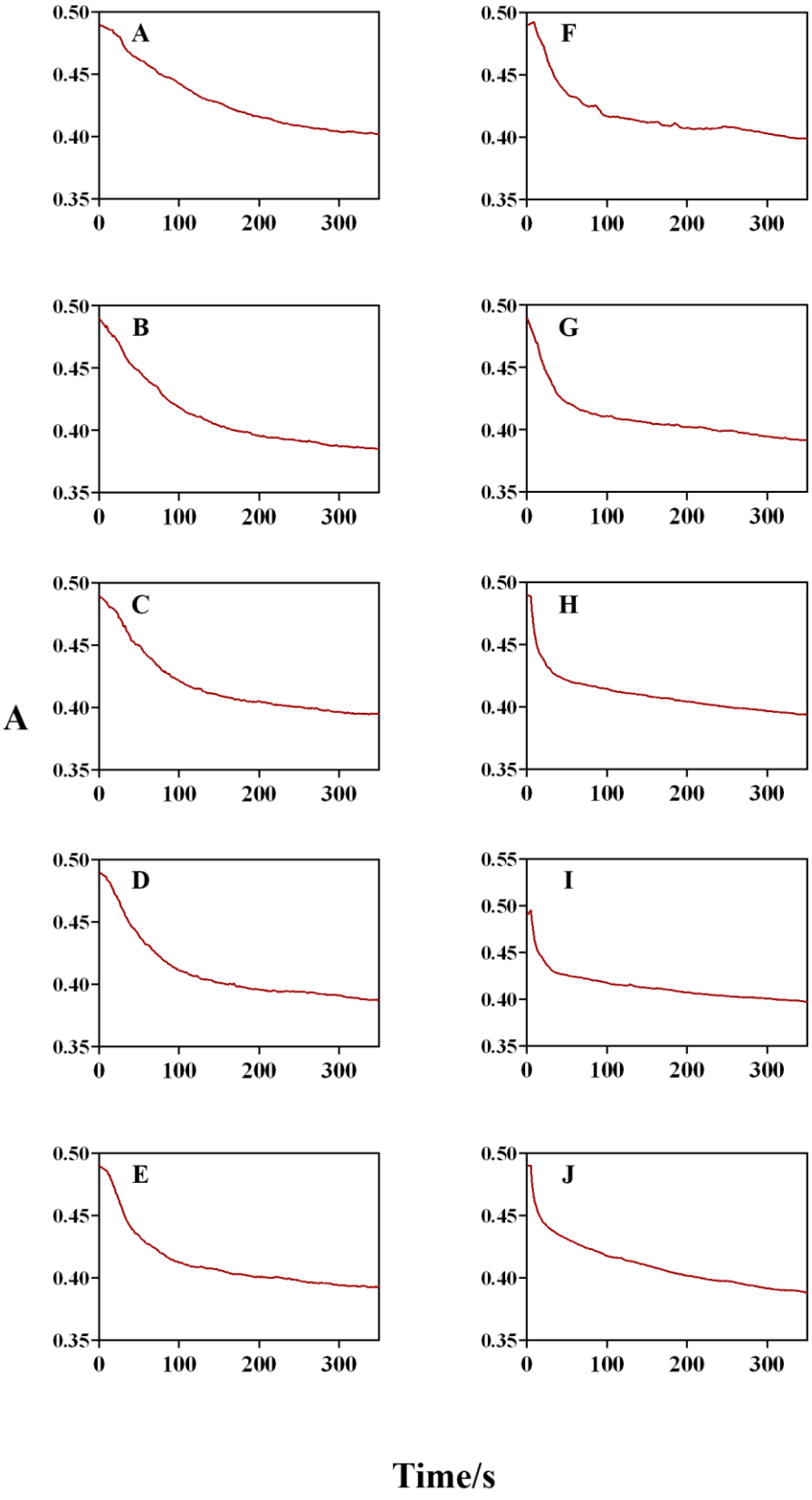

Figure 3.3: The reaction of Fe(III)PPIX and H_2O_2. The absorbance signal of the reaction was collected at 385 nm for 0.1 second intervals. Fe(III)PPIX concentration was kept constant at 10 µM. H_2O_2 concentration for graphs A to J are 40, 60, 80, 100, 150, 200, 300, 800, 1000 and 2000 µM respectively

3.3.1. Model set 1

The general mechanism of model 1 is based on the model proposed by Jones *et al*. in 1983 [159]. The mechanism is represented by a one-step second-order reaction. Fe(III)PPIX and H_2O_2 react to form $Fe^{\bullet+}$(IV)PPIX (Eq. 3.2, p1). This model is an excellent example of an overly simplistic model, with too few components to fully describe the underlying mechanism of the reaction studied. It is included to ensure goodness-of-fit regression analysis employed would indicate this model is inadequate when compared to more complex models presented further on. However, there is of course a chance that as the simpler model is sometimes more likely the correct one that this model could result in a better fit than expected.

We know from the onset that Fe(III)PPIX dimerization also occurs [165]. The dimerization reaction is known to be exceptionally fast, and as such the premise is made that the dimerization reaction is at equilibrium while other reactions are occurring at a much slower rate [166]. Thus, the change in concentration of dimer and monomer is much higher than for other species partaking in the reaction, yielding a stiff ordinary differential equation (ODE) problem. Stiff, because the ODEs incorporating the dimerization reaction, and any other reaction in the system, would have solutions that change rapidly and slowly, respectively. This dictates the use of very small step sizes in the numerical approximation for steps taken to converge on a solution for the ODEs presented. Subsequently, it will be computationally difficult to model the dimerization reaction correctly.

To solve this problem, we make use of the fact that for all intents and purposes the dimerization reaction is always at equilibrium. Thus, the fraction of monomeric Fe(III)PPIX (Eq. 3.12), or dimeric for that matter, present in the mixture relative to the total metal porphyrin concentration (Eq. 3.13) will remain constant throughout the reaction (Eq. 3.9b).

$$x_M = \frac{H_M}{H_M + 2H_D} = \frac{H_M}{T_p} \qquad Eq.3.12$$

$$T_P = H_M + 2H_D \qquad Eq.3.13$$

Consequently, dimerization can be accounted for indirectly in the proposed reaction models, under the premise that the mole fraction of monomeric Fe(III)PPIX present in the solution will remain the same throughout the reaction. Consider the two reactions, Eq. 3.9a (p3) and 3.14, where it is assumed that only the monomer porphyrin reacts with peroxide.

$$H_M + H_2O_2 \xrightarrow{k_{robs}} H_M{}^{\bullet+}\,(IV) \qquad Eq.3.14$$

Before moving on, the following should be noted as we are working with UV-Vis data. Since the dimerization reaction is at equilibrium whilst the reaction represented by equation 3.14 is occurring, the

UV-vis spectra of H_M and H_D can be approximated with one combined UV-Vis spectrum with the use of weighted molar extinction coefficients (Eq. 3.15), determined using the monomer and dimer mole fractions, which will remain constant for the duration of the reaction.

$$\varepsilon_W = \varepsilon_M.\frac{[H_M]}{[T_P]} + \varepsilon_D.\frac{[H_D]}{[T_P]} = \varepsilon_M.x_M + \varepsilon_D.x_D \qquad Eq.3.15$$

The ODE for monomeric Fe(III)PPIX for the reaction model presented by Eq. 3.9a and 3.14 is shown in equation 3.16, where k_1 represents the rate constant for the complexation of monomeric Fe(III)PPIX and H_2O_2.

$$\frac{dH_M}{dt} = -k_f[H_M]^2 + k_r[H_D] - k_1[H_M][H_2O_2] \qquad Eq.3.16$$

Since the dimerization reaction, Eq. 3.9a (p3), is assumed to be at equilibrium whilst the reaction in Eq. 3.14 (p10) is occurring, Eq. 3.16 can be simplified to Eq. 3.17, by noting that the mole fractions of $H_M(x_M)$ remains the same during the assay.

$$\frac{dH_M}{dt} = -k_{1obs}[T_p][H_2O_2] \qquad Eq.3.17$$

Thus,

$$k_{1obs} = k_1 x_M \qquad (Note: x_M[T_P] = [H_M]) \qquad Eq.3.18$$

Note, x_M is calculated by solving eq. 3.9b first and then substituting the result into eq. 3.12. The same derivation can be made if it is assumed that only the dimer reacts with peroxide.

The rate constant determined from the first reaction involving Fe(III)PPIX and H_2O_2 complexation is the observed rate constant k_{1obs} dependent on the total porphyrin concentration, while the "real" rate constant is only dependent on the activity of monomeric Fe(III)PPIX. Subsequently, the rate constant of monomeric Fe(III)PPIX and H_2O_2 complexation k_1 can be extracted from the optimized rate constant k_{1obs}. In this way the dimerization reaction was incorporated into the kinetic analysis without being added as an explicit reaction step.

All reaction models proposed for investigation in this chapter and subsequent chapters were written with incorporation of the dimerization reaction, either as a reaction step in the model, or in the form of Eq. 3.17.

For model 1, NLLS regression analysis is performed on the mechanism as is. For visual inspection of fits achieved by the constructed model 1_original, model generated data are presented with the experimental data, including the residuals of each graph generated to yield Figure 3.4.

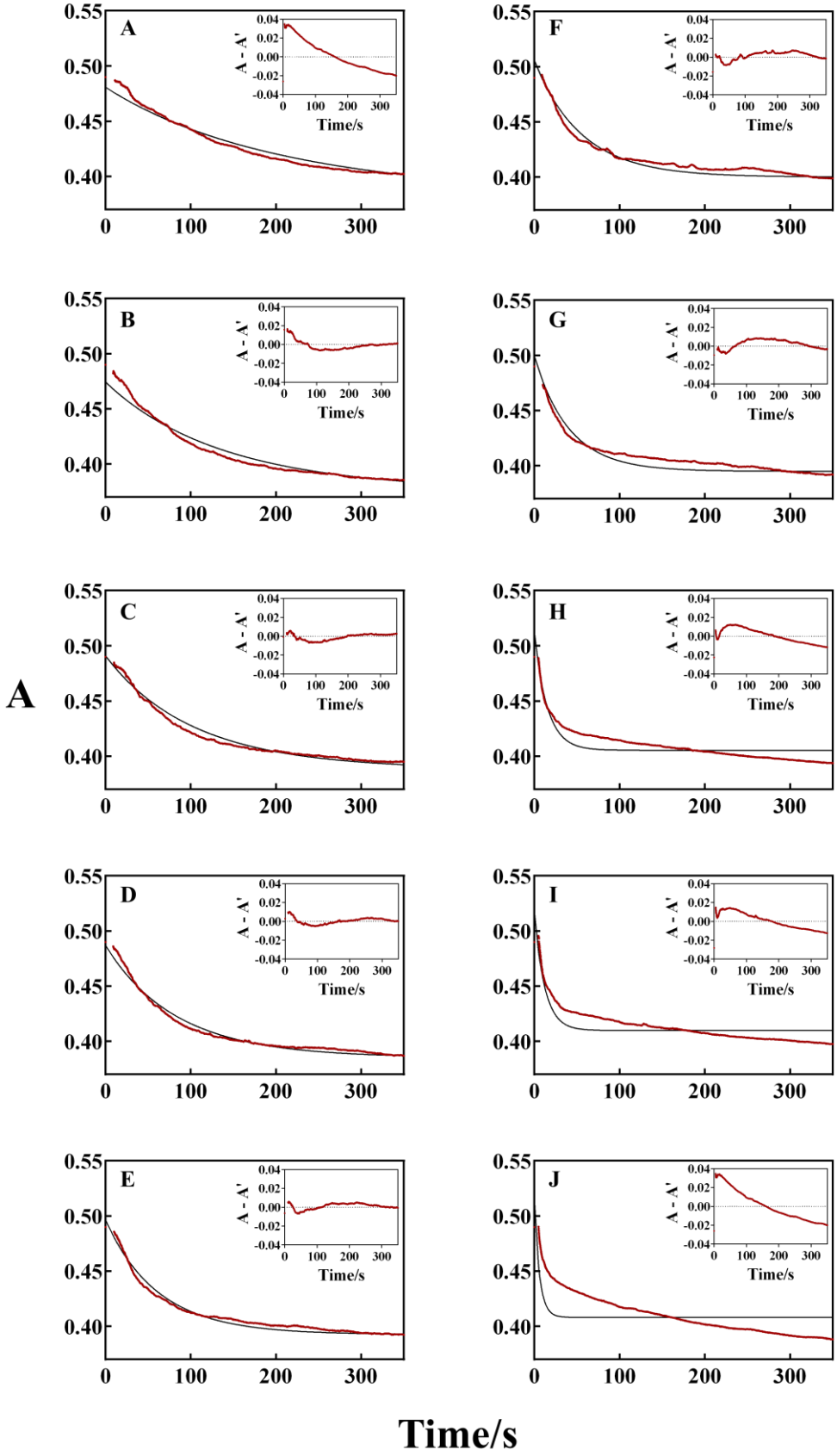

Figure 3.4: The theoretical and experimental absorbance of the reaction of H_2O_2 with Fe(III)PPIX. The sub model analysed is 1_original. Residual plots are presented as insets to allow for inspection of model deviance. From A to J, the experimental data were collected for Fe(III)PPIX at a concentration of 10 µM, and H_2O_2 at 40, 60, 80, 100, 150, 200, 300, 800, 1000 and 2000 µM.

Regarding fits achieved for 1_original, deviance between theoretical and experimental absorbance data is clearly evident (Figure 3.4). Residual plots (Figure 3.4, insets) show systematic error of the theoretical absorbance compared to experimental data, indicating that the model is insufficient to account for the reaction occurring between Fe(III)PPIX and H_2O_2. The poor fit is most likely caused by the insufficient amount of reaction steps incorporated in the reaction. Thus a second reaction step is introduced, denoting $Fe^{\bullet+}$(IV)PPIX decay as proposed by van Eldik and co-workers [70]. The original version and extension of model 1 are listed in Table 3.1

Table 3.1: Reaction steps incorporated in model extensions of model 1. H represents monomeric Fe(III)PPIX, P represents hydrogen peroxide and $H^{\bullet+}$ represents $Fe^{\bullet+}$(IV)PPIX=O

Model	**Reaction**	**Rate constant**
1_original	$H + P \rightarrow H^{\bullet+}$	k_{1obs}
1_rad	$H + P \rightarrow H^{\bullet+}$	k_{1obs}
	$H^{\bullet+} \rightarrow D$	k_2

NLLS fits obtained for the analysis of model 1_rad are presented in Figure 3.5.

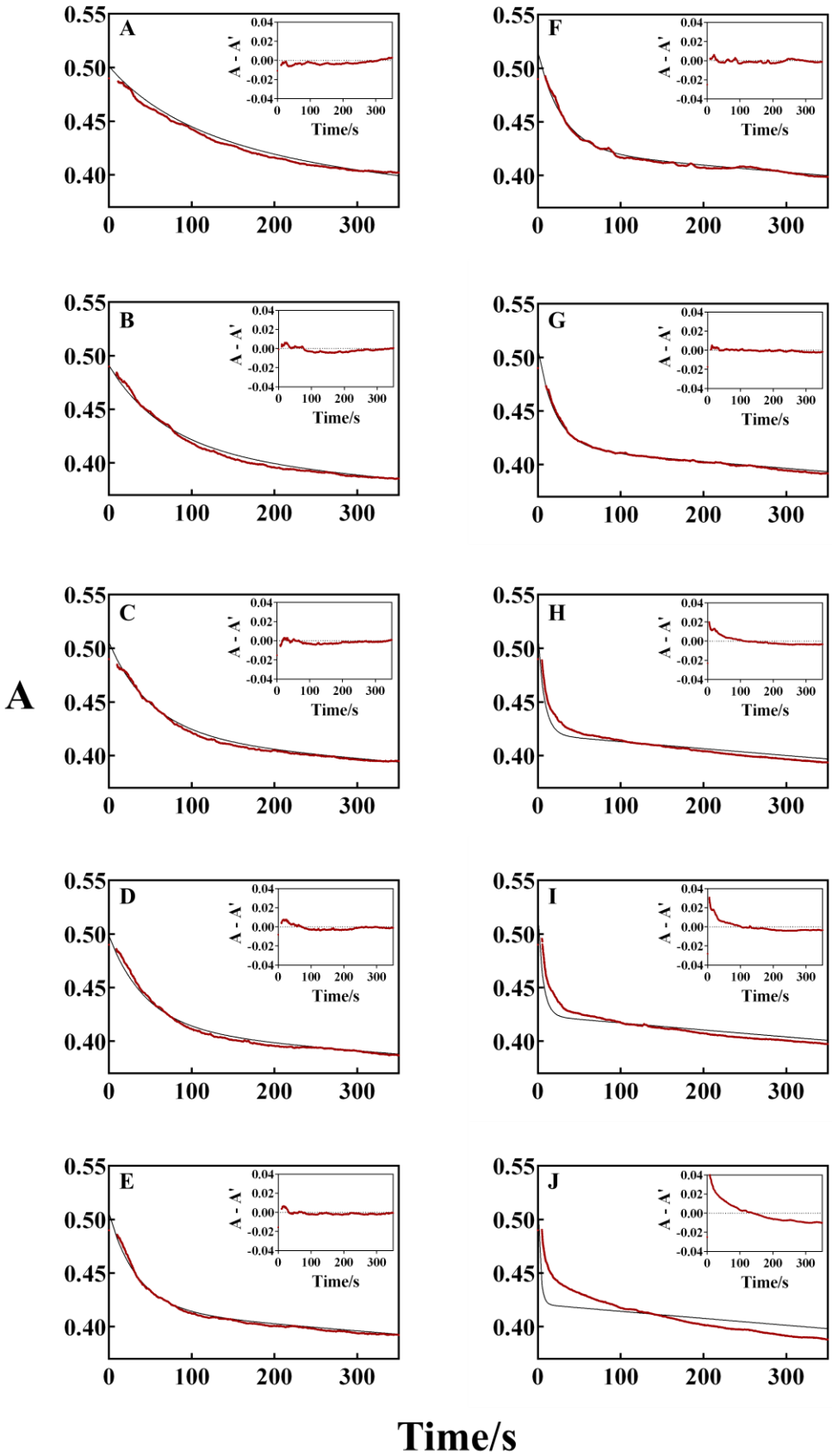

Figure 3.5: The theoretical and experimental absorbance of the reaction of H_2O_2 with Fe(III)PPIX. The sub model analysed is 1_rad. Residual plots are presented as insets to allow for inspection of model deviance. From A to J, the experimental data were collected for Fe(III)PPIX at a concentration of 10 µM, and H_2O_2 at 40, 60, 80, 100, 150, 200, 300, 800, 1000 and 2000 µM

Model 1_rad NLLS fits obtained also resulted in poor fits between theoretical and experimental absorbance data (Figure 3.5), thus the same inferences regarding this extended model are made as for 1_original regarding goodness-of-fit. An improvement is observed in goodness-of-fit with the addition of the decay of $Fe^{\bullet+}$(IV)PPIX=O to the general model 1_original. While it can be reasoned that this improvement indicates the necessity of this reaction, it must be stated that, taking the fits of the one-step reaction model 1_original into account, almost any plausible added reaction step would improve the goodness-of-fit of the model.

Table 3.2: The refined rate constants and extinction coefficients of fits achieved for model set 1.

Rate constant	**1_original**	**1_rad**	**Reaction**
k_{1obs} $(M^{-1}s^{-1})$	$(1.02 \pm 0.35) \times 10^2$	$(1.97 \pm 0.21) \times 10^2$	$H + P \rightarrow H^{\bullet+}$
k_1 $(M^{-1}s^{-1})$	1.22×10^3	2.36×10^3	$H_M + P \rightarrow H_M{}^{\bullet+}$
k_2 (s^{-1})	-	$(1.59 \pm 0.21) \times 10^{-4}$	$H^{\bullet+} \rightarrow D$
Extinction coefficient	**1_original**	**1_rad**	**Literature** [12, 16]
Fe(III)PPIX	49500 ± 1300	49500 ± 600	49000
$Fe^{\bullet+}$(IV)PPIX=O	39200 ± 3900	40500 ± 2700	39600

The multivariate global analysis results for both models (1_original and 1_rad) are summarized in Table 3.2. The calculated rate constants are meaningless as both models are not able to account for the experimental data. The relatively good agreement between calculated extinction coefficients with literature is largely due to at least the initial (time at 5 seconds) and final absorbance (time at 350 seconds) values of the theoretical data mostly corresponding well with experimental values.

3.3.2. Model set 2

Model set 2 is based on models proposed by de Almeida Ribeiro *et al*., Tatsuma and Watanabe, as well as van Eldik and co-workers, in their research on the peroxidase-like cycle of various iron (III) porphyrins [70, 74, 161]. The general mechanism encompasses an irreversible second-order reaction involving the complexation of H_2O_2 and Fe(III)PPIX, followed by the irreversible first-order conversion of Fe(III)PPIX.H_2O_2 to $Fe^{\bullet+}$(IV)PPIX (Table 3.4, 2(ir)_original). We extend model 2(ir)_original (Table 3.4) by firstly testing whether the first reaction steps may be reversible (model 2(r)_original), and secondly adding a decay step for the $Fe^{\bullet+}$(IV)PPIX=O (e.g. model 2(r)_rad), therefore resulting in a total of 4 models.

Table 3.3: Reaction steps of model extensions generated for model 2. H denotes monomolecular Fe(III)PPIX, P denotes hydrogen peroxide, H.P denotes the Fe(III)PPIX.H_2O_2 complex, $H^{\bullet+}$ denotes $Fe^{\bullet+}$(IV)PPIX=O and D denotes degradation products.

Model	Reaction	Rate constant
2(ir)_original	$H + P \rightarrow H.P$	k_{1obs}
	$H.P \rightarrow H^{\bullet+}$	k_2
2(r)_original	$H + P \rightleftharpoons H.P$	k_{1obs} k_{-1}
	$H.P \rightarrow H^{\bullet+}$	k_2
2(ir)_rad	$H + P \rightarrow H.P$	k_{1obs}
	$H.P \rightarrow H^{\bullet+}$	k_2
	$H^{\bullet+} \rightarrow D$	k_3
2(r)_rad	$H + P \rightleftharpoons H.P$	k_{1obs} k_{-1}
	$H.P \rightarrow H^{\bullet+}$	k_2
	$H^{\bullet+} \rightarrow D$	k_3

To determine the influence the reversibility of Fe(III)PPIX and hydrogen peroxide complexation has on the model fit, as well as the addition of $Fe^{\bullet+}$(IV)PPIX=O to the irreversible model, the sub models are compared by visual inspection of model fits achieved.

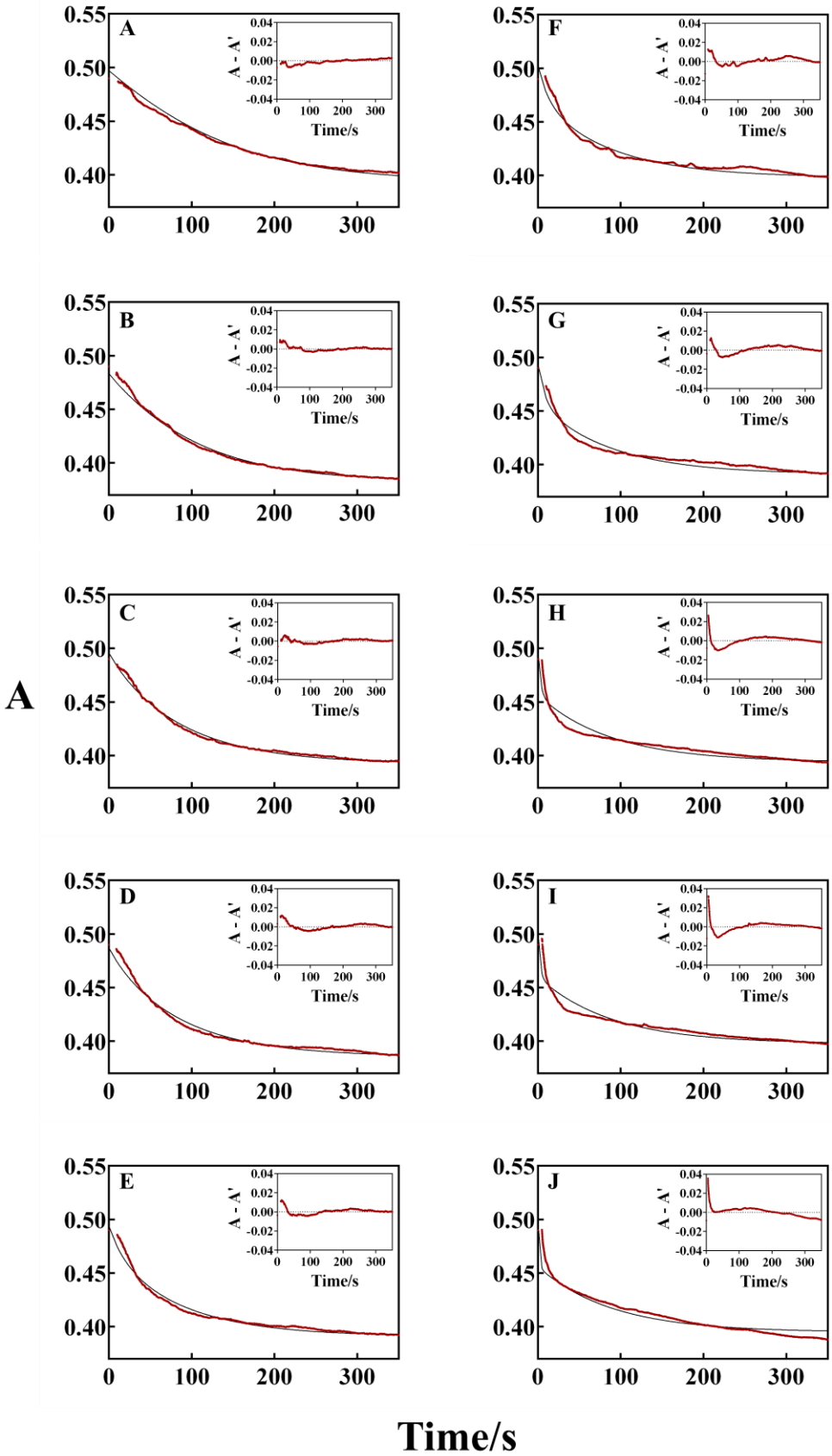

Figure 3.6: The theoretical and experimental absorbance of the reaction of H_2O_2 with Fe(III)PPIX. The sub model analysed is 2(ir)_original. Residual plots are presented as insets to allow for inspection of model deviance. From A to J, the experimental data were collected for Fe(III)PPIX at a concentration of 10 µM, and H_2O_2 at 40, 60, 80, 100, 150, 200, 300, 800, 1000 and 2000 µM.

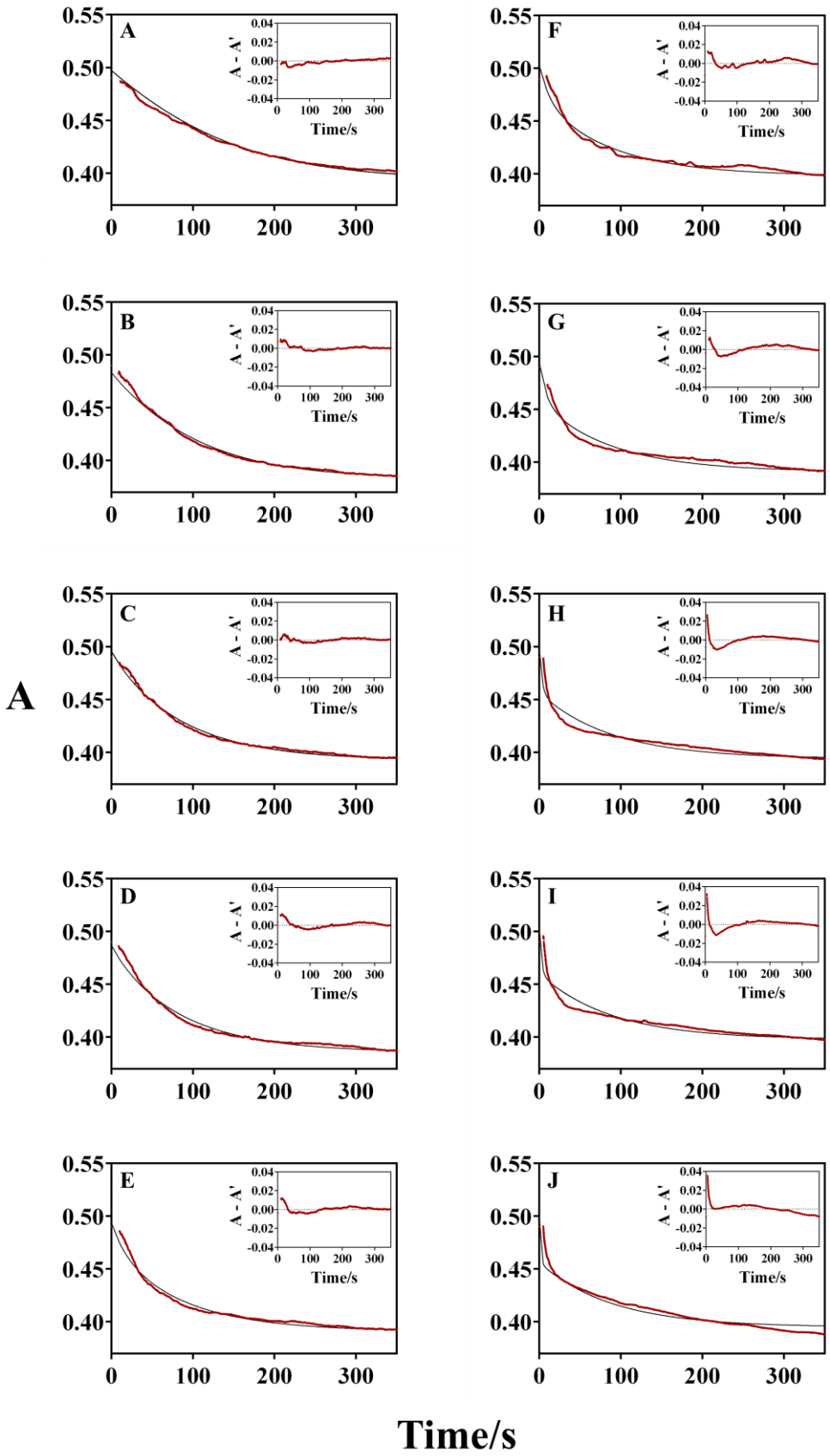

Figure 3.7: The theoretical and experimental absorbance of the reaction of H_2O_2 with Fe(III)PPIX. The sub model analysed is 2(r)_original. Residual plots are presented as insets to allow for inspection of model deviance. From A to J, the experimental data were collected for Fe(III)PPIX at a concentration of 10 µM, and H_2O_2 at 40, 60, 80, 100, 150, 200, 300, 800, 1000 and 2000 µM.

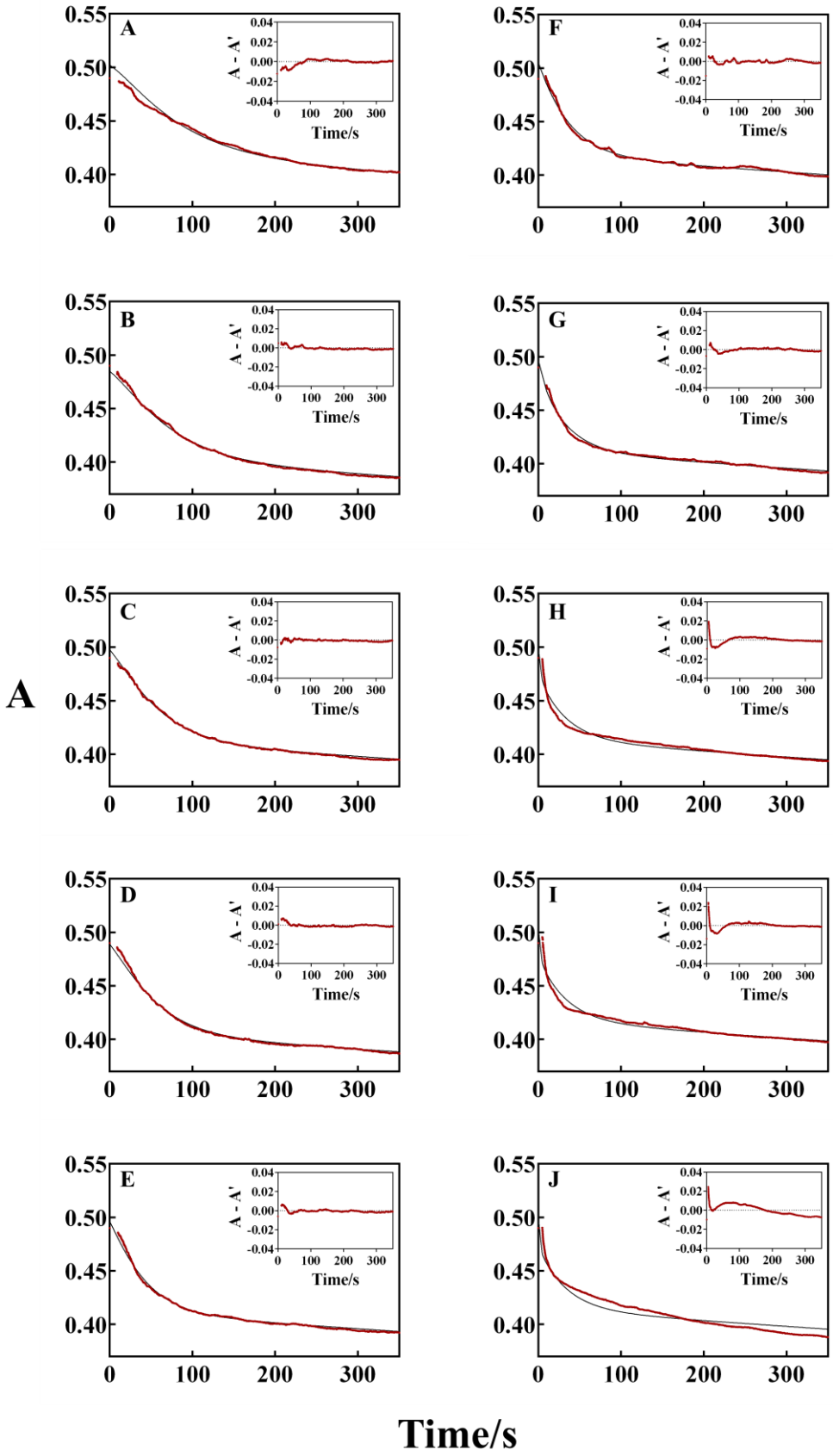

Figure 3.8: The theoretical and experimental absorbance of the reaction of H_2O_2 with Fe(III)PPIX. The sub model analysed is 2(ir)_rad. Residual plots are presented as insets to allow for inspection of model deviance. From A to J, the experimental data were collected for Fe(III)PPIX at a concentration of 10 µM, and H_2O_2 at 40, 60, 80, 100, 150, 200, 300, 800, 1000 and 2000 µM.

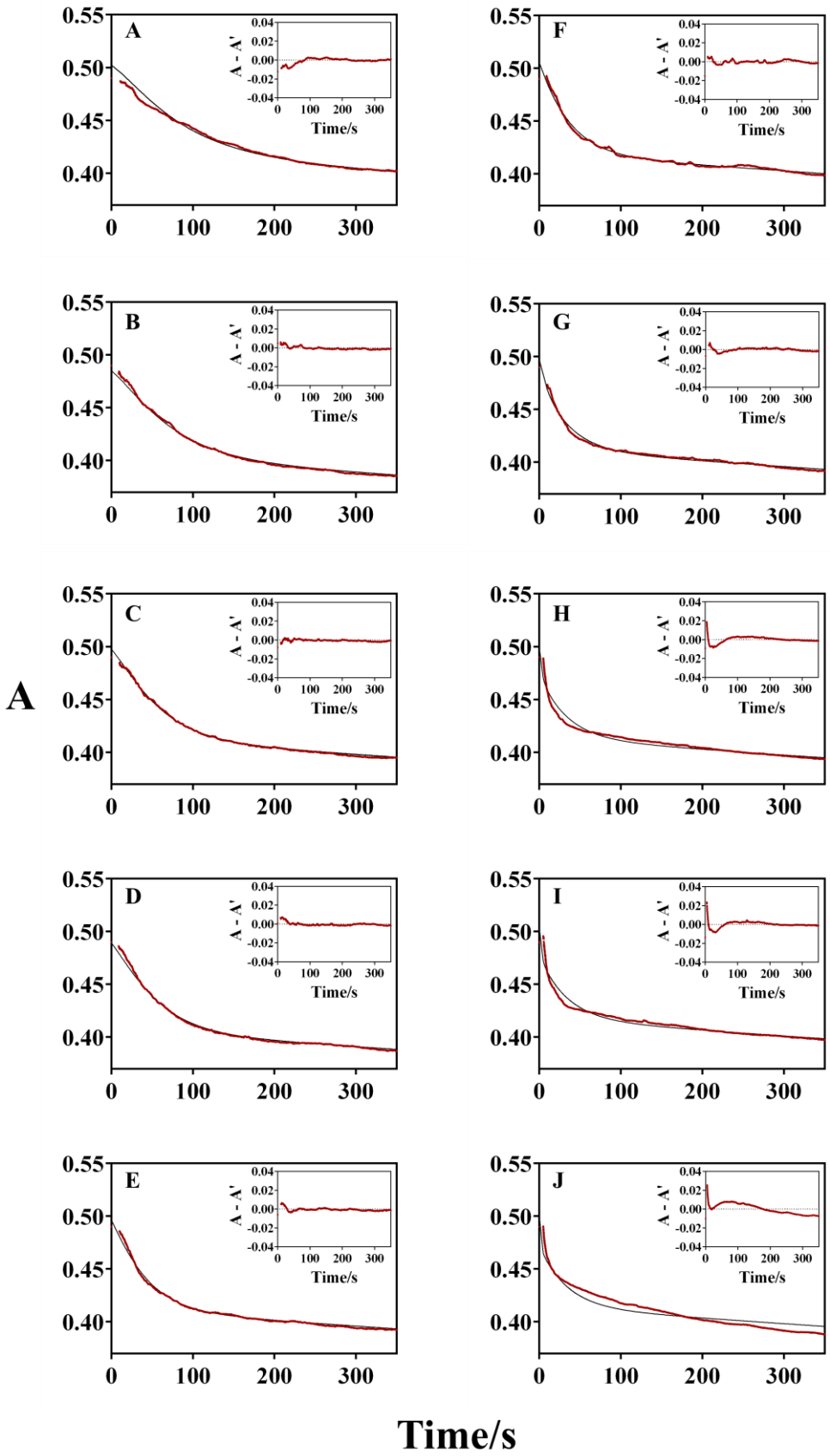

Figure 3.9: The theoretical and experimental absorbance of the reaction of H_2O_2 with Fe(III)PPIX. The sub model analysed is 2(r)_rad. Residual plots are presented as insets to allow for inspection of model deviance. From A to J, the experimental data were collected for Fe(III)PPIX at a concentration of 10 µM, and H_2O_2 at 40, 60, 80, 100, 150, 200, 300, 800, 1000 and 2000 µM.

The NLLS fits obtained for model 2(ir)_original presented in Figure 3.6 have discernible systematic deviation from the experimental results when the H_2O_2 concentration is 300 µM and higher. This indicates that the fit is worse than model 1_rad, as model 1_rad fit the data better at a H_2O_2 concentration of 300 µM and lower, with the residual plots showing less systematic deviation. Figure 3.7 represents the fitted data of model 2(r)_original. While the fits achieved for graphs A to J appear marginally better than for 2(ir)_original, systematic deviation can still be discerned from H_2O_2 at a concentration of 300 µM and up. The same inferences are made for this sub model as for 2(ir)_original, and inclusion of the reversible reaction step did not significantly improve the NLLS fits obtained. Visual inspection of the NLLS model fits for model 2(ir)_rad (Figure 3.8) yielded a significant improvement over model 2(ir)_original in terms of goodness-of-fit. Systematic deviation of model generated data is noticeable in graphs H to J as the H_2O_2 concentration is increased above 800 µM. Residual plots indicate only random error for all fits for H_2O_2 concentration below 300 µM. The residuals for this model fit is also noted to be an improvement on that of sub model 1_rad, with closer correlation to experimental data shown for graphs H to J. NLLS fits for model 2(r)_rad, presented in Figure 3.9, yielded the same trends as inferred from fits for 2(ir)_rad. Refined rate constants and extinction coefficients for model set 2 are listed in Table 3.4.

Table 3.4A: The refined rate constants and extinction coefficients of fits achieved for model set 2.

Rate Constants	**2(ir)_original**	**2(r)_original**	**Reaction**
k_{1obs} $(M^{-1}.s^{-1})$	$(3.77 \pm 0.13) \times 10^2$	$(3.78 \pm 0.37) \times 10^2$	$H + P \rightarrow H.P$
k_1 (s^{-1})	4.51×10^3	4.54×10^3	$H_M + P \rightarrow H_M.P$
k_{-1} (s^{-1})	-	$(3.20 \pm 2.47) \times 10^{-10}$	$H.P \rightarrow H + P$
k_2 (s^{-1})	$(1.12 \pm 0.13) \times 10^{-2}$	$(1.12 \pm 0.12) \times 10^{-2}$	$H.P \rightarrow H^{\bullet+}$
k_3 (s^{-1})	-	-	$H^{\bullet+} \rightarrow D$
Extinction coefficients	**2(ir)_original**	**2(r)_original**	**Literature** [70,92,167]
Fe(III)PPIX	49500 ± 750	49500 ± 1200	49000
Fe(III)PPIX.H_2O_2	45200 ± 3300	45200 ± 4900	51000
$Fe^{\bullet+}$(IV)PPIX=O	39200 ± 1300	39200 ± 700	39600

Table 3.4B: The refined rate constants and extinction coefficients of fits achieved for model set 2.

Rate Constants	**2(ir)_rad**	**2(r)_rad**	**Reaction**
k_{1obs} $(M^{-1}.s^{-1})$	$(3.81 \pm 0.35) \times 10^{2}$	$(3.88 \pm 0.22) \times 10^{2}$	$H + P \rightarrow H.P$
k_1 (s^{-1})	4.56×10^{3}	4.64×10^{3}	$H_M + P \rightarrow H_M.P$
k_{-1} (s^{-1})	-	$(5.00 \pm 3.33) \times 10^{-15}$	$H.P \rightarrow H + P$
k_2 (s^{-1})	$(3.01 \pm 0.43) \times 10^{-2}$	$(2.99 \pm 0.28) \times 10^{-2}$	$H.P \rightarrow H^{\bullet+}$
k_3 (s^{-1})	$(1.32 \pm 0.11) \times 10^{-4}$	$(1.32 \pm 0.09) \times 10^{-4}$	$H^{\bullet+} \rightarrow D$
Extinction coefficients	**2(ir)_rad**	**2(r)_rad**	**Literature** [70,92,167]
Fe(III)PPIX	49000 ± 810	48700 ± 960	49000
Fe(III)PPIX.H_2O_2	46100 ± 4300	45700 ± 3700	51000
$Fe^{\bullet+}$(IV)PPIX=O	40400 ± 670	40200 ± 1000	39600

The observed rate constant k_{1obs} (Table 3.4) does not vary much between models. Reaction of the Fe(III)PPIX.H_2O_2 complex to form $Fe^{\bullet+}$(IV)PPIX=O appears to be unchanged when testing the reversibility of the complexation of Fe(III)PPIX and hydrogen peroxide. In fact, the calculated rate constants k_{-1} obtained are so small, $3.2 \times 10^{-10}\ s^{-1}$ and $5.0 \times 10^{-15}\ s^{-1}$, that the reverse of the complexation reaction, for all practical purposes, does not occur. After the addition of the radical porphyrin decay step to form model 2(ir)_rad, the rate of formation of $Fe^{\bullet+}$(IV)PPIX=O increased. Extinction coefficients observed for Fe(III)PPIX are in good correlation with literature values [92]. The calculated extinction coefficients of the Fe(III)PPIX.H_2O_2 complex is slightly lower than that of Fe(III)PPIX, which does not agree completely with supplementary results of van Eldik and co-workers in which they use stopped-flow techniques to follow the reaction in the first few seconds, and showed that a slight increase in absorbance directly after mixing reaction components can be observed. They suggested that it is the complex between Fe(III)PPIX and peroxide with a slightly higher extinction coefficient than Fe(III)PPIX. To confirm that model 2 is better than model 1, regression statistics for goodness-of-fit of each model are listed in Table 3.5

Table 3.5: Regression statistics of fits achieved for sub models of model set 1 and 2. The SSQ, relative RMS, and Chi-Squared statistics are presented for the fitted data.

Sub Model	SSQ	%RMS	Chi-Square
1_original	1.94	1.32	4.71
1_rad	0.928	0.909	2.23
2(ir)_original	0.468	0.646	1.10
2(r)_original	0.468	0.646	1.10
2(ir)_rad	0.270	0.491	0.639
2(r)_rad	0.272	0.492	0.643

In Table 3.5 model set 2 surpasses the first model set in terms of goodness-of-fit. The SSQ is lowered from 1.94 for 1_original to 0.468 for 2_original, regardless of reversibility. The rRMS statistic drops from 1.32 % to 0.646 %, which is not as big a difference as for the SSQ, but still a significant change in model error percentage. The Chi-Square statistic is lowered from 4.71 to 1.10 from 1_original to 2_original, regardless of reversibility. Reversible and irreversible model pairs show no (original) or miniscule (rad) differences in error statistics, indicating that the reversibility of the initial complexation reaction can be discarded. For both model sets the addition of the radical porphyrin decay step almost halved the observed error, suggesting that the initial idea that the addition of the decay to 1_orginal was not a faux pas, and that this side reaction must be considered plausible for peroxidase-like cycle analysis. To ensure that the improvement from model set 1 to model set 2 is not considered over-parameterization, model comparison analysis is conducted and presented in Table 3.6.

Table 3.6: Model comparison statistics presented for sub models of model sets 1 and 2. The degrees of freedom dependent AIC and BIC are presented, along with the KLD

Sub model	AIC	BIC	KLD
1_original	-4.601×10^5	-4.601×10^5	1.26×10^{-4}
1_rad	-4.939×10^5	-4.938×10^5	5.95×10^{-5}
2(ir)_original	-5.251×10^5	-5.251×10^5	2.94×10^{-5}
2(r)_original	-5.251×10^5	-5.250×10^5	2.94×10^{-5}
2(ir)_rad	-5.502×10^5	-5.501×10^5	1.72×10^{-5}
2(r)_rad	-5.499×10^5	-5.498×10^5	1.73×10^{-5}

In Table 3.6, a decrease in the AIC and BIC is observed when moving from 1_original to 2_original models, regardless of reversibility state. For both model sets, the addition of radical porphyrin decay decreased the AIC and BIC, indicating that the addition improves the goodness-of-fit of the model, while not being an element of over-parameterization. The same inferences can be made from the KLD values, with a decrease of one order of magnitude shown for the change from 1_original to 2_original, regardless of reversibility. As such, it can be concluded that model set 2 is a better representation of the reaction between Fe(III)PPIX and H_2O_2 than model set 1. The addition of the radical decay step improves the fit, and must thus be considered for peroxidase-like cycle analysis

3.3.3. Model set 3

Model set 3 is based on the model presented by Baek and van Wart [158]. The addition of the reactive intermediate *I* was, however, considered perilous due to the possibility of over-parameterization. Baek and van Wart claimed to have isolated an intermediate species in the peroxidase-like pathway preluding the formation of $Fe^{\bullet+}$(IV)PPIX=O [158]. Thus, they offer experimental evidence supporting the addition of the intermediate *I*. The complexation of H_2O_2 and Fe(III)PPIX is considered irreversible for this set, in light of results obtained regarding the reversibility of this reaction step in model set 2 analysis. Thus, the conversion of Fe(III)PPIX.H_2O_2 to the reactive intermediate was then tested for reversibility, and with addition of radical porphyrin decay, results in four models presented in Table 3.7.

Table 3.7: Reaction steps of model extensions generated for model 3. H denotes monomolecular Fe(III)PPIX, P denotes hydrogen peroxide, H.P denotes the Fe(III)PPIX.H_2O_2 complex, $H^{\bullet+}$ denotes $Fe^{\bullet+}$(IV)PPIX=O, I denotes the active intermediate and D denotes degradation products.

Model	Reaction	Rate constant
3(ir)_original	$H + P \rightarrow H.P$	k_{1obs}
	$H.P \rightarrow I$	k_2
	$I \rightarrow H^{\bullet+}$	k_3
3(r)_original	$H + P \rightarrow H.P$	k_{1obs}
	$H.P \rightleftharpoons I$	$k_2 \quad k_{-2}$
	$I \rightarrow H^{\bullet+}$	k_3
3(ir)_rad	$H + P \rightarrow H.P$	k_{1obs}
	$H.P \rightarrow I$	k_2
	$I \rightarrow H^{\bullet+}$	k_3
	$H^{\bullet+} \rightarrow D$	k_4
3(r)_rad	$H + P \rightarrow H.P$	k_{1obs}
	$H.P \rightleftharpoons I$	$k_2 \quad k_{-2}$
	$I \rightarrow H^{\bullet+}$	k_3
	$H^{\bullet+} \rightarrow D$	k_4

The NLLS fits of each model are plotted in Figures 3.10 to 3.13 for visual inspection.

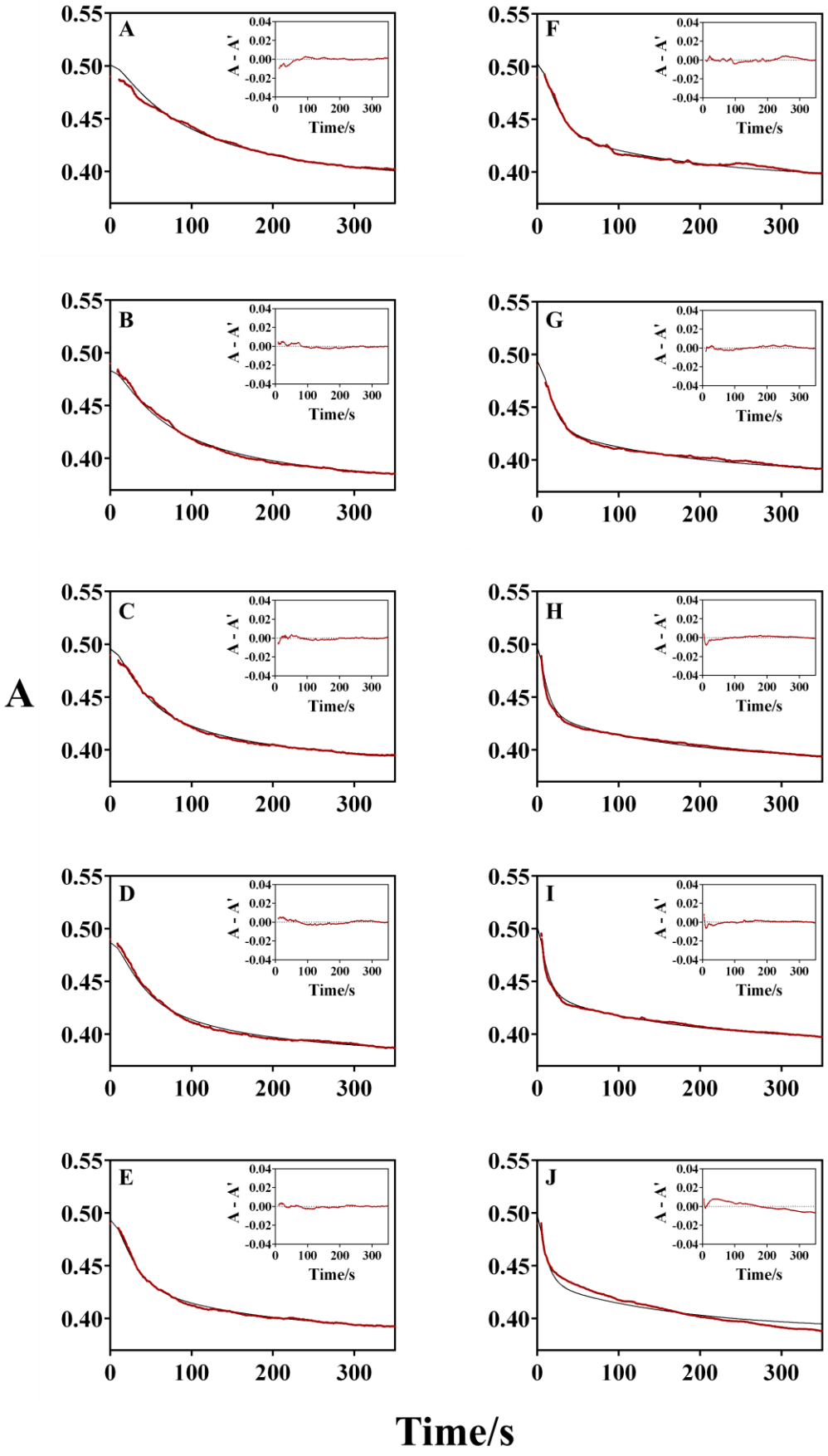

Figure 3.10: The theoretical and experimental absorbance of the reaction of H_2O_2 with Fe(III)PPIX. The sub model analysed is 3(ir)_original. Residual plots are presented as insets to allow for inspection of model deviance. From A to J, the experimental data were collected for Fe(III)PPIX at a concentration of 10 µM, and H_2O_2 at 40, 60, 80, 100, 150, 200, 300, 800, 1000 and 2000 µM.

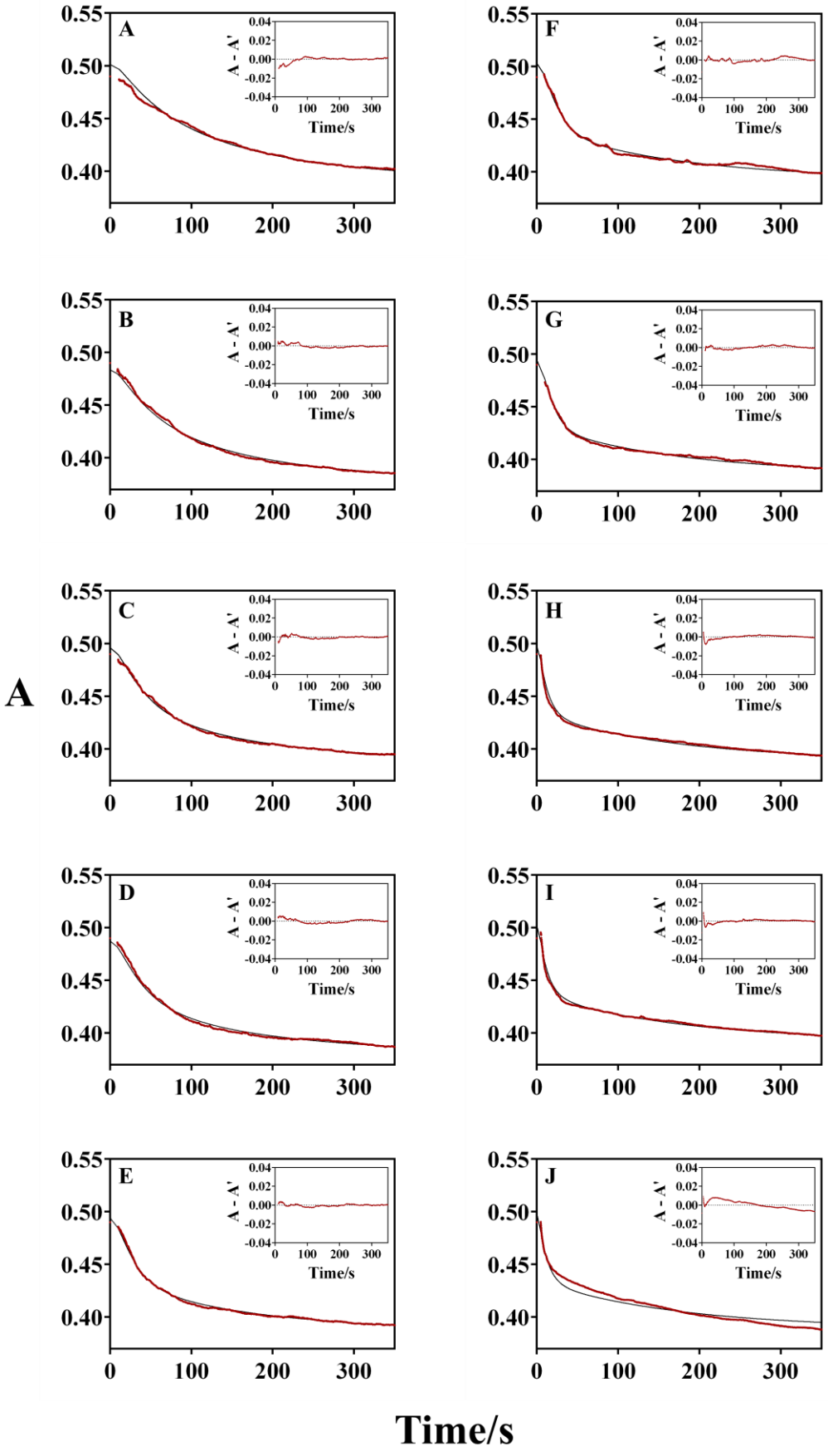

Figure 3.11: The theoretical and experimental absorbance of the reaction of H_2O_2 with Fe(III)PPIX. The sub model analysed is 3(r)_original. Residual plots are presented as insets to allow for inspection of model deviance. From A to J, the experimental data were collected for Fe(III)PPIX at a concentration of 10 µM, and H_2O_2 at 40, 60, 80, 100, 150, 200, 300, 800, 1000 and 2000 µM.

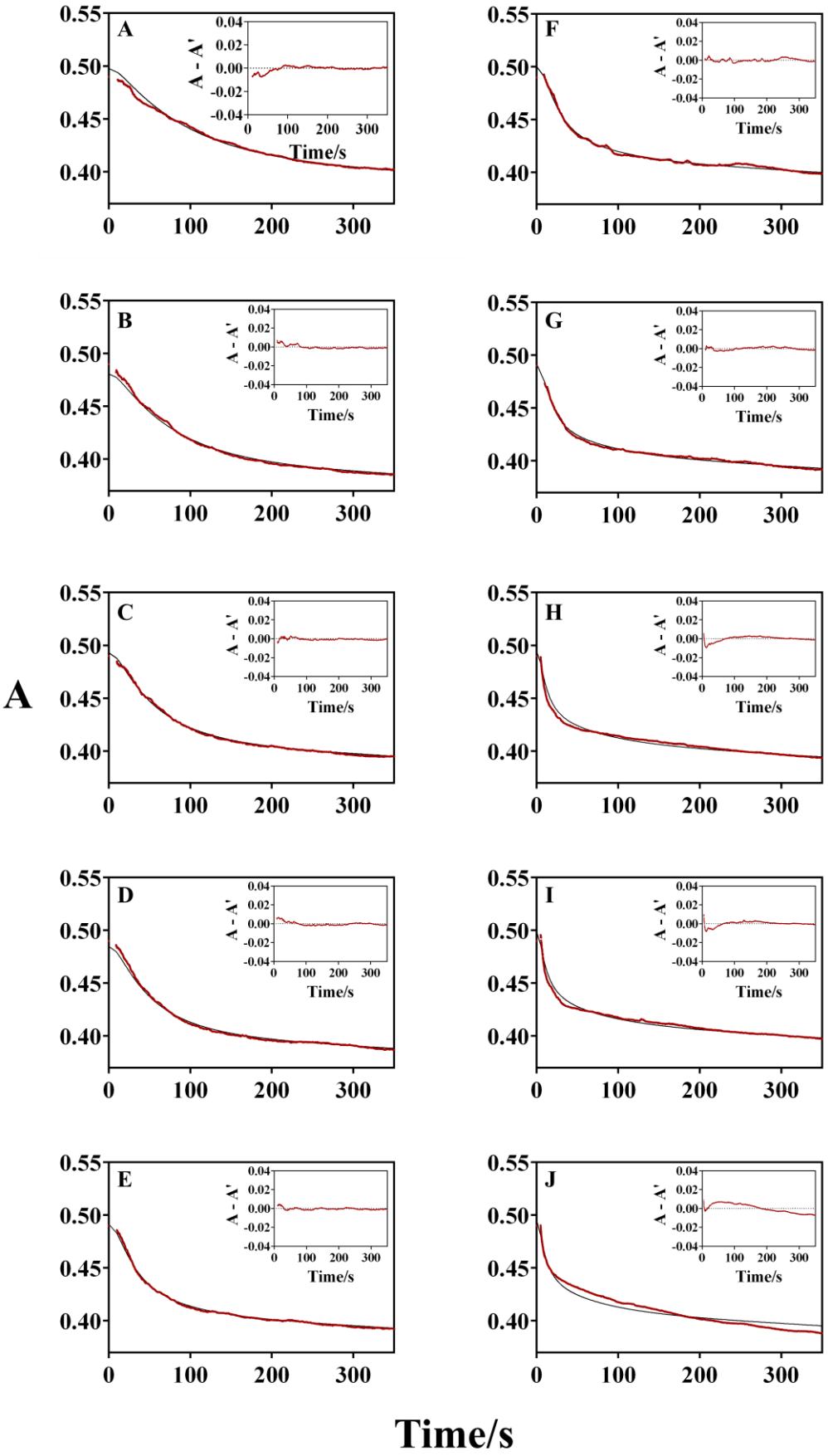

Figure 3.12: The theoretical and experimental absorbance of the reaction of H_2O_2 with Fe(III)PPIX. The sub model analysed is 3(ir)_rad. Residual plots are presented as insets to allow for inspection of model deviance. From A to J, the experimental data were collected for Fe(III)PPIX at a concentration of 10 µM, and H_2O_2 at 40, 60, 80, 100, 150, 200, 300, 800, 1000 and 2000 µM.

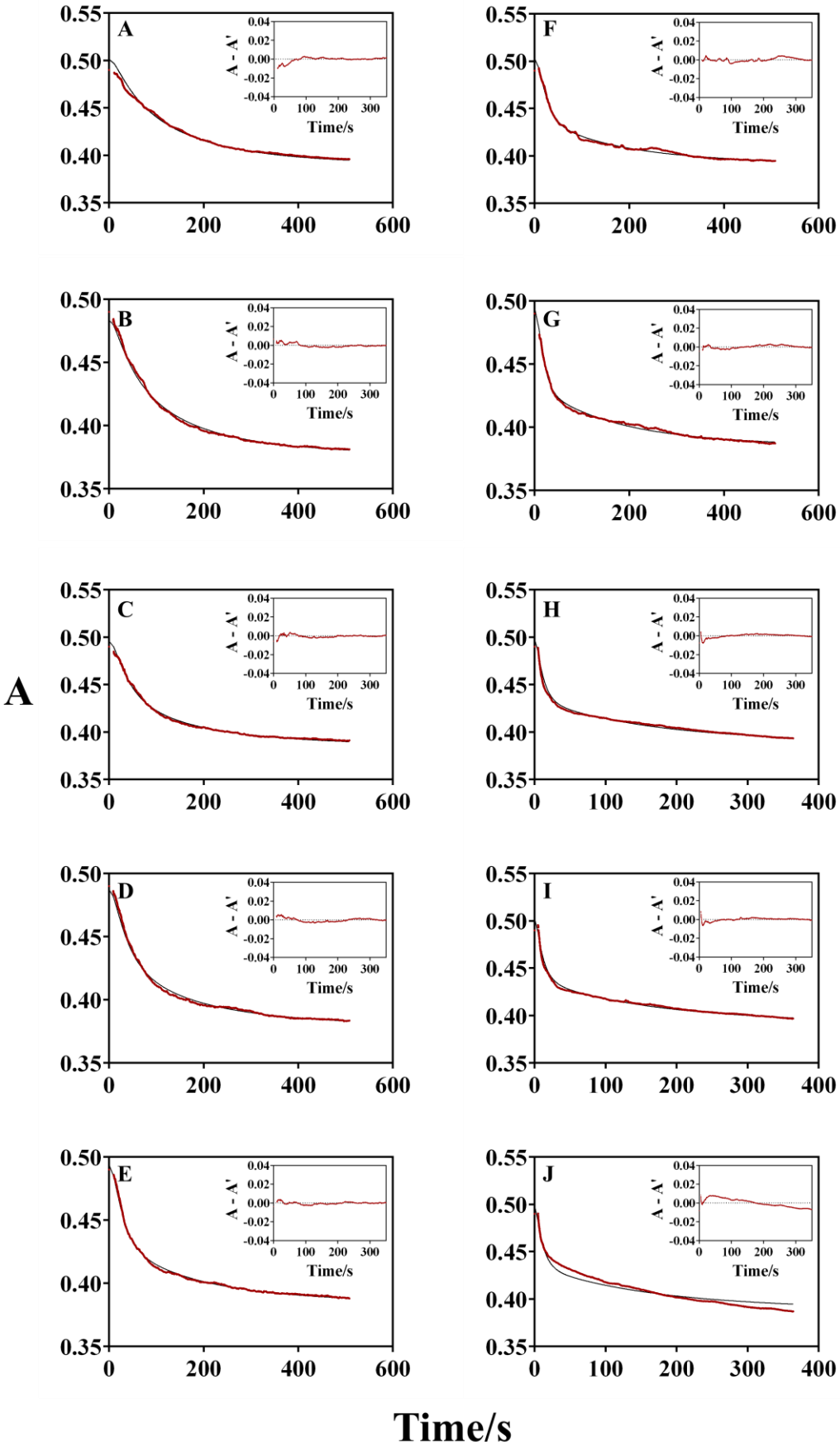

Figure 3.13: The theoretical and experimental absorbance of the reaction of H_2O_2 with Fe(III)PPIX. The sub model analysed is 3(r)_rad. Residual plots are presented as insets to allow for inspection of model deviance. From A to J, the experimental data were collected for Fe(III)PPIX at a concentration of 10 µM, and H_2O_2 at 40, 60, 80, 100, 150, 200, 300, 800, 1000 and 2000 µM.

For the model 3(ir)_original NLLS fits presented in Figure 3.10, the only case for which systematic deviation can truly be discerned from the graphs generated is for H_2O_2 at a concentration of 2000 µM in graph J. This is a substantial improvement from both 2(ir)_original and 2(r)_original fits obtained. Figure 3.11 show the model fits obtained for 3(r)_original and presents approximately the same results as obtained for 3(ir)_original, indicating that the reversibility between intermediates is not an important factor. NLLS fits of model 3(ir)_rad (Figure 3.12) show a slight increase in error observed in the residual plots, indicating that the addition of a radical porphyrin decay step decreased the goodness-of-fit for the irreversible version of the general model. The addition of the radical porphyrin decay step to 3(r)_original (Figure 3.13) did not affect the fits observed. Refined parameters for the sub models are listed in Table 3.8.

Table 3.8A: Refined rate constants and extinction coefficients for models 3(ir)_original and 3(r)_original

Rate Constant		**3(ir)_original**	**3(r)_original**	**Reaction step**
k_{1obs}	($M^{-1}s^{-1}$)	$(4.30 \pm 0.16) \times 10^2$	$(4.29 \pm 0.24) \times 10^2$	$H + P \rightarrow H.P$
k_1	(s^{-1})	5.15×10^3	5.14×10^3	$H_M + P \rightarrow H_M.P$
k_2	(s^{-1})	$(9.89 \pm 0.45) \times 10^{-2}$	$(2.80 \pm 0.25) \times 10^{-2}$	$H.P \rightarrow I$
k_{-2}	(s^{-1})	-	$(5.33 \pm 0.13) \times 10^{-2}$	$I \rightarrow H.P$
k_3	(s^{-1})	$(5.88 \pm 0.76) \times 10^{-3}$	$(1.98 \pm 0.09) \times 10^{-2}$	$I \rightarrow H^{\bullet+}$
k_4	(s^{-1})	-	-	$H^{\bullet+} \rightarrow D$
Extinction coefficient		**3(ir)_original**	**3(r)_original**	**Literature** [92,158,165]
Fe(III)PPIX		49500 ± 760	50900 ± 1500	49000
Fe(III)PPIX.H_2O_2		50000 ± 1100	51100 ± 860	51000
Intermediate *I*		42900 ± 2700	27000 ± 1600	-
$Fe^{\bullet+}$(IV)PPIX=O		38700 ± 1000	39700 ± 300	39600

Table 3.8B: Refined rate constants and extinction coefficients for models 3(ir)_rad and 3(r)_rad

Rate Constant		**3(ir)_rad**	**3(r)_rad**	**Reaction step**
k_{1obs}	($M^{-1}s^{-1}$)	$(4.52 \pm 0.43) \times 10^{2}$	$(4.31 \pm 0.31) \times 10^{2}$	$H + P \rightarrow H.P$
k_1	(s^{-1})	5.41×10^{3}	5.16×10^{3}	$H_M + P \rightarrow H_M.P$
k_2	(s^{-1})	$(1.68 \pm 0.37) \times 10^{-2}$	$(2.45 \pm 0.20) \times 10^{-2}$	$H.P \rightarrow I$
k_{-2}	(s^{-1})	-	$(5.57 \pm 0.13) \times 10^{-2}$	$I \rightarrow H.P$
k_3	(s^{-1})	$(1.03 \pm 0.09) \times 10^{-1}$	$(2.74 \pm 0.13) \times 10^{-2}$	$I \rightarrow H^{\bullet+}$
k_4	(s^{-1})	$(1.11 \pm 0.41) \times 10^{-4}$	$(1.93 \pm 0.48) \times 10^{-5}$	$H^{\bullet+} \rightarrow D$
Extinction coefficient		**3(ir)_rad**	**3(r)_rad**	**Literature** [92,158,165]
Fe(III)PPIX		49500 ± 800	49500 ± 870	49000
Fe(III)PPIX.H_2O_2		50000 ± 2100	50000 ± 1900	51000
Intermediate *I*		13300 ± 4300	20900 ± 2500	-
$Fe^{\bullet+}$(IV)PPIX=O		40800 ± 910	39000 ± 900	39600

The calculated extinction coefficient for Fe(III)PPIX (Table 3.8) for all models presented are in accordance with the literature values [92]. For this model set, the extinction coefficient of the Fe(III)PPIX.H_2O_2 complex is in agreement to that obtained by van Eldik and co-workers [70]. Extinction coefficients determined for the reactive intermediate *I* fluctuate more than expected. As Baek and van Wart isolated this species using cryogenic studies, their conditions for determining the properties of the intermediate *I* differ vastly from this study [158]. The only conclusive result regarding the extinction coefficient of this compound is that it must be lower than the extinction coefficient of Fe(III)PPIX. All calculated extinction coefficients are below that of Fe(III)PPIX, and as such is believed to be acceptable until the spectroscopic properties of the intermediate is elucidated. The forward and reverse rate constants of the reactive intermediate formation correlate well between 3(r)_original and 3(r)_rad, with the reverse rate k_{-2} of this reaction step approximated as almost double the forward reaction rate k_2. The observed initial reaction rate k_{1obs} shows consistency through testing different models. The radical porphyrin decay rate k_4 at $1.11 \times 10^{-4}\ s^{-1}$ is in close correlation with the corresponding rate for sub model 2(ir)_rad at $1.32 \times 10^{-4}\ s^{-1}$. The rate of formation of $Fe^{\bullet+}$(IV)PPIX=O, k_3, of model 3(ir)_original is two orders of magnitude lower than for model 3(ir)_rad. The inconsistency with k_3 increases the uncertainty in the model capabilities as effective descriptor of the reaction between Fe(III)PPIX and H_2O_2. To determine if model 3 proves better than model 2 in terms of goodness-of-fit, the error statistics for the two sets of models are listed in Table 3.9

Table 3.9: Regression statistics of fits achieved for sub models of model set 2 and 3. The SSQ, relative RMS, and Chi-Squared statistics are presented for the fitted data.

Sub Model	SSQ	%RMS	Chi-Square
2(ir)_original	0.468	0.646	1.10
2(r)_rad	0.270	0.491	0.639
3(ir)_original	0.174	0.195	0.412
3(r)_original	0.174	0.195	0.412
3(ir)_rad	0.199	0.209	0.474
3(r)_rad	0.175	0.196	0.412

The error statistics determined yield lower values for the conversion of model 2 to model 3. Comparison of reversible and irreversible pairs of model set 3 shows that the reversibility of the conversion of Fe(III)PPIX.H_2O_2 to the reactive intermediate does not affect the NLLS fits in any way. Addition of the radical porphyrin decay step to model 3(ir)_original increases model fit error, while a marginally small increase in the model error is seen for the same addition to 3(r)_original. This indicates that the addition of the radical decay step is not necessary and can be left out. The incorporation of another intermediate apart from the Fe(III)PPIX.H_2O_2 complex in these reaction steps regarding model set 3, yields much better fits than observed for the addition of radical porphyrin decay for model set 2. To determine if the improved fits of model set 3 are due to a better reaction model itself, or due to over-parameterization, model comparison analysis is performed, and the results are listed in Table 3.10

Table 3.10: Model comparison statistics presented for model sets 2 and 3. AIC, BIC and KLD values are shown

Sub model	AIC	BIC	KLD
2(ir)_original	-5.251×10^5	-5.251×10^5	2.94×10^{-5}
2(r)_original	-5.251×10^5	-5.251×10^5	2.94×10^{-5}
2(ir)_rad	-5.502×10^5	-5.501×10^5	1.72×10^{-5}
2(r)_rad	-5.499×10^5	-5.498×10^5	1.73×10^{-5}
3(ir)_original	-5.702×10^5	-5.702×10^5	1.11×10^{-5}
3(r)_original	-5.703×10^5	-5.702×10^5	1.11×10^{-5}
3(ir)_rad	-5.641×10^5	-5.640×10^5	1.27×10^{-5}
3(r)_rad	-5.703×10^5	-5.702×10^5	1.11×10^{-5}

Model 3(ir)_original and 3(r)_rad have the lowest AIC and BIC values (Table 3.10), and thus represent the best depiction of the reaction between Fe(III)PPIX and H_2O_2. Moreover, model 3(ir)_original is the simplest model in model set 3. It should be noted that the BIC and KLD share the same values of -5.702×10^5 and 1.11×10^{-5}, respectively, for 3(ir)_original, 3(r)_original and 3(r)_rad. Models that can only be considered adequate, but not good, depictions include 3(ir)_rad, 2(r)_rad and 2(ir)_rad. The correlation between model pairs regarding reversibility substantiate the inference that the reversibility of the complexation of Fe(III)PPIX and H_2O_2 and the formation of the other reactive intermediate *I* is negligible.

3.4. Conclusion

The reaction between Fe(III)PPIX and H_2O_2 was studied using model-based analysis. Experimental data was recorded spectrophotometrically at 385 nm for 0.1 second intervals for various concentrations of hydrogen peroxide. NLLS regression was used on the proposed reaction models to test goodness-of-fit to the experimental data.

Model 1 encompasses a single step reaction between Fe(III)PPIX and H_2O_2 to form $Fe^{\bullet+}$(IV)PPIX=O. NLLS fits achieved for this model shows that the model does not account for the experimental data. The model was then extended to include a $Fe^{\bullet+}$(IV)PPIX=O decay step to form model 1_rad. NLLS fits showed improvement in the goodness-of-fit; however, the model still offers an inadequate representation of the reaction kinetics. Model 2 denotes a two-step reaction that incorporates the reversible formation of a Fe(III)PPIX.H_2O_2 complex before the formation of $Fe^{\bullet+}$(IV)PPIX=O. The incorporation of the Fe(III)PPIX-hydrogen peroxide complex improved the goodness of fit from 1_original. Testing reversibility of the complexation reaction (2(r)_original and 2(ir)_original) did not show any difference in NLLS fits obtained. Addition of a $Fe^{\bullet+}$(IV)PPIX=O decay step significantly improved the goodness-of-fits observed, although systematic deviation could still be observed for H_2O_2 at a concentration of 800 µM and higher. Regression statistics determined show the goodness-of-fit for models 2(ir)_rad and 2(r)_rad were better than 1_rad. Comparison of regression statistics regarding models of 2(ir) and 2(r) indicated that the reversible reaction is unimportant for goodness of fit. Reverse reaction rates calculated are negligibly small, signifying that for practical purposes the reverse reaction will not occur. Model comparison analysis substantiate inferences made from regression statistics, and indicates that model 2 is a better depiction of the reaction between Fe(III)PPIX and H_2O_2 than model 1. Model 3 incorporates another active intermediate *I* before the formation of $Fe^{\bullet+}$(IV)PPIX=O. NLLS fits of model 3(ir)_original and 3(r)_original shows a significant improvement in correlation between theoretical data and experimental absorbances over models 1 and 2. Comparison of NLLS fits for model 3(ir)_original and 3(r)_original showed no difference with visual inspection. Addition of the $Fe^{\bullet+}$(IV)PPIX=O decay step reduced goodness-of-fit of model 3(ir)_original and did not perceivably affect the fit of 3(r)_original. Regression statistics of model 3 versus model 2 shows that the addition of the reactive intermediate *I* improves the goodness-of-fit. The reverse reaction of the formation of the active intermediate *I* does not influence the fit and can thus be excluded. Model comparison analysis indicates that models 3(ir)_original, 3(r)_original and 3(r)_rad yield the best fits to experimental data.

Considering that the simplest model is more than often the correct one, model 3(ir)_original is chosen as the current best representation for the reaction between Fe(III)PPIX and H_2O_2, and will subsequently be incorporated into peroxidase-like cycle studies undertaken in chapter 5. However, before the peroxidase cycle is analyzed, possible interactions of ABTS in the reaction system will be studied in the next chapter to ensure any influences that it may exert in the peroxidase-like reaction is considered.

4. Relevant reactions of ABTS

4.1. Introduction

ABTS, due to the characteristic absorbance peaks of its different species, is used in this study as a chromogen to spectrophotometrically follow the peroxidase-like activity of Fe(III)PPIX (Scheme 1.5). The reactions that ABTS can undergo in the peroxidase cycle system other than that indicated in scheme 1.5 include the complexation of ABTS to Fe(III)PPIX, the reaction between ABTS and hydrogen peroxide (H_2O_2), as well as $ABTS^{\bullet+}$ reacting with itself. These reactions need to be tested to determine the influence they may have on the kinetic absorbance measurements of the peroxidase-like reaction of Fe(III)PPIX.

Regarding the reaction between ABTS and Fe(III)PPIX, the complexation of the two compounds is proposed by de Almeida Ribeiro *et al.* as a mechanism that serves to avoid the degradation of Fe(III)PPIX by direct attack of peroxide [74]. Adams studied this complexation for haem octapeptide microperoxidase-8 via spectrophotometric titration at a pH of 7.0 and a temperature of 25 °C , and suggested a 1:1 complexation between the two compounds (eq. 4.1) with a dissociation constant of $0.89 \times 10^{-3}\ M$ [168]. This would thus affect the observed absorbance versus time signal for the peroxidase cycle as less ABTS is available to react with $Fe^{\bullet+}$(IV)PPIX=O.

$$Fe(III)PPIX + ABTS \rightleftharpoons Fe(III)PPIX.ABTS \qquad Eq.\,4.1$$

Furthermore, the use of H_2O_2 as oxidant for the generation of $Fe^{\bullet+}$(IV)PPIX can prove problematic when inspecting the reduction potential of this oxidant. H_2O_2 is a strong oxidant and may potentially oxidize ABTS. H_2O_2 has a reduction potential of 1.776 V vs standard hydrogen electrode (SHE) [169 & 170], $ABTS^{\bullet+}$/ABTS has a reduction potential of 0.69 V vs SHE, while $ABTS^{2+}$/$ABTS^{\bullet+}$ has a reduction potential of 1.10 V vs SHE [81 & 171]. As such, the electron affinity of H_2O_2 is greater than that of ABTS and $ABTS^{\bullet+}$, suggesting that H_2O_2 will oxidise ABTS and consequently generate $ABTS^{\bullet+}$ in acidic conditions. It should be noted that $ABTS^{\bullet+}$ is the chromogen species used to spectrophotometrically measure the peroxidase-like activity kinetics of Fe(III)PPIX. However, Drozd *et al.* found that H_2O_2 does not oxidise ABTS in neutral (pH 7.0) aqueous matrices [86].

Subsequently, the last side reaction that must be considered is the disproportionation reaction of $ABTS^{\bullet+}$ (Eq. 4.2). This reaction was shown to occur by Childs and Bardsley in their study on the kinetics of the Fe(III)PPIX peroxidase-like cycle using ABTS as chromogen, as well as by Branchi *et al.* in their analysis on the oxidation of benzyl alcohols [81, 94]. ABTS on its own in aqueous neutral (pH 7.0) solution is not believed to undergo any reaction except perhaps negligibly minor degradation over an extended period of time. However, if an oxidant capable of oxidizing ABTS to $ABTS^{\bullet+}$ is present in the solution, a disproportionation reaction may occur as follows (Eq. 4.2).

$$2ABTS^{\bullet+} \rightleftharpoons ABTS + ABTS^{2+} \qquad Eq.\,4.2$$

According to results presented in the study of Branchi *et al.*, the disproportionation reaction is only observed under acidic conditions [81]. Disproportionation could, however, occur in mildly basic conditions where the apparent lack of $ABTS^{2+}$ formation can be ascribed to rapid hydrolysis of $ABTS^{2+}$. This is partly substantiated by a study on the spectroscopic behaviour of ABTS conducted by Scott *et al.*, where they demonstrate that ABTS is protonated at a pH of 1 according to equation 4.3, shifting the maximum peak of absorbance from 345 to 310 nm [171].

$$ABTS + H^{+} \rightleftharpoons HABTS^{+} \qquad Eq.\,4.3$$

As discussed in chapter one, the location of the catalytically active haem within the malarial parasite is of importance [46, 47]. This is due to the reactions discussed here that may transpire at either a pH level of 4.8 or 7.5, corresponding to the pH of the digestive vacuole and plasma of the *Plasmodium* parasite, respectively. The disproportionation reaction will likely not occur under physiologically relevant conditions but may influence the peroxidase-like cycle for pH 4.8. As the generation of ROS in parasites is mediated by this reaction, it is believed relevant to study the interactions of ABTS using both pH levels [172]. In the investigation of the peroxidase activity of an iron(III) octa-anionic porphyrin complex by van Eldik and co-workers, the same chromogen and oxidant as in this case was used for experimentation [70]. Their findings suggest that the disproportionation reaction of $ABTS^{\bullet+}$ will not play a role in slightly basic to acidic solutions. However, whether a pH of 4.8 will fall into this range will be determined in this chapter.

As one of the aims was to kinetically construct a chemical reaction model of the peroxidase-like reaction of Fe(III)PPIX and prove its validity using NLLS regression analysis, the side reactions of ABTS were re-investigated under acidic and physiologically relevant conditions used in this study. The possible oxidation of ABTS with H_2O_2 and $ABTS^{\bullet+}$ disproportionation was thus studied. However, due to time constraints the complexation between ABTS and Fe(III)PPIX were not experimentally investigated, and the dissociation constant determined by Adams will be used for comparison to the parameters optimised in chapter 5, representing the association and dissociation of ABTS and Fe(III)PPIX for proposed reaction models [168].

4.2. Experimental methods

Preparation of Stock Solutions

ABTS stock solution (2.00 mM)

A 2.00 mM ABTS stock solution was prepared by dissolving 5.5 mg ABTS in distilled water to a volume of 5.00 ml in a volumetric flask.

Cerium disulphate stock solution (2.00 mM)

A 2.00 mM cerium disulphate stock solution was prepared by dissolving 8.2 mg cerium(IV)disulphate tetrahydrate in distilled water up to a volume of 10.0 ml in a volumetric flask.

Cerium nitrate stock solution (2.00 mM)

A 2.00 mM stock solution of cerium nitrate was prepared by dissolving 11.0 mg ammonium cerium(IV)nitrate in distilled water to a volume of 10.0 ml in a volumetric flask.

Nitric acid stock solution 1 (1.00 M)

A 1.00 M stock solution of nitric acid was prepared by slowly adding 11.5 ml concentrated nitric acid (55 % m/v) to 50 ml distilled water in a 100 ml volumetric flask. The solution was made up to 100 ml using distilled water.

Nitric acid stock solution 2 (5.00 M)

A 5.00 M stock solution of nitric acid was prepared by slowly adding 57.3 ml concentrated nitric acid (55 % m/v) to 20.0 ml distilled water in a 100 ml volumetric flask. The solution was made up to 100 ml using distilled water.

Permanganate stock solution (10.0 mM)

A 10.0 mM stock solution of permanganate was prepared by dissolving 15.8 mg potassium permanganate in distilled water to a volume of 10.0 ml in a volumetric flask.

Hydrochloric acid stock solution 1 (1.00 M)

A 1.00 M stock solution of hydrochloric acid was prepared by slowly adding 11.4 ml concentrated hydrochloric acid (32 % m/v) to 50.0 ml distilled water in a 100 ml volumetric flask. The solution was made up to 100 ml using distilled water.

Hydrochloric acid stock solution 2 (2.00 M)

A 2.00 M stock solution of hydrochloric acid was prepared by slowly adding 22.8 ml concentrated hydrochloric acid (32 % m/v) to 50.0 ml distilled water in a 100 ml volumetric flask. The solution was made up to 100 ml using distilled water.

Tris buffer stock solution (130 mM)

To prepare the Tris buffer solution, 1.57 g Tris-(hydroxymethyl)-aminomethane was dissolved in distilled water to a 100 ml in a volumetric flask. The pH was adjusted to 7.50 using 1.00 M hydrochloric acid solution.

For instrumentation please see chapter 3 section 3.2.1.

Reactions of ABTS

ABTS and hydrogen peroxide reaction conditions

The reaction of ABTS and H_2O_2 was studied spectrophotometrically in the wavelength range of 250 to 700 nm. pH levels of 0.5, 4.8 and 7.5 were used to determine whether any reaction observed between the two compounds is pH dependent. ABTS concentration was kept constant at 30.0 µM for all experiments conducted, whilst varying the H_2O_2 concentration. H_2O_2 can accept two electrons with a higher electron affinity than both ABTS and $ABTS^{\bullet+}$, thus implying that the addition of one unit of H_2O_2 to two units of the chromogen should theoretically lead to the production of two units of $ABTS^{\bullet+}$. As such, the concentrations of H_2O_2 used were 5.00 (limiting reagent) and 50.0 µM (in excess).

$ABTS^{\bullet+}$ disproportionation reaction conditions

Studies pertaining to $ABTS^{\bullet+}$ disproportionation were carried out at a pH level of 0.5 to confirm the generation of $ABTS^{2+}$, as well as the observation of the disproportionation reaction. This was repeated at pH levels of 4.8 and 7.5 to elucidate the kinetics of this reaction for solutions with decreased acidity. Various oxidants were employed in the study, with a new protocol presented for the generation of $ABTS^{\bullet+}$ under physiologically relevant conditions. Nitric acid (HNO_3) is presented as the first working oxidant for validating the observation of $ABTS^{2+}$ and the disproportionation reaction, after which potassium permanganate ($KMnO_4$) was employed as an effective oxidant at higher pH levels.

For the oxidation of ABTS in nitric acid, a 200 µM solution of ABTS was prepared using the stock solution for ABTS at 2.00 mM, of which 250 µL was mixed with 2250 µL of 2.00 and 0.100 M HNO_3 in turn. The final concentration of ABTS in the solution was 20.0 µM. Spectrophotometric measurements were taken in the wavelength range of 350 to 800 nm over fixed increments of time. For the oxidation of ABTS by permanganate (MnO_4^-), concentration ratios of 1:1 and 2:1 for ABTS to

permanganate were used at several pH levels. A concentration of 20.0 µM for ABTS was used for acidic studies using MnO_4^- as oxidant.

Chromogen decay

The degradation of ABTS and $ABTS^{\bullet+}$ was tested to determine if the rates of degradation would affect the spectrophotometric observation of the peroxidase-like cycle. Experiments were conducted for pH levels of 4.8 and 7.5. To study ABTS degradation by itself, an ABTS concentration of 30 µM in aqueous solution was used at both pH values. For $ABTS^{\bullet+}$ generation and subsequent decay, an ABTS concentration of 20 µM and the appropriate oxidant for the pH level in question was used.

4.3. Results and Discussion

4.3.1. ABTS and Hydrogen Peroxide

The oxidation of ABTS with H_2O_2 was tested for applicability to reaction kinetics of the peroxidase-like cycle of Fe(III)PPIX. This test is deemed necessary as it is considered probable for H_2O_2 to oxidize ABTS due to the higher redox potential of the peroxide (Eq. 4.4).

$$H_2O_2 + 2H^+ + 2e^- \rightleftharpoons 2H_2O \qquad E° = 1.776 \qquad Eq.4.4$$

However, this redox potential of hydrogen peroxide is only valid at standard state conditions, while for this study at pH 4.8 and 7.5 with proton concentrations of $1 \times 10^{-4.8}$ and $1 \times 10^{-7.5}$, respectively, they differ significantly from standard state. As such the Nernst equation (Eq. 4.5 and 4.6) can be used to calculate the redox potential of the peroxide at the different pH levels and H_2O_2 concentrations. The assumption is also made that all activity coefficients are equal to one for these redox potential calculations. This may be justified, considering the relatively low concentrations of reagents involved.

$$E_{cell} = E_{RHS} - E_{SHE} \qquad Eq.4.5$$

$$E_{RHS} = E° - \frac{RT}{nF} ln\left(\frac{1}{[H_2O_2][H^+]^2}\right) \qquad Eq.4.6$$

In the above equations, R represents the universal gas constant, T the temperature in Kelvin, n the number of electrons transferred and F is Faraday's constant. Using equation 4.5, the redox potential of hydrogen peroxide can be determined at the pH levels used (Table 4.1).

Table 4.1: New redox potentials determined for hydrogen peroxide at pH levels used in this chapter.

pH level	$[H^+]$ (M)	H_2O_2 (50 µM) E_{cell} (V)	H_2O_2 (5 µM) E_{cell} (V)
0.5	$1 \times 10^{-0.5}$	1.613	1.582
4.8	$1 \times 10^{-4.8}$	1.348	1.317
7.5	$1 \times 10^{-7.5}$	1.181	1.150

Redox potentials presented in Table 4.1 demonstrate that all redox potentials are larger than that of both ABTS/$ABTS^{\bullet+}$ and $ABTS^{\bullet+}$/$ABTS^{2+}$. As such, hydrogen peroxide should theoretically be able to oxidise ABTS to $ABTS^{\bullet+}$ at all pH levels used.

Two experiments were conducted at pH levels of 4.8 and 7.5. In the first experiment the ratio of ABTS to H_2O_2 was 6:1 and in the other 6:10. The reaction was followed via spectrophotometric measurements using a wavelength range of 250 to 700 nm to determine if there is any observable change in the absorbance of the reaction mixture.

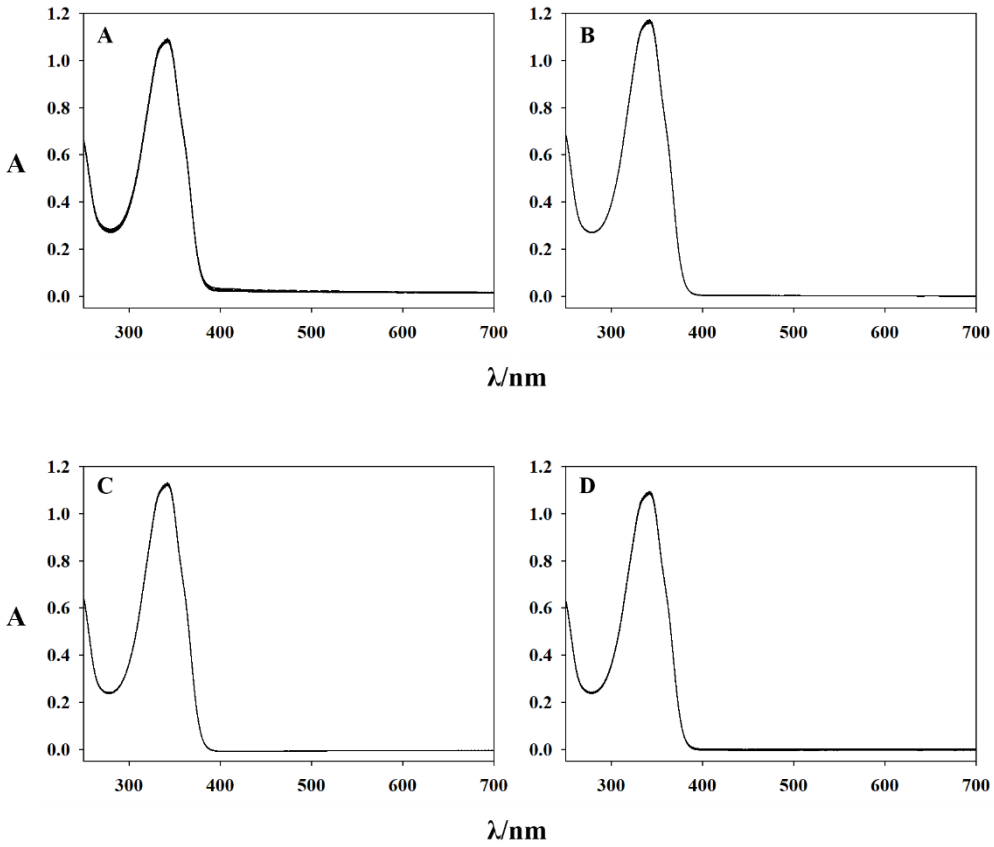

Figure 4.1: The reaction between ABTS and hydrogen peroxide. Multiple spectra measurements between 250 and 700 nm were collected as a function of time for the ABTS:hydrogen peroxide concentrations and pH values of. A) 30 µM ABTS:5 µM hydrogen peroxide at pH 7.5. B) 30 µM ABTS:50 µM hydrogen peroxide at pH 7.5. C) 30 µM ABTS:5 µM hydrogen peroxide at pH 4.8. D) 30 µM ABTS:50 µM hydrogen peroxide at pH 4.8.

As can be seen in Figure 4.1, either no reaction or an exceptionally slow one is observed between ABTS and H_2O_2 for pH levels 7.5 (A and B) and 4.8 (C and D). Since H_2O_2 has an extinction coefficient of essentially zero over the wavelength range presented it will have an insignificant contribution to the absorbance spectra. For pH 4.8, no shift in the absorbance maximum of ABTS is observed, indicating that ABTS is not protonated under moderately acidic conditions. The above experiment was repeated for a pH of 0.5 with the purpose to discern if the increased proton concentration in the system would induce H_2O_2-mediated ABTS oxidation.

At a pH of 0.5 and ABTS in moderate excess over H_2O_2 (Figure 4.2A), a small increase in absorbance around 415 nm can be observed when comparing the spectra to those obtained in Figure 4.1, indicative of a small amount of $ABTS^{\bullet+}$ formation when compared to the published UV-Vis spectrum by Branchi *et al.*, as well as the spectrum presented in Figure 1.5 [81]. With an excess of H_2O_2, $ABTS^{\bullet+}$ generation is observed over time (Figure 4.2B), indicating that the oxidation reaction does occur. However, $ABTS^{\bullet+}$ disproportionation does not appear to occur under these reaction conditions and the period of time in which recordings were made.

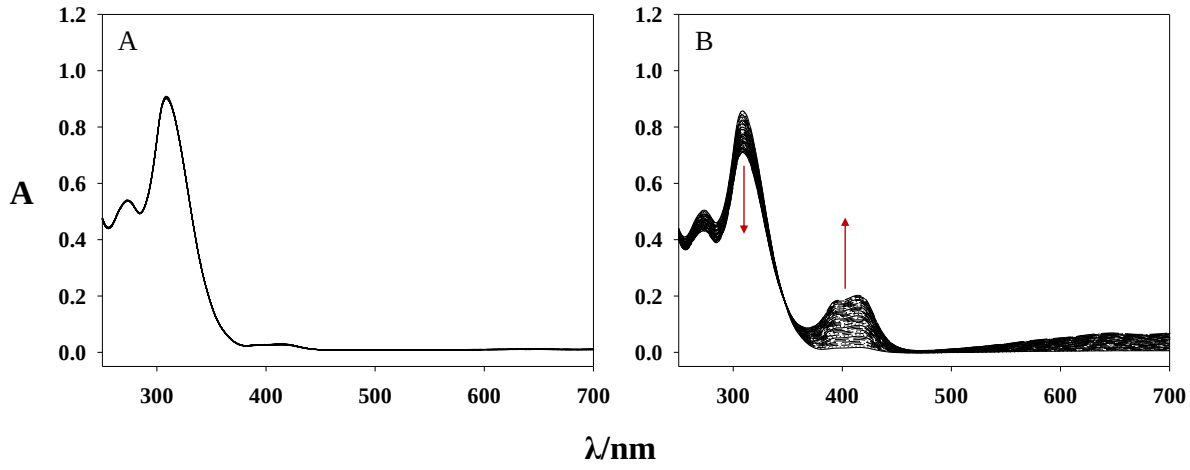

Figure 4.2: The reaction between ABTS and hydrogen peroxide. Measurements collected every 30 seconds at pH 0.5 for a wavelength range of 250 to 700 nm. A) The collection of multiple spectra of the reaction between 30 µM ABTS and 5 µM hydrogen peroxide. B) Multiple spectra collected for the full spectrum of the reaction between 30 µM ABTS and 50 µM hydrogen peroxide.

Regarding studies conducted at pH 0.5, a shift in the absorbance peak for ABTS at pH 7.5 from 345 to 310 nm at pH 0.5 is discerned (Figure 4.3). According to Scott *et al.* this shift is indicative of the conversion of ABTS to the protonated $HABTS^{+}$, where the increased acidity of the solution leads to

protonation of the chromogen and thus a shift of the absorbance maximum [171]. Consequently, Beer's Law plots were constructed for both pH's of 7.5 and 0.5.

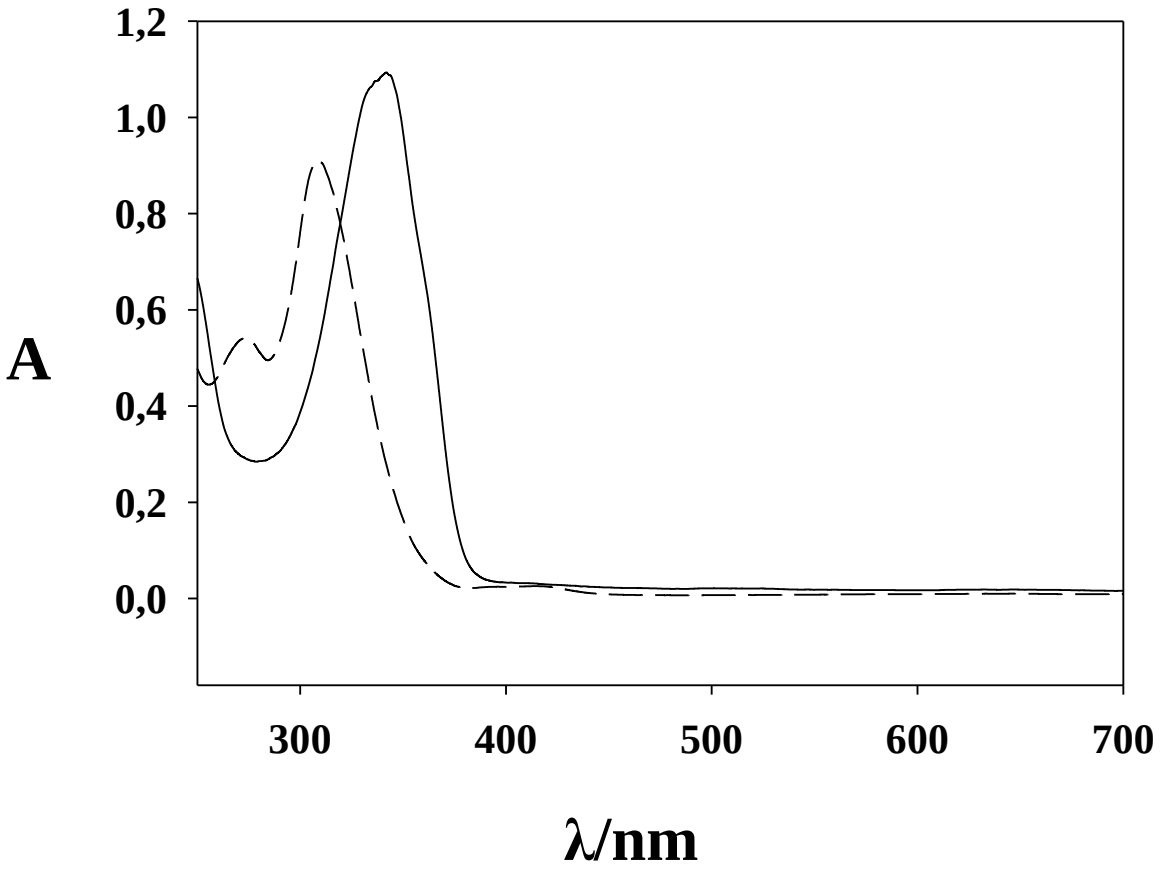

Figure 4.3: The spectrum of ABTS and HABTS$^+$. ABTS (−) at 30 µM was measured under physiologically relevant conditions, and HABTS$^+$ at 30 µM at pH 4.8 and temperature 37.5 °C. A wavelength range of 250 to 700 nm was used.

As such, H_2O_2 can be used to oxidise ABTS under highly acidic conditions when ABTS is protonated and using an excess of the oxidant. Considering the concentration ratios (ABTS > H_2O_2 >> Fe(III)PPIX) and pH levels (7.5) used for the peroxidase-like activity of Fe(III)PPIX studies, H_2O_2 will not oxidise ABTS [92]s. It can thus be deduced that the potential of H_2O_2 as an oxidant for generation of $ABTS^{\bullet+}$ is insignificant, and the reaction can be excluded when considering the mechanism of the peroxidase-like activity of Fe(III)PPIX.

4.3.2. $ABTS^{\bullet+}$ disproportionation

Investigating the disproportionation reaction of $ABTS^{\bullet+}$ is crucial for the accurate analysis of the peroxidase-like cycle of Fe(III)PPIX, as this reaction may greatly influence the observed absorbance versus time profile of $ABTS^{\bullet+}$. Consequently, tests were conducted to determine the possible effects elicited by this reaction to ensure any impact the disproportionation reaction may hold on further analysis would be incorporated into reaction models proposed. The validity of $ABTS^{\bullet+}$ disproportionation was first tested at a pH level of 0.5 to ascertain the existence of $ABTS^{2+}$, followed by analysis of the plausibility of the disproportionation reaction occurring. Thereafter, the reaction was investigated at pH values of 4.8 and 7.5 to determine if the reaction may still occur with an increase in pH. A mention should be made that a comproportionation reaction refers to the reverse of a disproportionation reaction, thus simply the generation of $ABTS^{\bullet+}$ by the interaction of ABTS and $ABTS^{2+}$ (Eq. 4.2).

Various oxidants were employed to find experimental conditions for observing the formation of $ABTS^{\bullet+}$ and possibly $ABTS^{2+}$. The first oxidant that worked for these purposes was nitric acid. Interestingly, the standard redox potential of HNO_3 is 0.958 V vs SHE [173]. This would suggest that the acid is only capable of oxidizing ABTS to form $ABTS^{\bullet+}$, and not $ABTS^{\bullet+}$ to produce $ABTS^{2+}$, as the redox potential is lower than that of $ABTS^{\bullet+}/ABTS^{2+}$ (1.10 V vs SHE redox couple). Based on this, appearance of $ABTS^{2+}$ in this system provides evidence of the disproportionation reaction taking place in the system.

Addition of concentrated nitric acid (55 % m/v) to neutral ABTS resulted in a colour change where the solution immediately turned red, and then to a dark blue-green after about five minutes. This rather imprecise benchtop experiment that resulted in a colour change indicated the presence of $ABTS^{2+}$ that changes to $ABTS^{\bullet+}$, possibly due to comproportionation (Eq. 4.2, reverse reaction), in line with observations by Branchi *et al.* and as shown in Figure 1.5 [81]. This result prompted the use of nitric acid as an oxidising agent to allow for the observation of the disproportionation of $ABTS^{\bullet+}$. Consequently, precise experimentation was conducted at a pH of 0.5 (HNO_3) and 20 and 40 µM ABTS to follow the reaction spectrophotometrically (Figure 4.4).

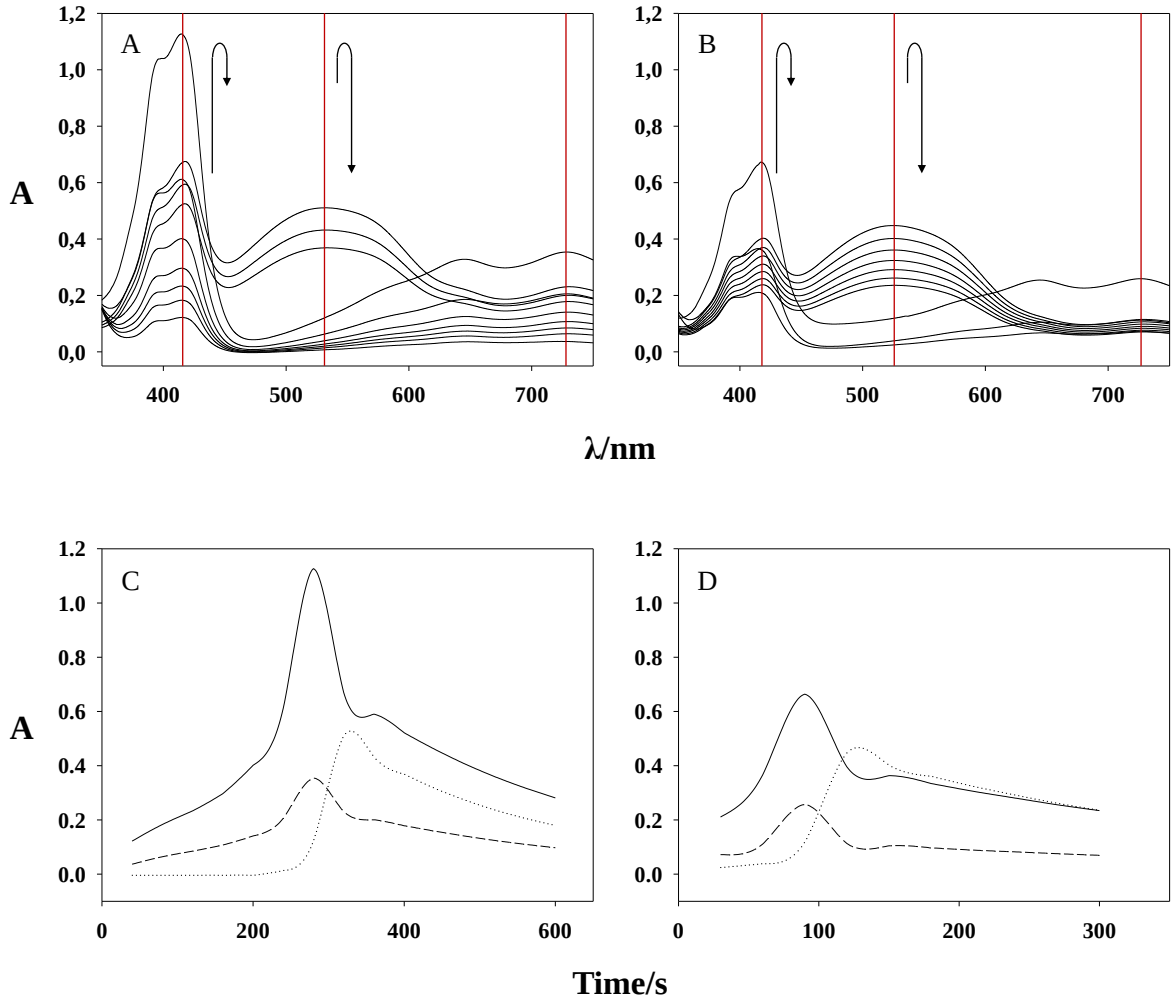

Figure 4.4: The oxidation of ABTS by nitric acid. A) The reaction of 40 µM ABTS with 0.9 M nitric acid monitored over a wavelength range of 300 to 750 nm as a function of time. B) The reaction of 20 µM ABTS with 1.8 M nitric acid over a range of wavelength as a function of time. For A and B, the increase and decrease of the absorbance signal observed is indicated by the arrows. C) The absorbance at 415 nm (–), 530 nm (···) and 730 nm (--) for reaction A represented as a function of time. D) The absorbance at 415 nm (–), 530 nm (···) and 730 nm (--) for reaction B represented as a function of time.

Regarding the absorbance spectra collected for the oxidation of ABTS with HNO_3 (Figure 4.4A and B), the first signal observed is at 415 nm, representing $ABTS^{\bullet+}$. The signal is seen to increase rapidly at 415 nm until it reaches a peak absorbance around 1.1, after which a decrease in this signal is observed, coupled with an increase in absorbance at the wavelength of 530 nm, denoting $ABTS^{2+}$. After this increase at 530 nm representing $ABTS^{2+}$ concentration, the signal decays quickly. In the first three minutes following mixing of reagents the generation of $ABTS^{\bullet+}$ alone is observed in graph C. The formation of $ABTS^{\bullet+}$ lasts only 90 seconds as seen in graph D, possibly due to the higher concentration of nitric acid and lower concentration of ABTS present in the second experiment. Both sets of conditions

adhere to the same observed trend. Following $ABTS^{\bullet+}$ generation, a sudden drop in signal for 415 and 730 nm was detected, both being absorbance maxima of $ABTS^{\bullet+}$, coupled with the signal increase at 530 nm, indicative of $ABTS^{2+}$ generation. Directly after the formation of $ABTS^{2+}$, the signal at 530 nm can be seen to decrease sharply for 20 to 30 seconds, followed by a slower signal decrease. The delay in the formation of the dicationic chromogen species suggests that its formation is not mediated by HNO_3, but rather by a different pathway. As the $ABTS^{\bullet+}$ signal observed seems to drop to almost half of its maximum absorbance following the initial increase in $ABTS^{2+}$ signal, the inference is made that $ABTS^{\bullet+}$ is required in a 1:1 ratio to other components in the mixture for the formation of $ABTS^{2+}$ to reach a maximum. With this the disproportionation reaction is implicated as the mediator for the generation of the signal at 530 nm. The ABTS versus time curves in Figure 4.4C and D are rather complex and a full kinetic study of the processes occurring is beyond the ambit of this study.

$KMnO_4$ with a redox potential of 1.47 V vs SHE was chosen as oxidant for further investigation regarding the existence of $ABTS^{2+}$ under pH's of 0.5, 4.8 and 7.5. The lowest pH is used as a control to determine the level of $ABTS^{2+}$ production and degradation. As HNO_3 only offers results pertaining highly acidic medium, a compound is needed to oxidise ABTS under physiologically relevant conditions. In acidic solutions at pH 0.5 (adjusted using HCl), using concentration ratios of 1:1 and 2:1 of ABTS to MnO_4^-, the reaction progress was followed spectrophotometrically. Regarding the reaction stoichiometry, five units of ABTS are required for every two units of MnO_4^{-1} for the complete reduction of the oxidant under the premise that ABTS will be oxidised to $ABTS^{2+}$ (Eq. 4.3).

$$2.5ABTS + 1MnO_4^- + 8H^+ \rightleftharpoons 2.5ABTS^{2+} + 1Mn^{2+} + 4H_2O \qquad Eq.\,4.3$$

Therefore, the concentration ratio of 2:1 for ABTS versus MnO_4^{-1} signifies that there are four units of ABTS for every two units of MnO_4^{-1}. As five units of ABTS can be oxidised completely by two units of MnO_4^{-1}, it is surmised that the oxidant is in excess for this ratio, and thus in greater excess for the concentration ratio of 1:1 regarding the oxidation of ABTS directly to $ABTS^{2+}$.

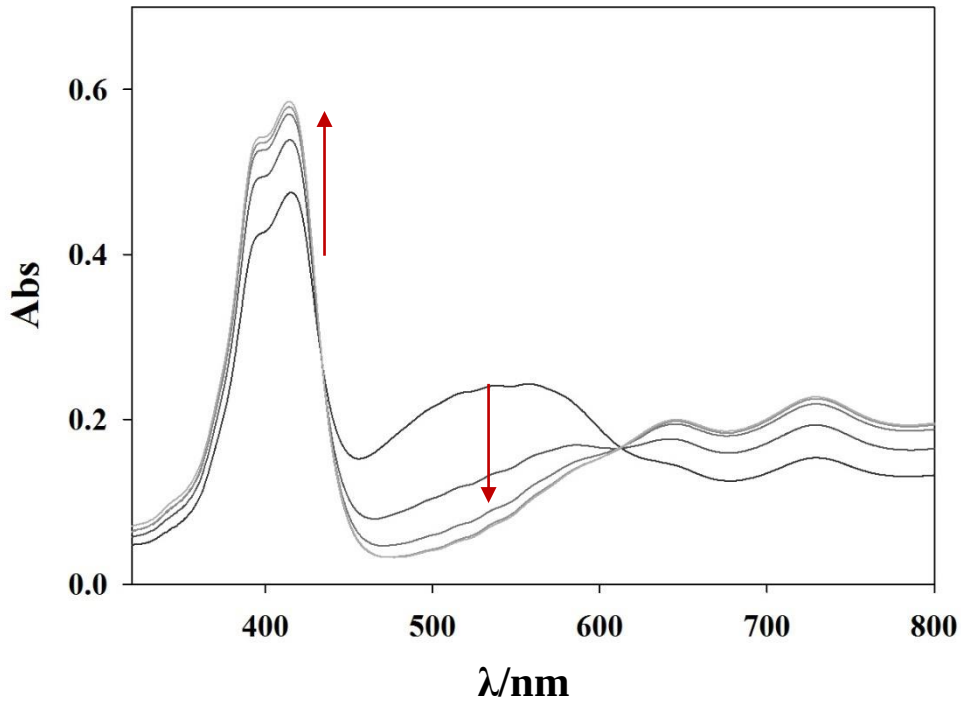

Figure 4.5: The reaction between ABTS and MnO_4^-. The spectrophotometric readings are taken at a pH of 0.5 and temperature of 37 °C for ABTS and permanganate at concentrations of 20 and 10 µM respectively. The first five minutes of the reaction are presented.

Mixing ABTS and MnO_4^- at a ratio of 2:1 and recording the UV-Vis spectrum as a function of time, yielded the results indicated in Figure 4.5. In Figure 4.5, the spectrum provides evidence of both $ABTS^{\bullet+}$ and $ABTS^{2+}$ from the start of the reaction. As the reaction progresses, a decrease in the $ABTS^{2+}$ signal is observed (530 nm), coupled with an increase in $ABTS^{\bullet+}$. The decrease in $ABTS^{2+}$ absorbance does not correspond with a 2:1 increase in the $ABTS^{\bullet+}$ absorbance as would be expected if only the comproportionation reaction was taking place (Eq. 4.2, reverse reaction). This suggests that the comproportionation reaction is not the only reaction occurring, and that $ABTS^{2+}$ degradation must be considered as well. The isosbestic point at about 610 nm is worth noting. This point signifies that at this wavelength, the molar extinction coefficients of the two compounds $ABTS^{2+}$ and $ABTS^{\bullet+}$ are the same. For an isosbestic point to occur, a one to one conversion is required (i.e. $ABTS^{2+} \rightarrow ABTS^{\bullet+}$) and does not correspond with the comproportionation reaction stoichiometry (eq. 4.2 reverse reaction). The signal for the dicationic chromogen species disappears after two minutes in the mixture, signifying that while $ABTS^{2+}$ can be present at this level of acidity, the hydrolysis of this compound seems to be significant, which agrees with the findings of Branchi *et al.* that $ABTS^{2+}$ is unstable due to the hydrolysis of the compound [81].

Repeating the experiment above between MnO_4^- and ABTS at pH levels 4.8 and 7.5 yielded the UV-Vis data plotted in Figure 4.6. Inspection of Figure 4.6 indicates that at both pH levels ABTS was oxidised to $ABTS^{\bullet+}$, since the absorbance increases at 415 and 730 nm; on the contrary, no evidence of $ABTS^{2+}$ formation was found. This could imply that $ABTS^{\bullet+}$ disproportionation is slow or that the reaction does not occur at these pH levels. These experiments also show that ABTS does not need to be protonated for oxidation to occur. A difference observed between the oxidation of ABTS at pH 4.8 and 7.5 is the rate of the oxidation, as the rate appears faster under moderately acidic conditions. This may be related to the reduction in ABTS stability as discussed in chapter 1 [90].

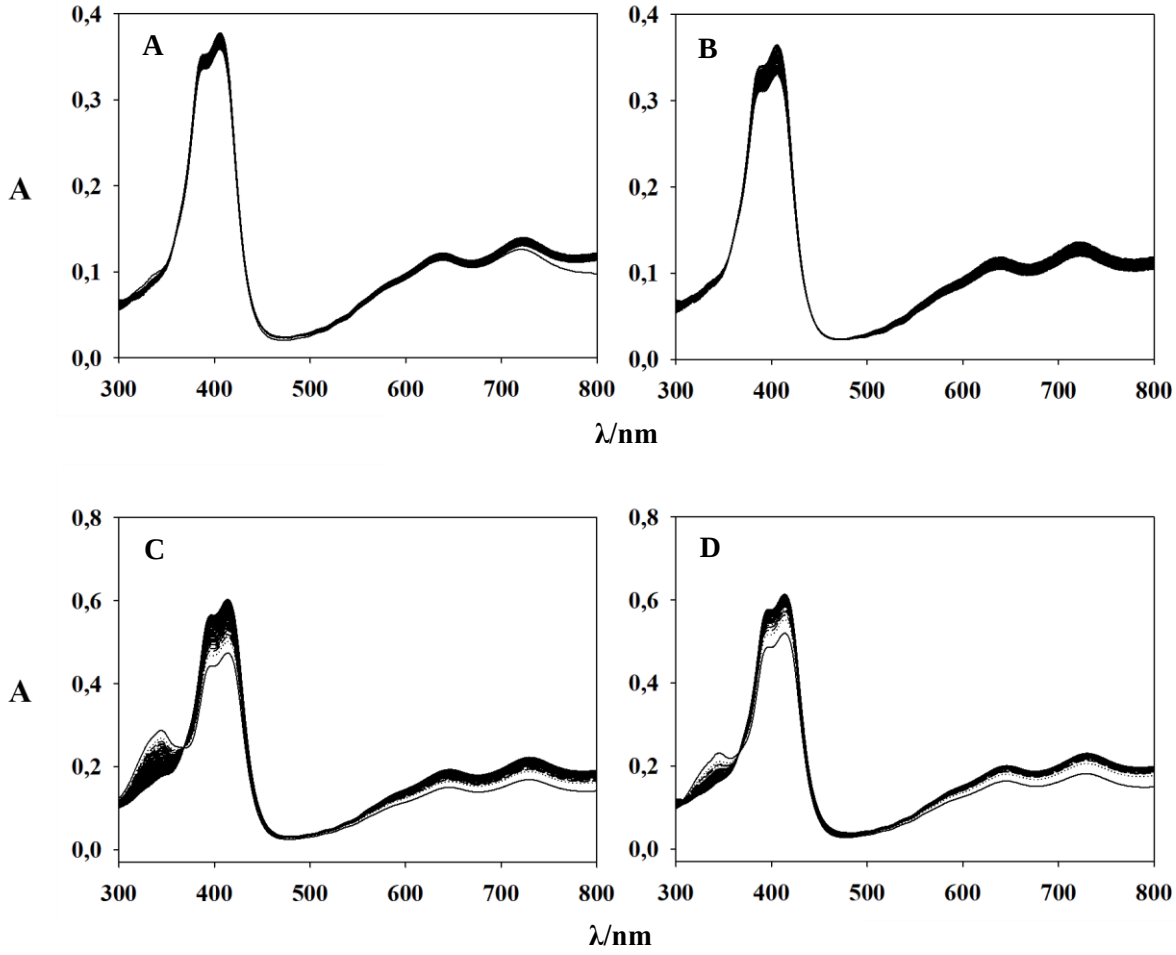

Figure 4.6: The reaction of MnO_4^- with ABTS at 37 °C followed spectrophotometrically for a wavelength range of 300 to 800 nm as a function of time. A) 20 µM ABTS was mixed with 10 µM MnO_4^- at pH 4.8. B) 20 µM ABTS was mixed with 20 µM MnO_4^- at pH 4.8. C) 20 µM ABTS was mixed with 10 µM MnO_4^- at pH 7.5. D) 20 µM ABTS was mixed with 20 µM MnO_4^- at pH 7.5

4.3.3. Chromogen Decay

The remaining side reaction that needs to be investigated before tackling the peroxidase-like cycle of Fe(III)PPIX is the possible degradation of ABTS and $ABTS^{\bullet+}$. For the degradation of the radical chromogen species, MnO_4^{-1} is used as oxidant, as no signal indicating the presence of $ABTS^{2+}$ was observed at pH levels 4.8 or 7.5. Song *et al.* presented a half reaction of permanganate reacting with ABTS under these conditions [174] (Eq. 4.7).

$$5ABTS + 1MnO_4^- + 8H^+ \rightleftharpoons 5ABTS^{\bullet+} + Mn^{2+} + 4H_2O \qquad Eq.4.7$$

Upon dissolving ABTS in solutions of pH 4.8 and 7.5 and recording the absorbance at 345 nm as a function of time, Figure 4.7A and B were obtained. As can be seen, no significant ABTS degradation takes place in the time frame of the recordings made.

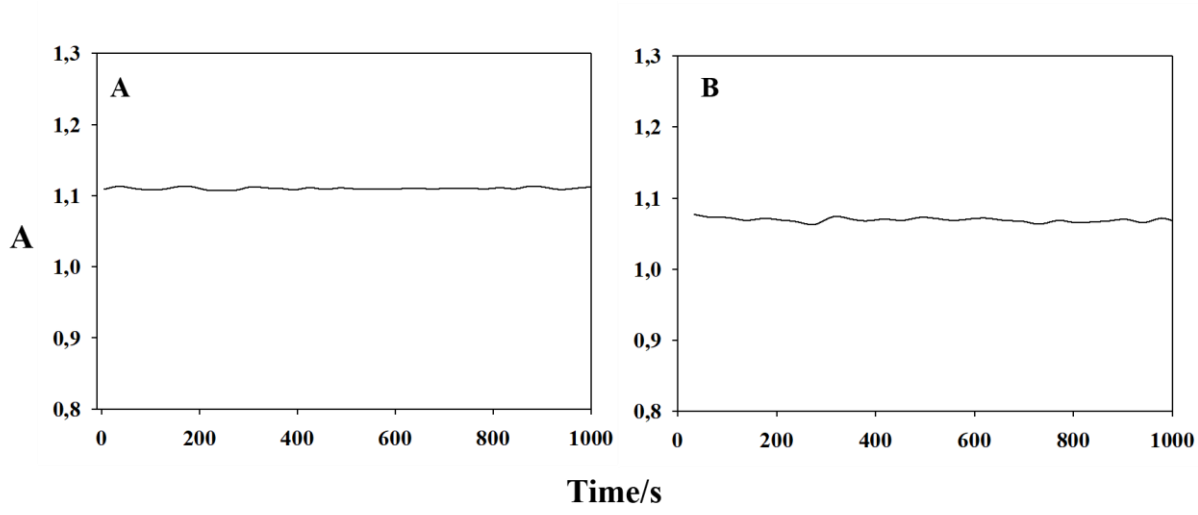

Figure 4.7: The degradation of ABTS over time. A) 30 µM ABTS is inspected spectrophotometrically at 37 °C and pH 4.8 over a period of time to determine the decay of the signal collected at 345 nm. B) 30 µM ABTS is employed in a physiologically relevant system to observe the decay of the chromogen over time at 345 nm.

For Figure 4.8, inspection of the absorbance versus time data shows marginal decay of the signal at 730 nm for conditions pertaining pH 4.8, while a slight increase in signal is observed for pH 7.5. This difference in observed signal may be linked to several reasons and requires a more detailed study to unravel. In the context of investigating the peroxidase-like activity of Fe(III)PPIX, a slow decay step might be considered for the proposed model regarding Fe(III)PPIX peroxidase-like activity.

$$ABTS^{\bullet+} \rightarrow Degradation\ Product \qquad Eq.4.6$$

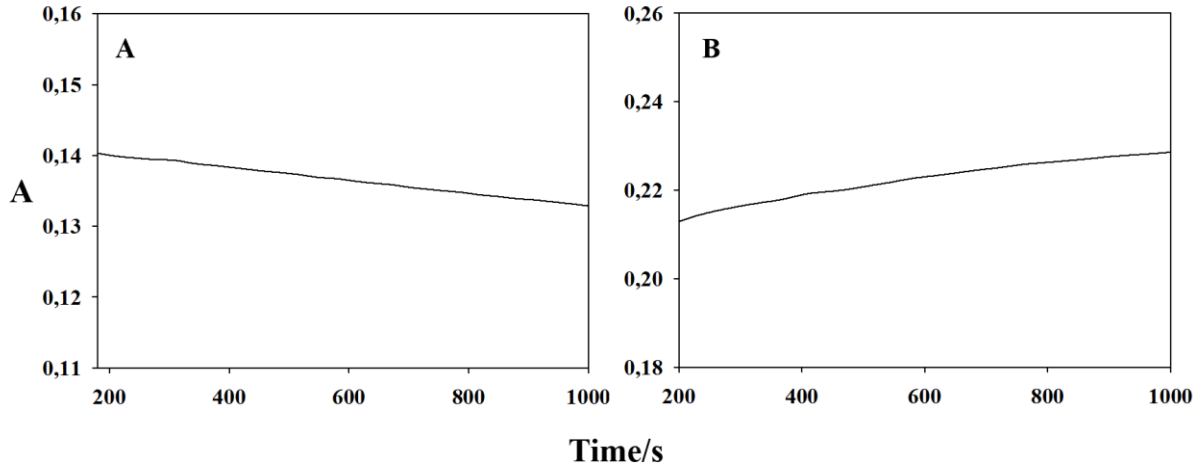

Figure 4.8: The degradation of $ABTS^{\bullet+}$ over time. A) 20 µM ABTS is oxidised using MnO_4^{-1} to form $ABTS^{\bullet+}$, which is inspected spectrophotometrically at 37 °C and pH 4.8 as a function of time to determine the decay of the signal collected at 730 nm. B) 20 µM ABTS is oxidised using MnO_4^{-1} to form $ABTS^{\bullet+}$ in a physiologically relevant system to observe the decay of the signal over time at 730 nm.

4.4. Conclusion

Potential reactions of ABTS, other than that presented in Figure 1.5, have been investigated to determine the effect of these reactions on kinetic absorbance measurements of the peroxidase-like reaction of Fe(III)PPIX. The first reaction considered was the oxidation of ABTS with H_2O_2, as the redox potential of the peroxide exceeds that of both $ABTS^{\bullet+}$/ABTS and $ABTS^{2+}$/$ABTS^{\bullet+}$ for all pH levels used (Table 4.1) and is thus believed capable of oxidizing ABTS. Studies at pH levels of 4.8 and 7.5 showed that no oxidation reaction occurred. It was also found (Figure 4.2) that ABTS is protonated under highly acidic conditions, shifting the maximum absorbance from 345 nm to 310 nm, with 310 nm indicative of $HABTS^{+}$ presence (Figure 4.3). Oxidation of ABTS with H_2O_2 was only observed at a pH of 0.5 with the peroxide concentration in excess to that of ABTS. HNO_3 oxidized ABTS to $ABTS^{\bullet+}$, followed by the formation of $ABTS^{2+}$. As the acid has a lower redox potential (0.89 V vs SHE) than $ABTS^{2+}$/$ABTS^{\bullet+}$, the formation of the dication species was attributed to the disproportionation of $ABTS^{\bullet+}$ (Eq. 4.2). The use of permanganate at pH 0.5 to oxidise ABTS showed the formation of both $ABTS^{2+}$ and $ABTS^{\bullet+}$, with an isosbestic point observed (Figure 4.5) at around 610 nm for the conversion of $ABTS^{2+}$ to $ABTS^{\bullet+}$, indicating that the stoichiometry of the reaction is 1:1, thus not corresponding to a comproportionation reaction (Eq. 4.2 reverse reaction) and consequently requiring more in-depth study in future work on ABTS as chromogen. For pH levels of 4.8 and 7.5, no absorbance signal for $ABTS^{2+}$ was observed, leading to the inference that the disproportionation reaction either occurs slowly enough to be negligible, or doesn't occur at all. While ABTS was found not to degrade significantly in aqueous solution for pH levels of 4.8 and 7.5, $ABTS^{\bullet+}$ did show slow degradation for a pH of 4.8.

However, at a pH of 7.5, a slight increase in absorbance is observed, requiring analysis of the reaction outside the ambit of this study.

Therefore, the oxidation of ABTS with H_2O_2 will not occur for conditions used to study the peroxidase-like activity of Fe(III)PPIX, nor will disproportionation of $ABTS^{\bullet+}$ affect the kinetics of the peroxidase-like reaction. Plausible degradation of ABTS can also be omitted from reactions considered for the peroxidase-like model, while decay of $ABTS^{\bullet+}$ is considered a viable side reaction. The complexation of Fe(III)PPIX and ABTS to participate in the peroxidase-like cycle via a secondary pathway will also be included. For the complexation of Fe(III)PPIX and ABTS, dissociation constant presented by Adams *et al.* will be used for comparison to refined parameters yielded by NLLS regression of models proposed [168].

5. The peroxidase cycle of haem

5.1. Introduction

Mechanistic investigations into the reaction of iron porphyrins are considered of high importance to uncover the oxidative potential of this moiety that is commonly found to react in a similar manner to both catalases and peroxidases. The toxicity of this organometallic compound is of interest in research on malaria parasites, as one plausible mechanism of certain antimalarial compounds seem to enhance or affect this toxicity in a way that speeds the apoptosis of the malarial cell in which the activity of haem transpires. As such, the end goal of this study is the proposal of a chemical mechanism governing the reaction kinetics of the peroxidase activity of haem with efficiency.

In the elucidation of chemical mechanisms of enzymes or organometallic compounds with enzyme-like activity, all possible elements partaking in and affecting the reaction must be identified and characterized with the purpose of constructing a mechanistic reaction pathway accurately depicting the kinetic data collected for such a reaction. As such, the interaction between Fe(III)PPIX and H_2O_2, as well as the possible effects of ABTS reactions on the peroxidase-like cycle have been studied to ease the analysis of the peroxidase-like cycle of Fe(III)PPIX. Models proposed for this chapter would incorporate rate constants optimised in the previous chapters. The model that proves to yield the best representation of the kinetic data will yield insight into the specific mechanisms of action of various peroxidase haemoproteins. More importantly, the model most accurately describing the reaction would offer a system for kinetic comparison to the same system under unexplored conditions.

Zipplies *et al.* determined the influence of the activity of hydrogen ions on the peroxidase-mediated decomposition of hydrogen peroxide in 1986 [73]. They studied the interaction between an iron porphyrin and hydrogen peroxide at a pH of 7.0 and temperature of 30 °C. The resulting reaction mechanism proposed follows the same general reaction steps as seen for model set 2 of chapter 3 regarding Fe(III)PPIX and hydrogen peroxide interaction, with a reversible complexation of Fe(III)PPIX and hydrogen peroxide (Eq. 5.1). Following $Fe^{\bullet+}$(IV)PPIX production (Eq. 5.2), the radical iron porphyrin reacts with ABTS to generate Fe(IV)PPIX=O and $ABTS^{\bullet+}$ (Eq. 5.3). Fe(III)PPIX=O can react with another molecule of ABTS to regenerate Fe(III)PPIX and produce $ABTS^{\bullet+}$ (Eq. 5.4).

$$Fe(III)PPIX + H_2O_2 \rightleftharpoons Fe(III)PPIX.H_2O_2 \qquad Eq.5.1$$

$$Fe(III)PPIX.H_2O_2 \rightarrow Fe^{\bullet+}(IV)PPIX \qquad Eq.5.2$$

$$Fe^{\bullet+}(IV)PPIX + ABTS \rightarrow Fe(IV)PPIX{=}O + ABTS^{\bullet+} \qquad Eq.5.3$$

$$Fe(IV)PPIX{=}O + ABTS \rightarrow Fe(III)PPIX + ABTS^{\bullet+} \qquad Eq.5.4$$

However, following results from chapter three, we know the reaction steps presented in Eq 5.1 and 5.2 must actually be presented as in Eq. 5.5 to 5.7.

$$Fe(III)PPIX + H_2O_2 \rightarrow Fe(III)PPIX.H_2O_2 \quad Eq.5.5$$

$$Fe(III)PPIX.H_2O_2 \rightarrow I \quad Eq.5.6$$

$$I \rightarrow Fe^{\bullet+}(IV)PPIX \quad Eq.5.7$$

Jones reviewed the effect of water on the activity of Fe(III)PPIX peroxidase and catalase enzymes in 2001 to determine the effect of ligand modification on the peroxidase activity of select iron porphyrins [159]. The mechanism proposed in his discussion is akin to that of Zipplies *et al.*, although the reaction mechanism they presented was simply in terms of horseradish peroxidase (HRP) activity.

van Eldik and co-workers proposed a mechanism for the peroxidase-like cycle based on the results of their study on the reaction of an iron porphyrin with hydrogen peroxide, using ABTS as chromogen [70]. Using a variety of pH values and temperature at 4 °C, they used stopped-flow spectroscopy to study the peroxidase-like activity of iron porphyrin. The mechanism proposed in the course of their study regarding physiologically relevant pH follows the same general trend as observed for mechanisms of Zipplies *et al.* and Jones [1, 4]. They detected degradation of radical iron porphyrin (Eq. 5.8) and showed that at high enough concentrations of hydrogen peroxide, catalase activity of the iron porphyrin could be stimulated (Eq. 5.9). Therefore, $Fe^{\bullet+}$(IV)PPIX reacted with hydrogen peroxide to regenerate haematin and produce oxygen and water.

$$Fe^{\bullet+}(IV)PPIX \rightarrow Deg \quad Eq.5.8$$

$$Fe^{\bullet+}(IV)PPIX + H_2O_2 + H_2O \rightarrow Fe(III)PPIX.H_2O + H_2O + O_2 \quad Eq.5.9$$

Adams studied the plausible complexation between Fe(III)PPIX and ABTS to determine the equilibrium constant for the interaction [168]. In this study the reaction between iron porphyrin and hydrogen peroxide was followed at a temperature of 25 °C and pH 7.0, to elicit a reaction mechanism describing the peroxidase-like reaction. Based on results obtained, a second "cycle" involving the complexation of Fe(III)PPIX and ABTS (Eq. 5.10) was proposed to function in parallel to the peroxidase-like cycle presented by Zipplies *et al.* and Jones [1, 4]. This parallel cycle incorporates the coordination of hydrogen peroxide to this Fe(III)PPIX.ABTS complex (Eq. 5.11), followed by the formation of $Fe^{\bullet+}$(IV)PPIX.ABTS (Eq. 5.12). The radical iron porphyrin then reacts with the ABTS coordinated to it in order to generate Fe(IV)PPIX=O and $ABTS^{\bullet+}$ (Eq. 5.13).

$$Fe(III)PPIX + ABTS \rightleftharpoons Fe(III)PPIX.ABTS \quad Eq.5.10$$

$$Fe(III)PPIX.ABTS + H_2O_2 \rightleftharpoons Fe(III)PPIX.ABTS.H_2O_2 \quad Eq.5.11$$

$$Fe(III)PPIX.ABTS.H_2O_2 \rightarrow Fe^{\bullet+}(IV)PPIX.ABTS \quad Eq.5.12$$

$$Fe^{\bullet+}(IV)PPIX.ABTS \rightarrow Fe(IV)PPIX{=}O + ABTS^{\bullet+} \quad Eq.5.13$$

de Almeida Ribeiro *et al.* also presented a scheme for Fe(III)PPIX peroxidase like activity involving the complexation between Fe(III)PPIX and ABTS as presented by Adams [168, 74]. They suggested that the complexation prevents degradation of Fe(III)PPIX and oxidised forms of Fe(III)PPIX by direct attack of hydrogen peroxide.

The reaction involving haem and hydrogen peroxide has been analysed to produce models capable of explaining the data collected spectrophotometrically, following the mixture of these compounds. For each model, a set of rate constant and extinction coefficient estimates were yielded to be used in this section for models encompassing the same reactions. The plausible reactions of ABTS has been tested to determine the effect these reactions may have on the full cycle. Under the conditions employed in the collection of the peroxidase cycle data by Sammy [92], the only ABTS interactions deemed necessary to add is a degradation pathway for radical ABTS, as the disproportionation reaction of $ABTS^{\bullet+}$ does not transpire under physiological conditions, and the reaction between ABTS and hydrogen peroxide can only occur with hydrogen peroxide in excess to the chromogen at extremely acidic pH's. As such, all necessary additions are considered and tested in the section to follow.

5.2. Experimental Methods

For instrumentation please see section 3.2.1.

Data used for model-based analysis regarding the peroxidase-like cycle of haem was collected by Sammy during her MSc thesis [92]. The results have been validated, and thus the methods used by Sammy is described in section 4.2.2. of her thesis [92]. In her protocol, the catalytic oxidation of ABTS by H_2O_2 was investigated for a range of Fe(III)PPIX, using an ABTS concentration range of 0.8 and 3.0 mM. Firstly, the concentration of H_2O_2 was varied between 25.0 and 300.0 µM while Fe(III)PPIX was kept at a concentration of 1.0 µM. Secondly, a Fe(III)PPIX concentration range between 0.3 and 1.3 µM was used with a H_2O_2 concentration of 100.0 µM remained constant. Thus, 20 experiments were conducted in total for every concentration of ABTS investigated. The reactions were followed spectrophotometrically at a wavelength of 660 nm to measure the generation of $ABTS^{\bullet+}$ as a function of time. From this data, experimental absorbance sets showing the least deviation were chosen for use in NLLS regression analysis of proposed reaction models. Initial concentrations of reagents for chosen data sets are listed in Table 5.1.

Table 5.1: The initial concentrations of reagents used for the measurement of peroxidase-like activity of Fe(III)PPIX. All concentration ratios used fulfil the required ration of ABTS > H_2O_2 >> Fe(III)PPIX for studying peroxidase-like activity of Fe(III)PPIX [70,92]

Data set	Fe(III)PPIX (µM)	H_2O_2 (µM)	ABTS (µM)
A	0.30	100	2000
B	0.30	100	1500
C	0.60	100	1500
D	0.30	100	1000
E	0.60	100	1000
F	0.60	100	3000
G	0.30	200	3000
H	0.60	200	3000
I	0.30	300	3000
J	0.60	300	3000

5.2.1. Models proposed

Before proposing models, the reaction mechanism to which any additions will be made must be understood. Results in chapter three concluded that model 3(ir)_original best represents the experimental data. Taking the basic interactions of the general cycle with ABTS into account (Figure 1.5), the basis for all models proposed in this chapter to build on will follow reaction steps presented in equations 5.14 to 5.18

$$Fe(III)PPIX + H_2O_2 \rightarrow Fe(III)PPIX.H_2O_2 \qquad Eq.5.14$$

$$Fe(III)PPIX.H_2O_2 \rightarrow I \qquad Eq.5.15$$

$$I \rightarrow Fe^{\bullet+}(IV)PPIX \qquad Eq.5.16$$

$$Fe^{\bullet+}(IV)PPIX + ABTS \rightarrow Fe(IV)PPIX{=}O + ABTS^{\bullet+} \qquad Eq.5.17$$

$$Fe(IV)PPIX{=}O + ABTS \rightarrow Fe(III)PPIX + ABTS^{\bullet+} \qquad Eq.5.18$$

As such, all proposed models in this chapter incorporates these reaction steps. As rate constants for Eq 5.14 to 5.16 has already been determined in chapter 3, these are incorporated into the NLLS regression program as unvarying parameters. Thus, for each model, only the added reaction steps will be presented.

Regarding the proposal of models for this section, the first step is to determine plausible side reactions for the remaining elements of the peroxidase-like reaction not yet approached in previous chapters. The degradation of Fe(IV)PPIX=O serves as example of such a reaction. As the models involving the reaction between Fe(III)PPIX and hydrogen peroxide have already been analysed in chapter 3, only the portion of the peroxidase-like cycle following the production of $Fe^{\bullet+}$(IV)PPIX is presented for subsequent proposal of reaction models. Side reactions are incorporated into each model set to test if the reactions prove relevant. These include Fe(IV)PPIX=O degradation (ox), as well as $ABTS^{\bullet+}$ degradation (ab). To alleviate any confusion regarding nomenclature between models of this chapter and chapter 3, the first model proposed in this chapter is referred to as model 4.

5.3. Results

Model set 4:

Model 4 is based on models proposed by Zipplies *et al.* and Jones (Eq. 5.1 to 5.4), akin to the mechanism presented in Figure 1.5 and shown in equations 5.14 to 5.18 (p4) [73,163] . This reaction model may follow the same trend as model 1 in chapter 3 in terms of goodness-of-fit, as it is reasoned that model 4 does not encompass all factors involved in the peroxidase-like reaction of Fe(III)PPIX. A single NLLS fit for the general model 4_original is presented in Figure 5.1 for visual inspection.

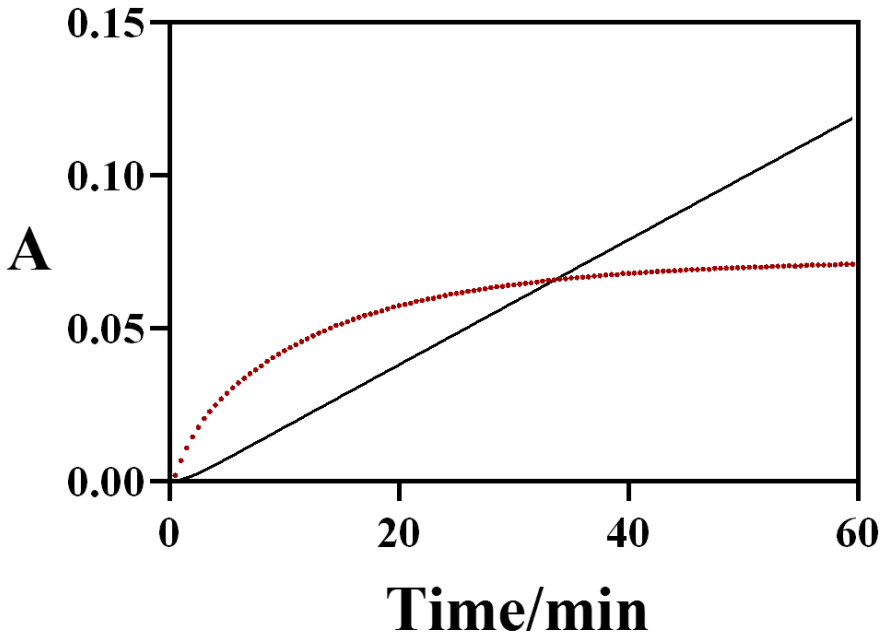

Figure 5.1: Comparison of experimental and theoretical data for the peroxidase-like reaction of Fe(III)PPIX. The reaction was followed at a wavelength of 660 nm for reagent concentrations as stipulated in Table 5.1, data set C. Theoretical data was generated by NLLS regression analysis of model 4_original. The red dots represent experimental data, while the black line denotes model generated data.

Only one NLLS fit is presented in Figure 5.1, as all fits achieved for model 4_original shows the same trend as seen in Figure 5.1. The deviation of theoretical data from absorbance values clearly indicates that model 4_original is inadequate in explaining the experimental data. As such, this model set is rejected.

Model set 5:

The general reaction model for this model set is based on the proposal of a complexation reaction between Fe(III)PPIX and ABTS. However, contrary to the mechanisms proposed by de Almeido Ribeiro *et al.* and Adams, the complexation is proposed to be followed by a one-step reaction of the complex with H_2O_2 to form a $Fe^{\bullet+}$(IV)PPIX=O-ABTS complex, without incorporating an Fe(III)PPIX.ABTS.H_2O_2 complex [5, 6]. The formation of the Fe(III)PPIX.ABTS complex tested for an irreversible model extension, and Fe(IV)PPIX=O and $ABTS^{\bullet+}$ degradation is incorporated individually and together into the general model mechanism, yielding model reaction steps listed in Table 5.2.

Table 5.2: The proposed models for the analysis of model set 5. The rates of the omitted reactions represented by equations 5.17 and 5.18 are represented by k_4 and k_5 for parameters obtained by NLLS regression.

Model	Reaction	Rate constant
5(ir)_original	$H + A \rightarrow H.A$	k_6
	$H.A + P \rightarrow H^{\bullet+}A$	k_7
	$H^{\bullet+}A \rightarrow H{=}O + A^{\bullet+}$	k_8
5(r)_original	$H + A \rightleftharpoons H.A$	k_6 k_{-6}
	$H.A + P \rightarrow H^{\bullet+}A$	k_7
	$H^{\bullet+}A \rightarrow H{=}O + A^{\bullet+}$	k_8
5(ir)_ox	$H + A \rightarrow H.A$	k_6
	$H.A + P \rightarrow H^{\bullet+}A$	k_7
	$H^{\bullet+}A \rightarrow H{=}O + A^{\bullet+}$	k_8
	$H{=}O \rightarrow D1$	k_9
5(r)_ox	$H + A \rightleftharpoons H.A$	k_6 k_{-6}
	$H.A + P \rightarrow H^{\bullet+}A$	k_7
	$H^{\bullet+}A \rightarrow H{=}O + A^{\bullet+}$	k_8
	$H{=}O \rightarrow D1$	k_9
5(ir)_ab	$H + A \rightarrow H.A$	k_6
	$H.A + P \rightarrow H^{\bullet+}A$	k_7
	$H^{\bullet+}A \rightarrow H{=}O + A^{\bullet+}$	k_8
	$A^{\bullet+} \rightarrow D2$	k_{10}
5(r)_ab	$H + A \rightleftharpoons H.A$	k_6 k_{-6}
	$H.A + P \rightarrow H^{\bullet+}A$	k_7
	$H^{\bullet+}A \rightarrow H{=}O + A^{\bullet+}$	k_8
	$A^{\bullet+} \rightarrow D2$	k_{10}
5(ir)_ox_ab	$H + A \rightarrow H.A$	k_6
	$H.A + P \rightarrow H^{\bullet+}A$	k_7
	$H^{\bullet+}A \rightarrow H{=}O + A^{\bullet+}$	k_8
	$H{=}O \rightarrow D1$	k_9
	$A^{\bullet+} \rightarrow D2$	k_{10}
5(r)_ox_ab	$H + A \rightleftharpoons H.A$	k_6 k_{-6}
	$H.A + P \rightarrow H^{\bullet+}A$	k_7
	$H^{\bullet+}A \rightarrow H{=}O + A^{\bullet+}$	k_8
	$H{=}O \rightarrow D1$	k_9
	$A^{\bullet+} \rightarrow D2$	k_{10}

In the above graph H represents monomeric Fe(III)PPIX, P denotes hydrogen peroxide, A represents ABTS, H.P represents the Fe(III)PPIX.H_2O_2 complex, $H^{\bullet+}$ denotes $Fe^{\bullet+}$(IV)PPIX=O, H=O represents Fe(IV)PPIX=O, $A^{\bullet+}$ represents $ABTS^{\bullet+}$, D1 represents H=O degradation products, and D2 denotes $A^{\bullet+}$ degradation products.

NLLS fits of models in Table 5.2 are presented in Figures 5.2 and 5.3 for visual inspection of fits achieved.

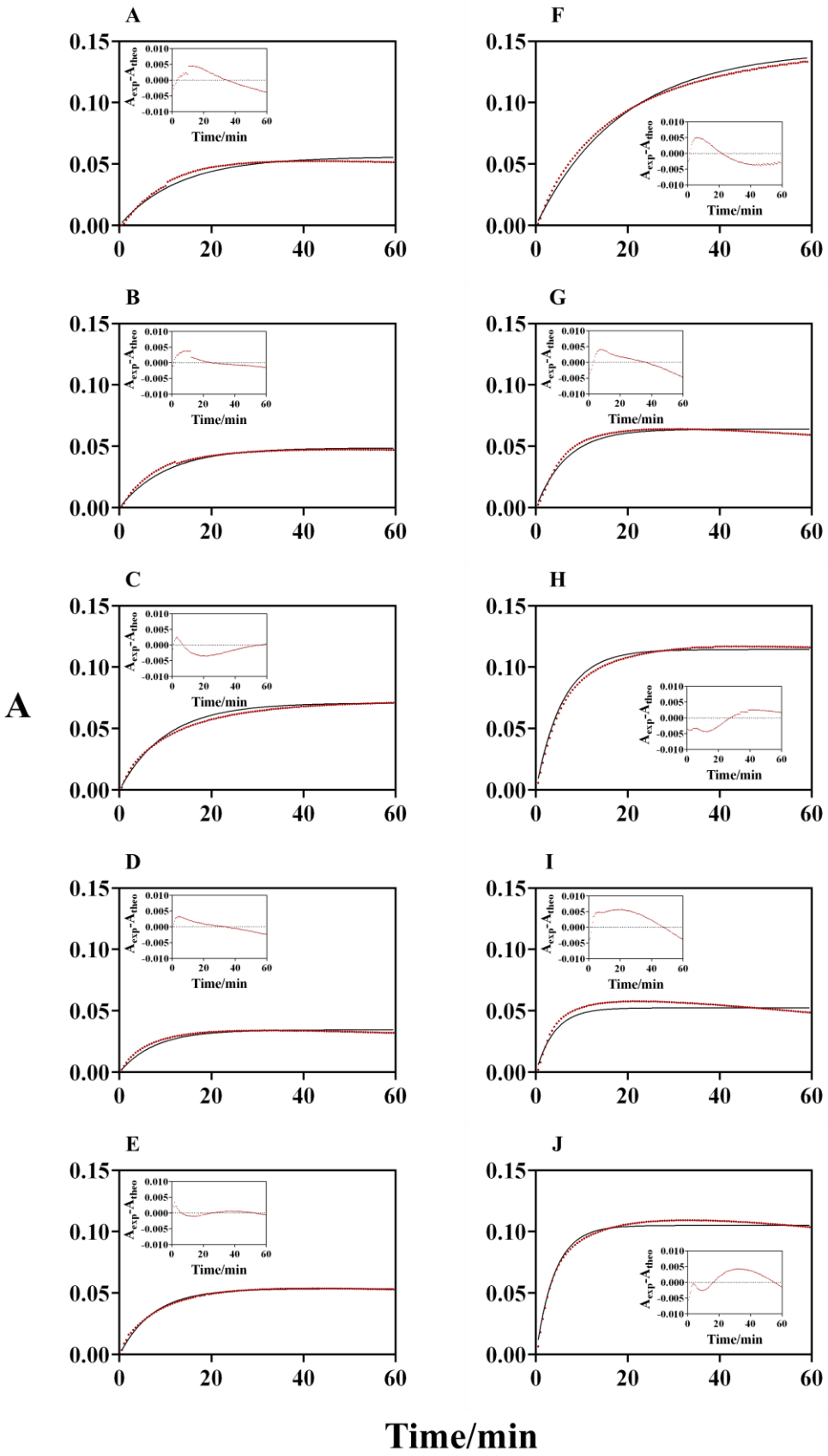

Figure 5.2: Comparison of theoretical and experimental absorbance data for the peroxidase-like reaction of Fe(III)PPIX. The reaction is followed at a wavelength of 660 nm for reagent concentrations as stipulated in Table 5.1 according to the corresponding letter. The red line on main graphs represent experimental values, while the black line denotes model generated data. The model tested is model 5(ir)_original. Insets present the residual plots of every corresponding set of fitted data.

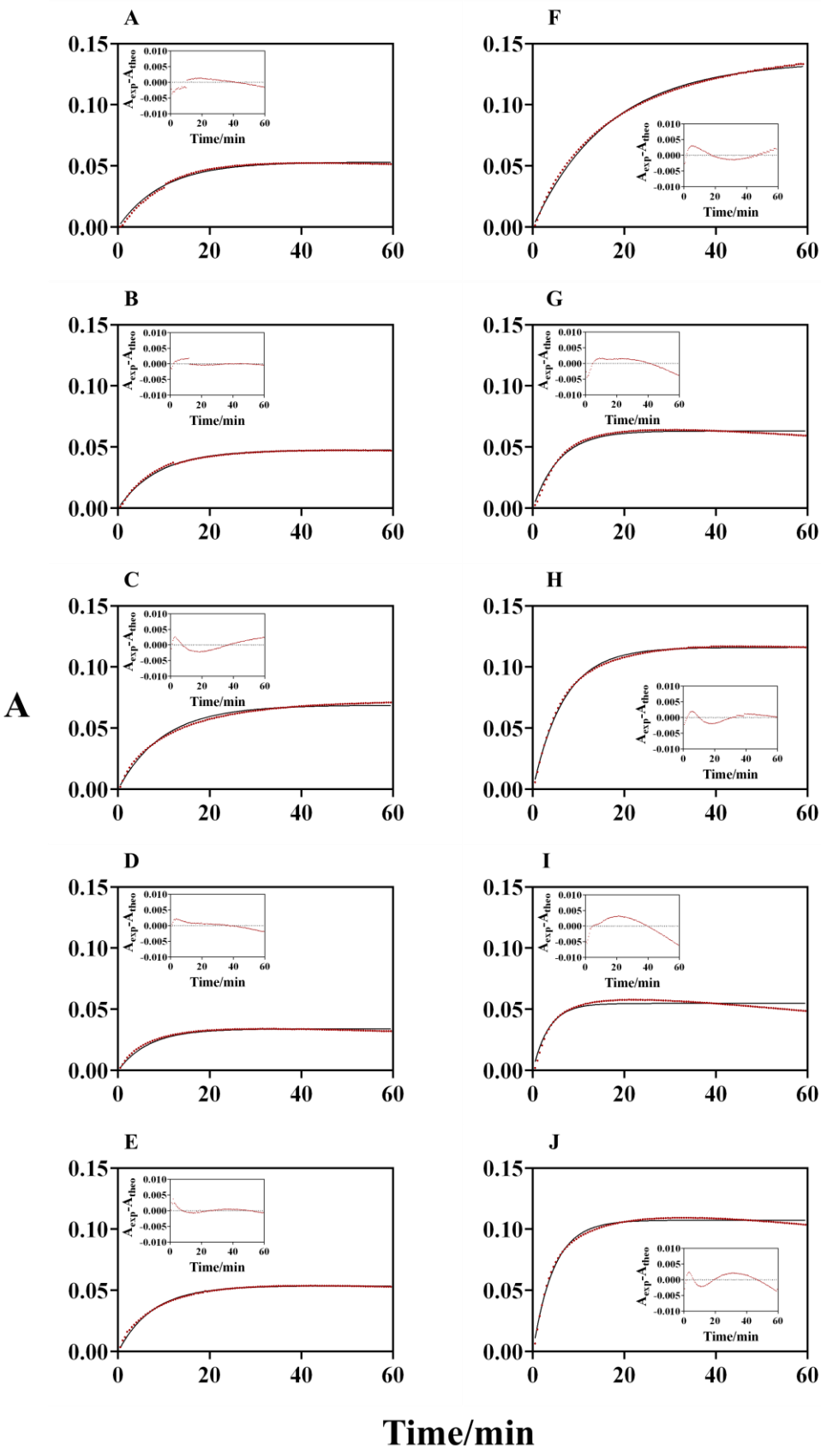

Figure 5.3: Comparison of theoretical and experimental absorbance data for the peroxidase-like reaction of Fe(III)PPIX. The reaction is followed at a wavelength of 660 nm for reagent concentrations as stipulated in Table 5.1 according to the corresponding letter. The red line on main graphs represent experimental values, while the black line denotes model generated data. The model tested is model 5(r)_original. Insets present the residual plots of every corresponding set of fitted data.

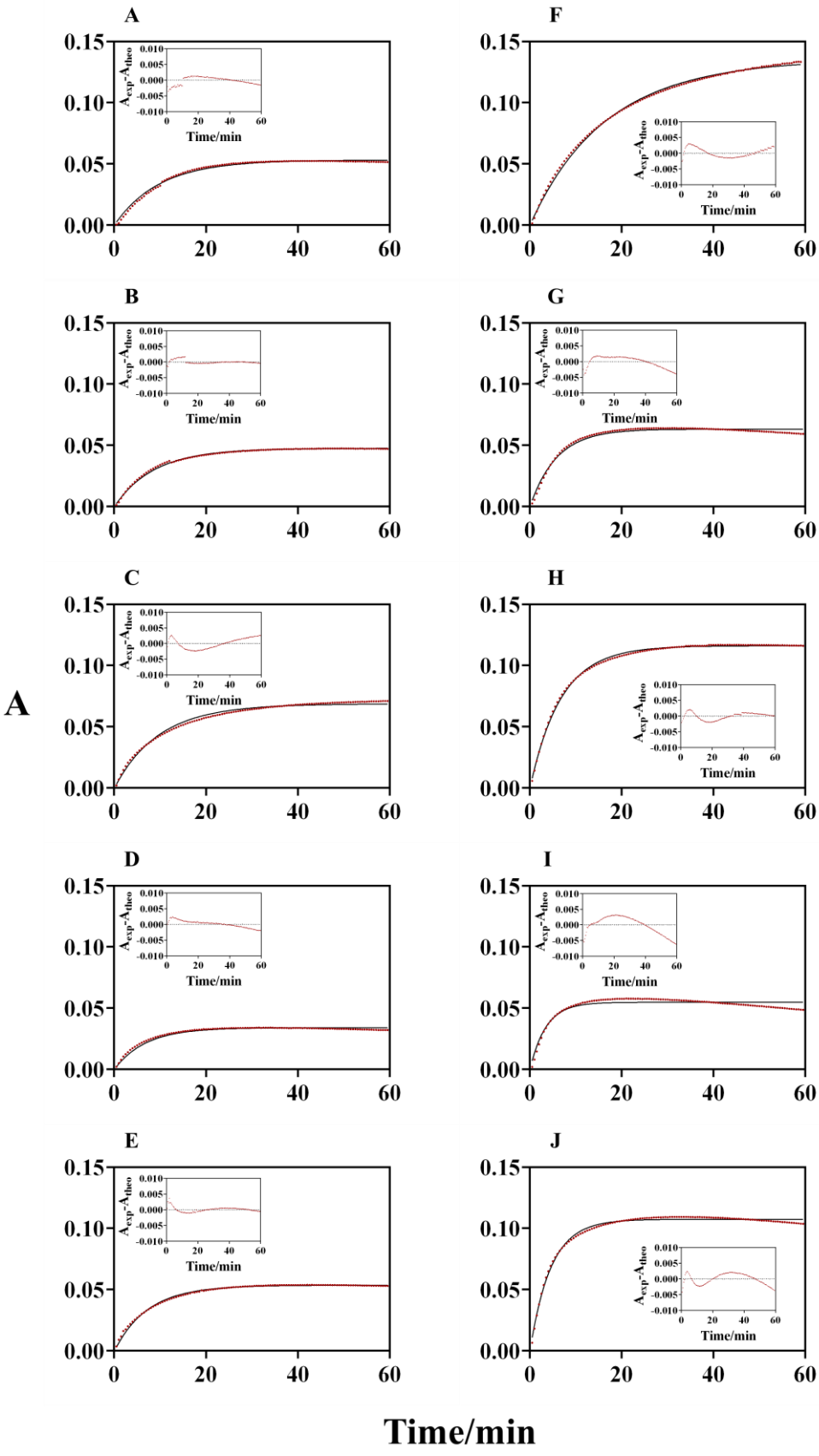

Figure 5.4: Comparison of theoretical and experimental absorbance data for the peroxidase-like reaction of Fe(III)PPIX. The reaction is followed at a wavelength of 660 nm for reagent concentrations as stipulated in Table 5.1 according to the corresponding letter. The red line on main graphs represent experimental values, while the black line denotes model generated data. The model tested is model 5(ir)_ox. Insets present the residual plots of every corresponding set of fitted data.

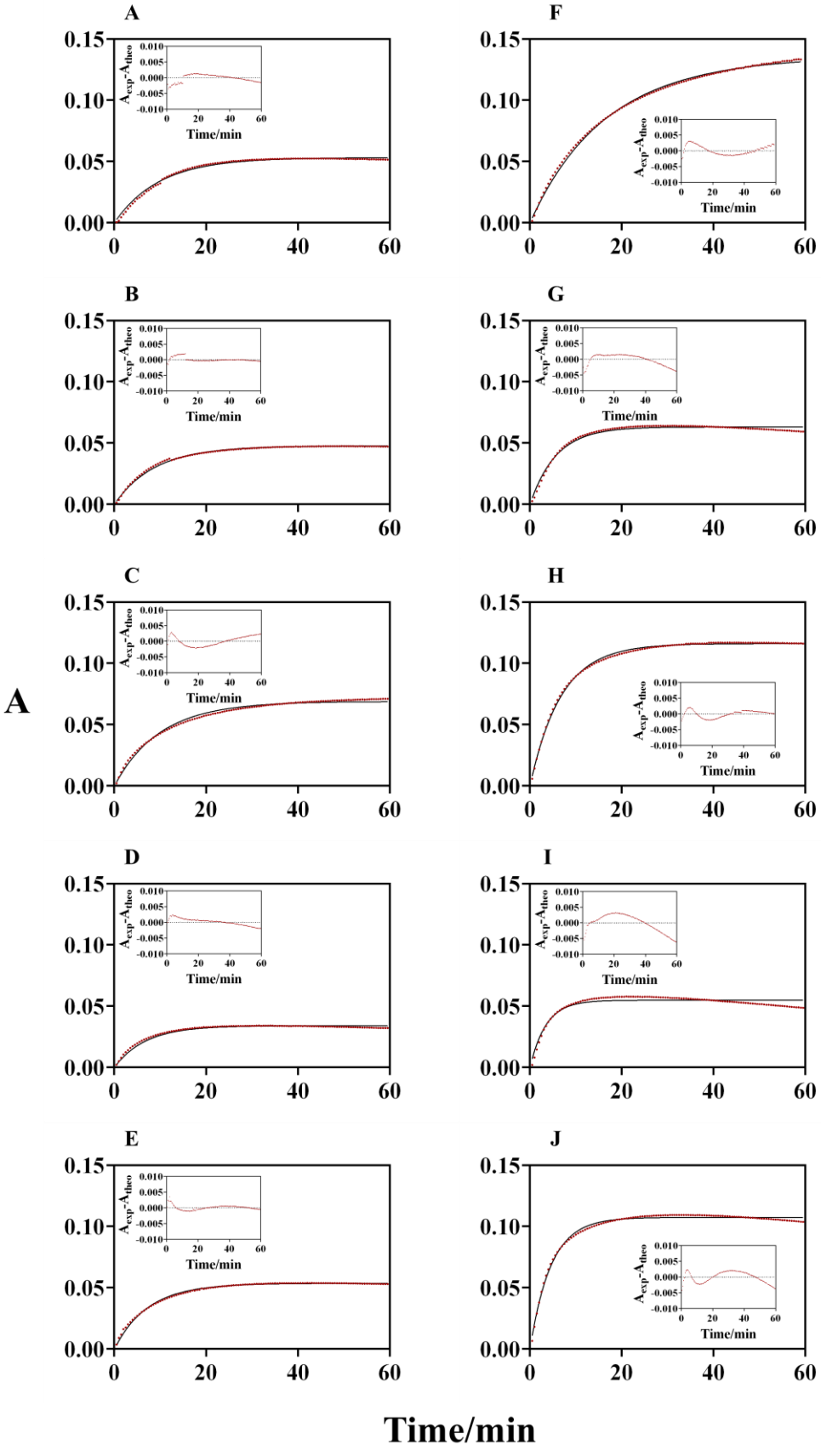

Figure 5.5: Comparison of theoretical and experimental absorbance data for the peroxidase-like reaction of Fe(III)PPIX. The reaction is followed at a wavelength of 660 nm for reagent concentrations as stipulated in Table 5.1 according to the corresponding letter. The red line on main graphs represent experimental values, while the black line denotes model generated data. The model tested is model 5(r)_ox. Insets present the residual plots of every corresponding set of fitted data.

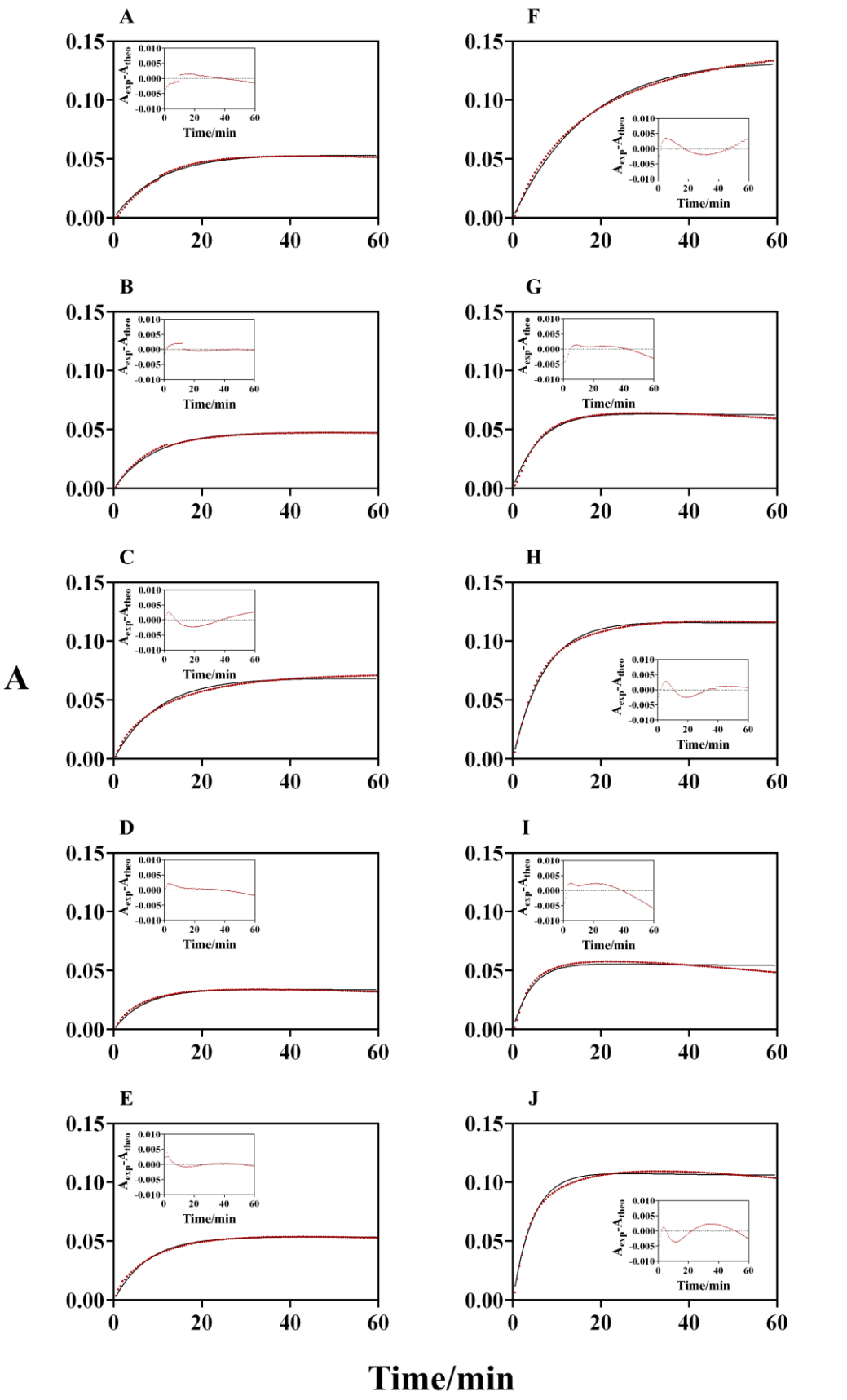

Figure 5.6: Comparison of theoretical and experimental absorbance data for the peroxidase-like reaction of Fe(III)PPIX. The reaction is followed at a wavelength of 660 nm for reagent concentrations as stipulated in Table 5.1 according to the corresponding letter. The red line on main graphs represent experimental values, while the black line denotes model generated data. The model tested is model 5(ir)_ab. Insets present the residual plots of every corresponding set of fitted data

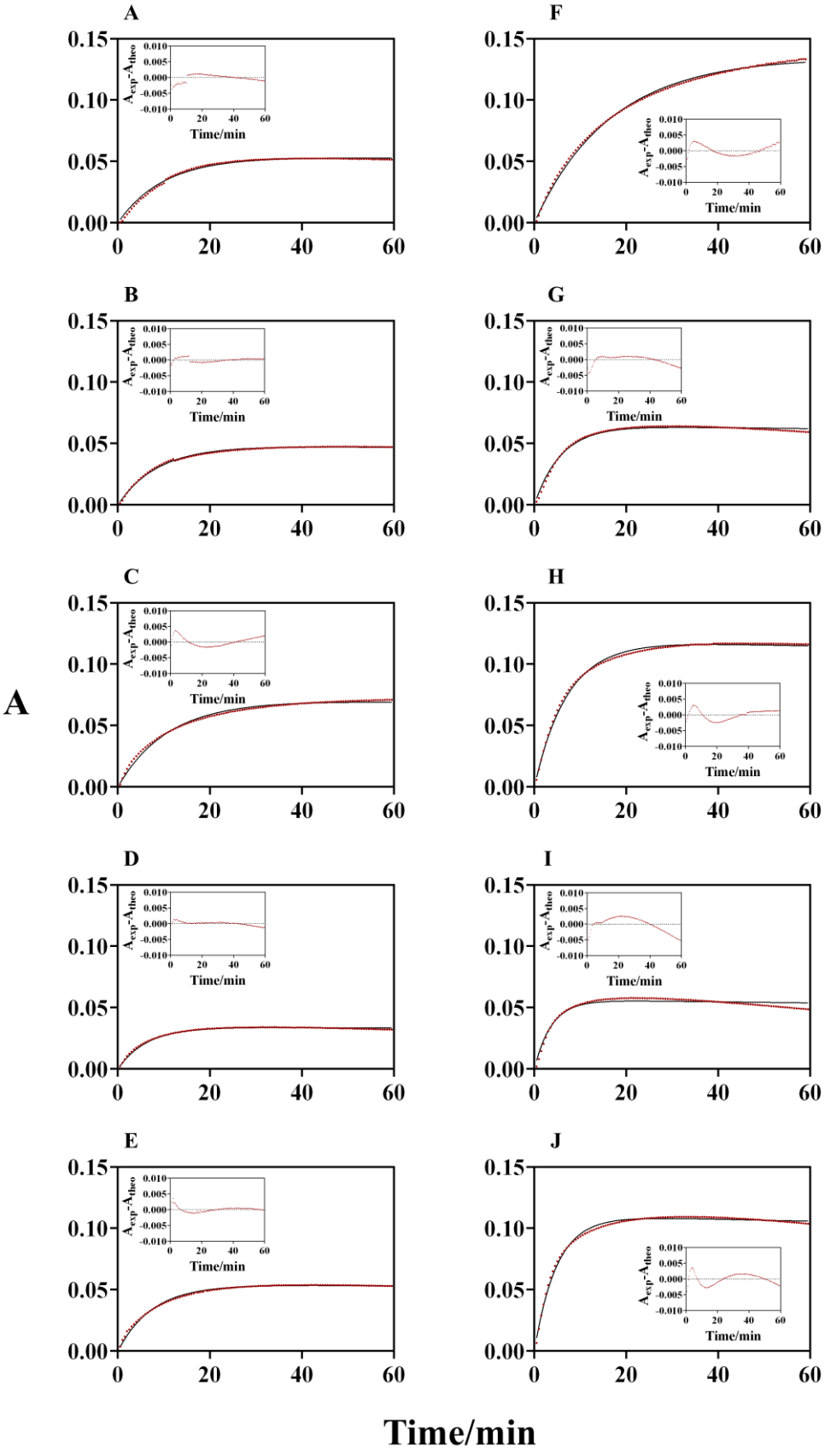

Figure 5.7: Comparison of theoretical and experimental absorbance data for the peroxidase-like reaction of Fe(III)PPIX. The reaction is followed at a wavelength of 660 nm for reagent concentrations as stipulated in Table 5.1 according to the corresponding letter. The red line on main graphs represent experimental values, while the black line denotes model generated data. The model tested is model 5(r)_ab. Insets present the residual plots of every corresponding set of fitted data.

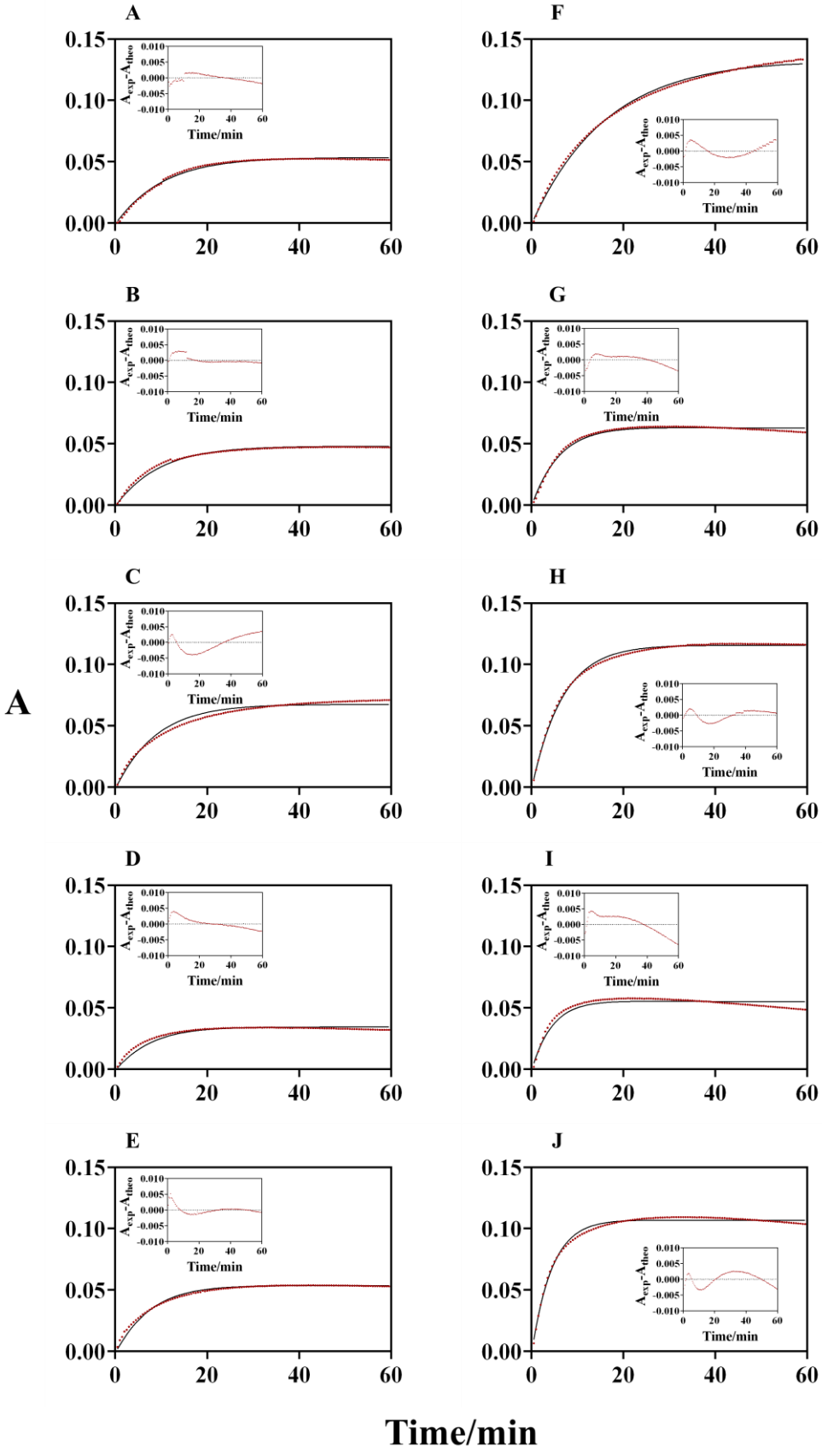

Figure 5.8: Comparison of theoretical and experimental absorbance data for the peroxidase-like reaction of Fe(III)PPIX. The reaction is followed at a wavelength of 660 nm for reagent concentrations as stipulated in Table 5.1 according to the corresponding letter. The red line on main graphs represent experimental values, while the black line denotes model generated data. The model tested is model 5(ir)_ox_ab. Insets present the residual plots of every corresponding set of fitted data.

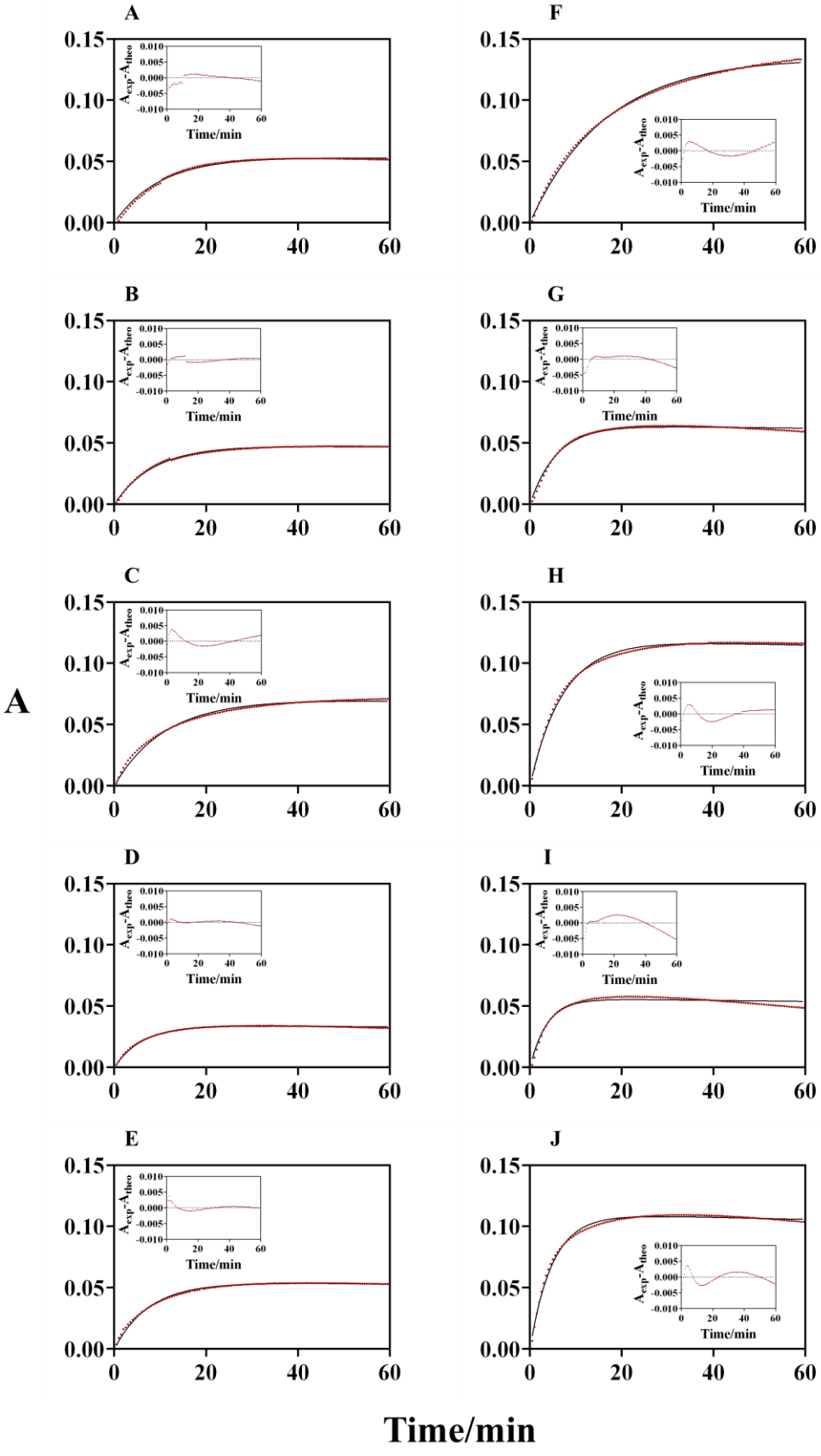

Figure 5.9: Comparison of theoretical and experimental absorbance data for the peroxidase-like reaction of Fe(III)PPIX. The reaction is followed at a wavelength of 660 nm for reagent concentrations as stipulated in Table 5.1 according to the corresponding letter. The red line on main graphs represent experimental values, while the black line denotes model generated data. The model tested is model 5(r)_ox_ab. Insets present the residual plots of every corresponding set of fitted data.

NLLS fits achieved for model 5(ir)_original (Figure 5.2) shows a significant improvement in the goodness-of-fit compared to model 4. Low systematic deviation is observed for models 5(ir)_original and 5(r)_original (Figure 5.3), although in the latter case the error is lower than for the irreversible general model 5, indicating that for this model set the reverse reaction incorporated in the reaction steps is not irrelevant and must be considered. The addition of a Fe(IV)PPIX=O decay step (model 5(ir)_ox in Figure 5.4 and 5(r)_ox in Figure 5.5) seems to marginally worsen the fit or have no effect on models 5(ir)_original and 5(r)_original. This indicates that the addition of Fe(IV)PPIX=O does not improve the fit in any way. The addition of $ABTS^{\bullet+}$ decay to create models 5(ir)_ab (Figure 5.6) and 5(r)_ab (Figure 5.7) improved the NLLS fits achieved for NLLS fits of model 5(ir)_original, showing slightly better correlation of theoretical data to experimental values. No significant effect on the goodness-of-fit could be observed for the addition of the decay step to model 5(r)_original. Improvement in goodness-of-fit could not be distinguished for the addition of both decay steps to model 5(r)_original (Figure 5.9), although a slight decrease in error could be seen for model 5(ir)_ox_ab (Figure 5.8) compared to 5(ir)_original. For Figures 5.2 to 5.9, the models could not account for experimental data in graphs I and J. As observed in Table 5.1, the distinguishing change in conditions for these experiments is the increase of H_2O_2 concentration to 300 µM. Thus, the increase in hydrogen peroxide led to a worse fit. This could be assigned to the increased concentration of peroxide inducing catalase-like activity of Fe(III)PPIX, in which hydrogen peroxide is degraded instead of the expected formation of $ABTS^{\bullet+}$ [70]. Parameters yielded for NLLS regression analysis of relevant model extensions proposed are listed in Table 5.3A (original) 5.3B (ox), 5.3C (ab) and 5.3D (ox_ab).

Table 5.3A: NLLS regression analysis calculated parameter values for models 5(ir)_original and 5(r)_original.

Rate Constants	**5(ir)_original**	**5(r)_original**	**Reaction step**
k_4 $(M^{-1}.s^{-1})$	$(2.12 \pm 0.87) \times 10^{-13}$	$(1.00 \pm 0.62) \times 10^{-17}$	$H^{\bullet+} + A \rightarrow H{=}O + A^{\bullet+}$
k_5 $(M^{-1}.s^{-1})$	$(2.70 \pm 0.19) \times 10^{4}$	$(7.35 \pm 0.69) \times 10^{4}$	$H{=}O + A \rightarrow H + A^{\bullet+}$
k_6 $(M^{-1}.s^{-1})$	(19.0 ± 0.17)	(11.2 ± 0.31)	$H + A \rightarrow H.A$
k_{-6} (s^{-1})	-	(5.27 ± 0.49)	$H.A \rightarrow H + A$
k_7 $(M^{-1}.s^{-1})$	$(5.99 \pm 0.68) \times 10^{-3}$	$(1.11 \pm 0.13) \times 10^{-2}$	$H.A + P \rightarrow H^{\bullet+}A$
k_8 (s^{-1})	$(1.00 \pm 0.20) \times 10^{4}$	$(1.00 \pm 0.17) \times 10^{4}$	$H^{\bullet+}A \rightarrow H{=}O + A^{\bullet+}$
Extinction coefficients	**5(ir)_original**	**5(r)_original**	**Literature** [7, 8]
$ABTS^{\bullet+}$	13500 ± 270	10000 ± 1400	12500

Table 5.3B: NLLS regression analysis calculated parameter values for models 5(ir)_ox and 5(r)_ox.

Rate Constants	5(ir)_ox	5(r)_ox	Reaction step
k_4 $(M^{-1}.s^{-1})$	$(1.05 \pm 0.70) \times 10^{-14}$	$(5.80 \pm 1.02) \times 10^{-14}$	$H^{\bullet+} + A \rightarrow H{=}O + A^{\bullet+}$
k_5 $(M^{-1}.s^{-1})$	(6.24 ± 0.74)	(50.4 ± 7.3)	$H{=}O + A \rightarrow H + A^{\bullet+}$
k_6 $(M^{-1}.s^{-1})$	$(8.86 \pm 1.92) \times 10^{-2}$	$(9.68 \pm 0.67) \times 10^{-2}$	$H + A \rightarrow H.A$
k_{-6} (s^{-1})	-	(3.80 ± 0.32)	$H.A \rightarrow H + A$
k_7 $(M^{-1}.s^{-1})$	$(9.20 \pm 1.31) \times 10^{-2}$	$(1.05 \pm 0.14) \times 10^{-2}$	$H.A + P \rightarrow H^{\bullet+}A$
k_8 (s^{-1})	$(1.00 \pm 0.21) \times 10^{4}$	$(1.00 \pm 0.19) \times 10^{4}$	$H^{\bullet+}A \rightarrow H{=}O + A^{\bullet+}$
k_9 (s^{-1})	$(9.21 \pm 0.49) \times 10^{2}$	(6.78 ± 0.84)	$H{=}O \rightarrow D1$
Extinction coefficients	**5(ir)_ox**	**5(r)_ox**	**Literature** [7, 8]
$ABTS^{\bullet+}$	11000 ± 270	10000 ± 1400	12500

Table 5.3C: NLLS regression analysis calculated parameter values for models 5(ir)_ab and 5(r)_ab.

Rate Constants	5(ir)_ab	5(r)_ab	Reaction step
k_4 $(M^{-1}.s^{-1})$	$(3.72 \pm 0.10) \times 10^{-4}$	(9.66 ± 1.10)	$H^{\bullet+} + A \rightarrow H{=}O + A^{\bullet+}$
k_5 $(M^{-1}.s^{-1})$	(27.4 ± 3.52)	$(1.79 \pm 0.33) \times 10^{2}$	$H{=}O + A \rightarrow H + A^{\bullet+}$
k_6 $(M^{-1}.s^{-1})$	$(1.66 \pm 0.21) \times 10^{-2}$	$(1.51 \pm 0.60) \times 10^{-2}$	$H + A \rightarrow H.A$
k_{-6} (s^{-1})	-	(4.35 ± 0.61)	$H.A \rightarrow H + A$
k_7 $(M^{-1}.s^{-1})$	$(1.18 \pm 0.30) \times 10^{-2}$	$(1.33 \pm 0.14) \times 10^{-2}$	$H.A + P \rightarrow H^{\bullet+}A$
k_8 (s^{-1})	$(1.00 \pm 0.21) \times 10^{4}$	$(1.00 \pm 0.09) \times 10^{4}$	$H^{\bullet+}A \rightarrow H{=}O + A^{\bullet+}$
k_{10} (s^{-1})	$(2.76 \pm 0.49) \times 10^{-2}$	$(3.63 \pm 0.24) \times 10^{-2}$	$A^{\bullet+} \rightarrow D2$
Extinction coefficients	**5(ir)_ab**	**5(r)_ab**	**Literature** [7, 8]
$ABTS^{\bullet+}$	13300 ± 760	11000 ± 1100	12500

Table 5.3D: NLLS regression analysis calculated parameter values for models 5(ir)_ox_ab and 5(r)_ox_ab.

Rate Constants	5(ir)_ox_ab	5(r)_ox_ab	Reaction step
k_4 $(M^{-1}.s^{-1})$	$(1.45 \pm 0.13) \times 10^{-4}$	(2.87 ± 0.22)	$H^{\bullet+} + A \rightarrow H{=}O + A^{\bullet+}$
k_5 $(M^{-1}.s^{-1})$	(92.3 ± 8.73)	(65.2 ± 5.03)	$H{=}O + A \rightarrow H + A^{\bullet+}$
k_6 $(M^{-1}.s^{-1})$	$(2.08 \pm 0.30) \times 10^{-2}$	$(1.59 \pm 0.16) \times 10^{-2}$	$H + A \rightarrow H.A$
k_{-6} (s^{-1})	-	(5.00 ± 0.39)	$H.A \rightarrow H + A$
k_7 $(M^{-1}.s^{-1})$	$(1.24 \pm 0.15) \times 10^{-2}$	$(1.36 \pm 0.12) \times 10^{-2}$	$H.A + P \rightarrow H^{\bullet+}A$
k_8 (s^{-1})	$(1.00 \pm 0.07) \times 10^{4}$	$(1.00 \pm 0.08) \times 10^{4}$	$H^{\bullet+}A \rightarrow H{=}O + A^{\bullet+}$
k_9 (s^{-1})	$(5.84 \pm 1.97) \times 10^{-10}$	(3.42 ± 0.29)	$H{=}O \rightarrow D1$
k_{10} (s^{-1})	$(2.76 \pm 0.49) \times 10^{-2}$	$(2.42 \pm 0.24) \times 10^{-2}$	$A^{\bullet+} \rightarrow D2$
Extinction coefficients	**5(ir)_ox_ab**	**5(r)_ox_ab**	**Literature** [7, 8]
$ABTS^{\bullet+}$	11000 ± 760	11000 ± 1100	12500

The rate constants k_4 (Table 5.3) for the reaction between Fe$^{\bullet+}$(IV)PPIX=O and ABTS are very low, below $1 \times 10^{-10}\ M^{-1}.s^{-1}$, for the original models as well as for models 5(ir)_ox and 5(r)_ox, meaning that for these models, for all intents and purposes, the reaction does not occur. This rate constant is considered more reliable for models incorporating ABTS$^{\bullet+}$ decay. The lowered k_4 is most likely due to the complexation of Fe(III)PPIX and ABTS preventing degradation or deactivation of Fe(III)PPIX. As such, the reaction using this pathway should be more likely as it is then the path via which the iron porphyrin can avoid degradation. The conversion rate of Fe$^{\bullet+}$(IV)PPIX=O.ABTS reaction to produce Fe(IV)PPIX=O and ABTS$^{\bullet+}$ remains at a constant values of 1.00×10^4 throughout model extensions made. Reverse reaction rates of the Fe(III)PPIX.ABTS complexation are in good correlation between models. Rate constants for the decay steps incorporated (k_9 for Fe(IV)PPIX=O decay and k_{10} for ABTS$^{\bullet+}$ decay) show values within believable ranges for k_{10}; however, k_9 fluctuates for the change of the reversible reaction to irreversible, as well as for the addition of ABTS$^{\bullet+}$ decay. The extinction coefficients calculated for ABTS$^{\bullet+}$ correlates well with literature values.

Model set 6:

The reaction steps incorporated into the general model 6 (6(r)_original) is as proposed by de Almeida Ribeiro *et al.* [74]. The formation of the Fe$^{\bullet+}$(IV)PPIX=O.ABTS complex now follows the formation of a Fe(III)PPIX.ABTS complex with H_2O_2. The latter reaction is deemed reversible, and the general model is extended to include model 6(ir)_original, with both model mechanisms listed in Table 5.4.

Table 5.4: The model extensions proposed for model set 6. The rates of the omitted reactions represented by equations 5.17 and 5.18 are represented by k_4 and k_5 for parameters obtained by NLLS regression.

Model	Reaction	Rate constant
6(ir)_original	$H + A \rightarrow H.A$	k_6
	$H.A + P \rightarrow HAP$	k_7
	$HAP \rightarrow H^{\bullet+}A$	k_8
	$H^{\bullet+}A \rightarrow H{=}O + A^{\bullet+}$	k_9
6(r)_original	$H + A \rightleftharpoons H.A$	k_6 k_{-6}
	$H.A + P \rightarrow HAP$	k_7
	$HAP \rightarrow H^{\bullet+}A$	k_8
	$H^{\bullet+}A \rightarrow H{=}O + A^{\bullet+}$	k_9

H represents monomeric Fe(III)PPIX, P represents H_2O_2, A represents ABTS, $H^{\bullet+}$ represents Fe$^{\bullet+}$(IV)PPIX=O, H=O represents Fe(IV)PPIX=O and $A^{\bullet+}$ represents ABTS$^{\bullet+}$.

NLLS fits obtained for models listed in Table 5.4 are shown in Figures 5.4 and 5.5 for visual inspection.

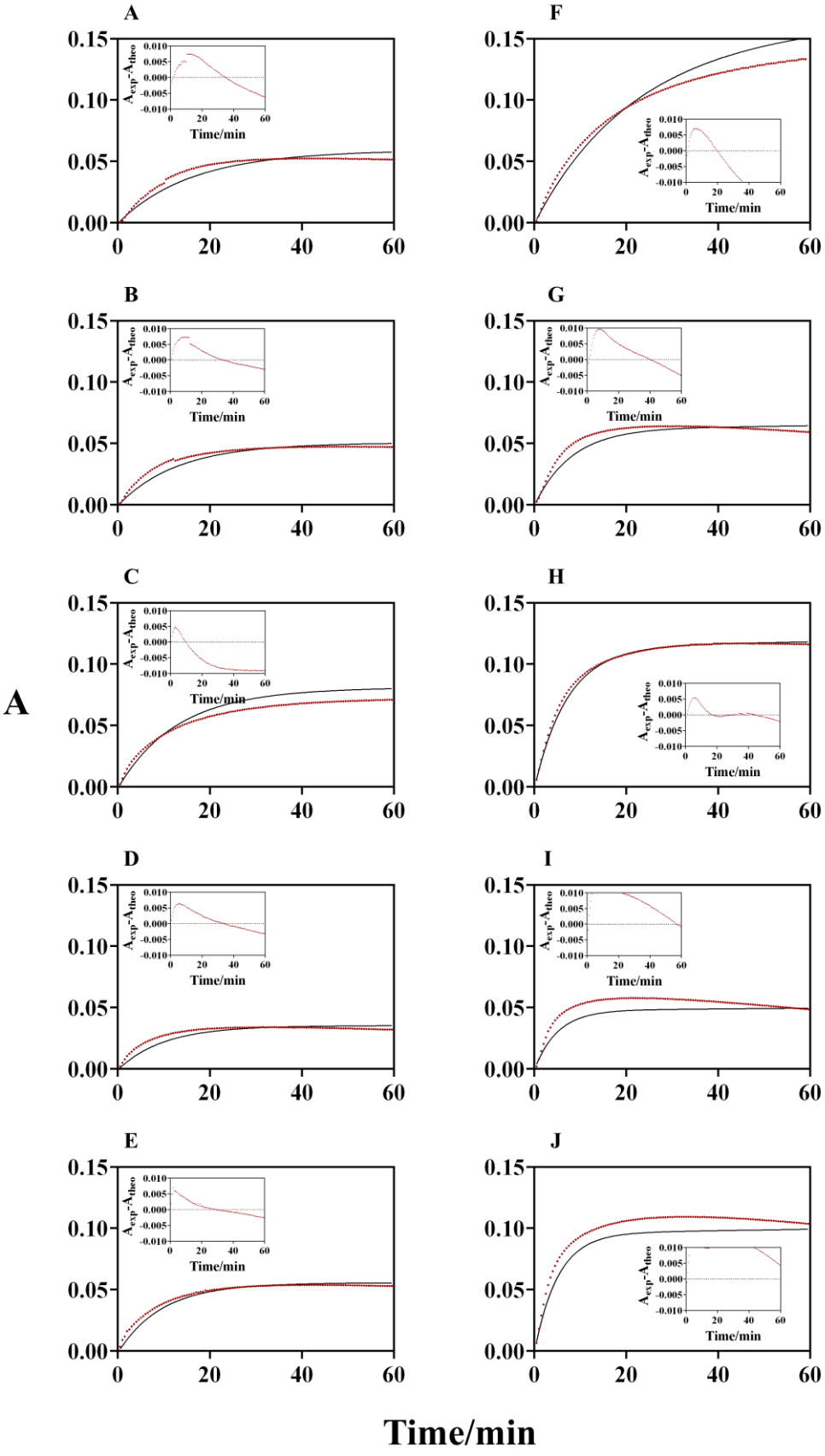

Figure 5.10: Comparison of theoretical and experimental absorbance data for the peroxidase-like reaction of Fe(III)PPIX. The reaction is followed at a wavelength of 660 nm for reagent concentrations as stipulated in Table 5.1 according to the corresponding letter. The red line on main graphs represent experimental values, while the black line denotes model generated data. The model tested is model 6(ir)_original. Insets present the residual plots of every corresponding set of fitted data.

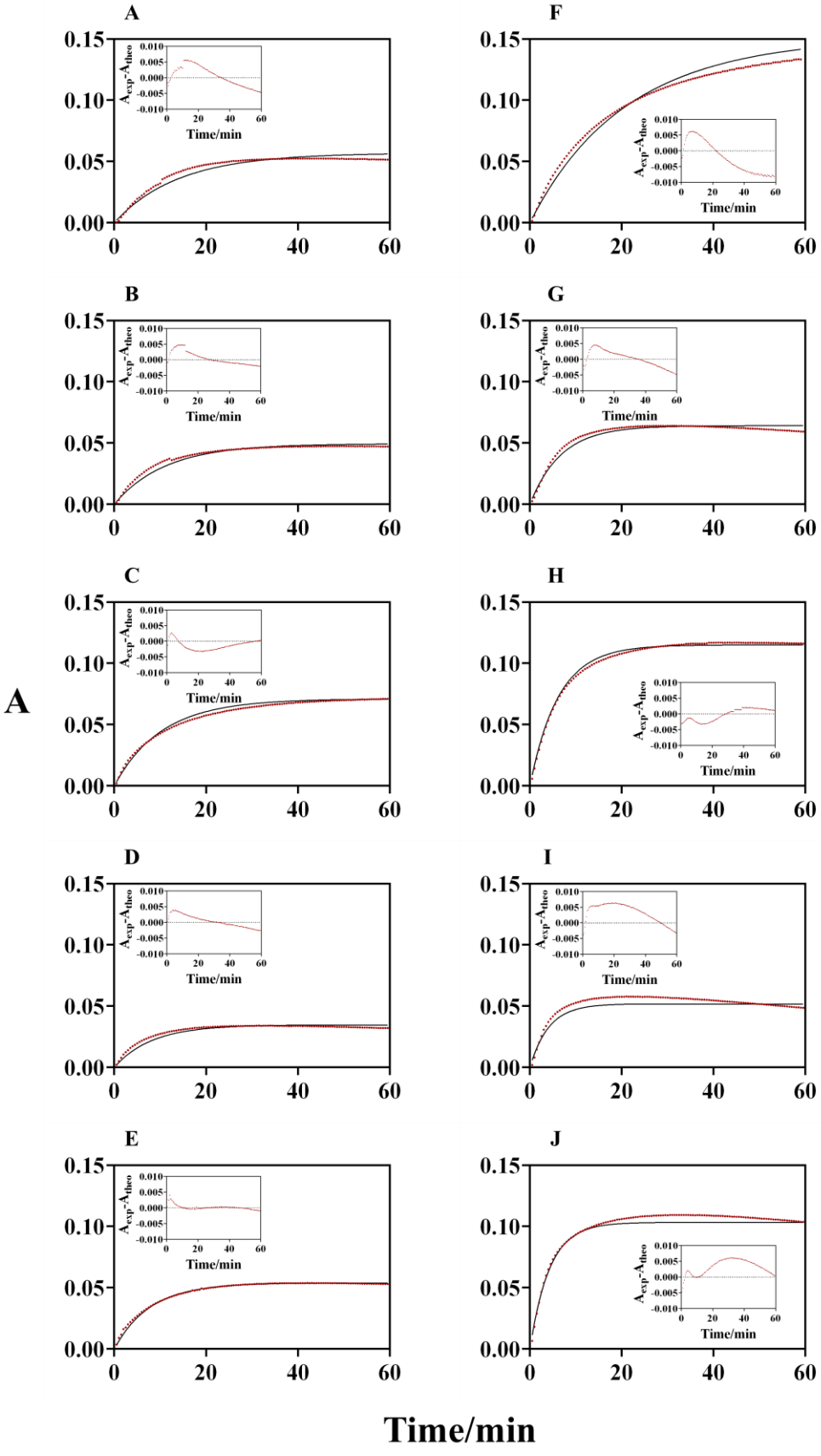

Figure 5.11: Comparison of theoretical and experimental absorbance data for the peroxidase-like reaction of Fe(III)PPIX. The reaction is followed at a wavelength of 660 nm for reagent concentrations as stipulated in Table 5.1 according to the corresponding letter. The red line on main graphs represent experimental values, while the black line denotes model generated data. The model tested is model 6(r)_original. Insets present the residual plots of every corresponding set of fitted data.

NLLS fits obtained for models 6(ir)_original (Figure 5.9) and 6(r)_original (Figure 5.10) show worse correlation to experimental data than observed for model 5. Clearly the addition of a Fe(III)PPIX.H_2O_2.ABTS complex is not plausible, thus decreasing the goodness-of-fit. Residual plots indicate systematic deviation for almost every plot presented for models of model set 6. To compare models 5 and 6, error statistics for each model extension are listed in Table 5.5.

Table 5.5: The regression statistics for analysis of model fit error. SSQ and Chi-Square values are included. rRMS is omitted as it is a repetition of the sum of squares, as a percentage.

Model	SSQ	Chi-Square
5(ir)_original	8.07×10^{-3}	17.6×10^{-2}
5(r)_original	2.77×10^{-3}	8.50×10^{-2}
5(ir)_ox	2.82×10^{-3}	8.51×10^{-2}
5(r)_ox	2.76×10^{-3}	8.54×10^{-2}
5(ir)_ab	2.88×10^{-3}	8.21×10^{-2}
5(r)_ab	2.32×10^{-3}	7.54×10^{-2}
5(ir)_ox_ab	3.99×10^{-3}	11.3×10^{-2}
5(r)_ox_ab	2.30×10^{-3}	7.54×10^{-2}
6(ir)_original	0.0484	86.9×10^{-2}
6(r)_original	0.0129	25.1×10^{-2}

The SSQ values for models 6(ir)_original and 6(r)_original (Table 5.5) are the poorest of the models tested, with a lower SSQ for 6(r)_original (0.012856). Compared to the highest SSQ value amongst model 5 extensions, 0.008073 for 5(ir)_original, the error model 6 encompasses along with the deviation observed in Figures 5.9 and 5.10 shows that model six cannot explain the absorbance data and as such rejection of model 6 is suggested. An important observation to make is that, for model 5 every reaction that includes the reversible complexation of Fe(III)PPIX and ABTS, a lower error statistic is achieved than for the irreversible complexation. 5(r)_original, for example, has a Chi-Square value of 8.52×10^{-2}, which is less than half of the Chi-Square statistic of 5(ir)_original (17.6×10^{-2}). According to regression statistics determined, model 5(r)_ab described the kinetic reaction best, closely followed by model 5(r)_ox_ab. To validate this inference, model comparison analysis was performed, and the results listed in Table 5.6

Table 5.6: Model comparison statistics presented for determination of the best overall representation of the peroxidase-like cycle of Fe(III)PPIX. The AIC, BIC and KLD statistics are presented. The highlighted rows represent the best (green) and second best (blue) models

Model	AIC	BIC	KLD
5(ir)_original	-7.10×10^5	-7.10×10^5	10.74×10^{-4}
5(r)_original	-7.59×10^5	-7.59×10^5	5.68×10^{-4}
5(ir)_ox	-7.59×10^5	-7.58×10^5	5.64×10^{-4}
5(r)_ox	-7.59×10^5	-7.59×10^5	5.68×10^{-4}
5(ir)_ab	-7.58×10^5	-7.57×10^5	5.4×10^{-4}
5(r)_ab	-7.67×10^5	-7.67×10^5	5.07×10^{-4}
5(ir)_ox_ab	-7.43×10^5	-7.43×10^5	6.86×10^{-4}
5(r)_ox_ab	-7.68×10^5	-7.68×10^5	5.07×10^{-4}
6(ir)_original	-6.29×10^5	-6.29×10^5	48.12×10^{-4}
6(r)_original	-6.89×10^5	-6.89×10^5	14.83×10^{-4}

The information lost (KLD) by model 6 is higher than for original models of model set 5. This substantiates the suggestion that model six can be rejected as it does not offer the best approximation of the experimental data. Original models of model set 5 show the least correlation to the kinetic reaction, while models containing the $ABTS^{\bullet+}$ decay reaction step obtained lower values for the information criteria. The model indicated as the one with the lowest error as compared to its complexity is model 5(r)_ab.

5.4. Conclusion

The potential reaction models for the peroxidase-like cycle of Fe(III)PPIX have been studied. The first proposed model incorporated the reaction as presented in Figure 1.5 of chapter 1 and was denoted as model set 4 in this chapter. NLLS regression analysis yielded model generated data with no correlation to the experimental absorbance values. Thus, model set 4 is rejected as no fit is achieved. The second model set proposed includes the complexation of Fe(III)PPIX and ABTS according to the mechanisms proposed by Adams and de Almeida Ribeiro [5, 6]. An alteration was made by the removal of a complexation of H_2O_2 to Fe(III)PPIX.ABTS. NLLS fits obtained indicated that the reversible reaction ABTS-haematin complexation is relevant to the model for its ability to elucidate the experimental data. An observation made is that the addition of Fe(IV)PPIX=O decay did not significantly affect the fits obtained for 5_original models. Incorporation of the decay of $ABTS^{\bullet+}$ led to an

improved fit, as well as more viable parameters yielded by NLLS regression, such as the reaction rate k_4 of $Fe^{\bullet+}$(IV)PPIX=O with ABTS. Model six includes the complexation excluded from model 5 where NLLS fits deviated noticeably from experimental data. Regression statistics determined model six to be more erroneous than model 5, which was substantiated by comparison of AIC, BIC and KLD values. These same model comparison statistics verified the importance of the reverse reaction of ABTS-Fe(III)PPIX complexation. Both regression statistics indicate that model 5(r)_ab yielded the best fit, with model 5(r)_ox_ab performing marginally poorer. As the margin of difference is very small, and the decay of Fe(IV)PPIX did not significantly affect goodness-of-fit, the simpler model is believed best. Thus, the peroxidase-like activity of Fe(III)PPIX can be described by scheme 5.1. As presented in Scheme 5.1, the peroxidase-like activity of Fe(III)PPIX can be explained by the green cycle and red bar. This cycle represents the three step reaction of Fe(III)PPIX with H_2O_2 to form $Fe^{\bullet+}$(IV)PPIX=O, as stipulated in model 3(ir)_original. The radical porphyrin compound can convert two molecules of ABTS to $ABTS^{\bullet+}$, but is in the process reduced to Fe(IV)PPIX=O, and then Fe(III)PPIX. However, in order to fully account for the experimental data using ABTS as chromogen, the association between the catalyst and chromogen is incorporated to create the additional reactions represented as a blue cycle.

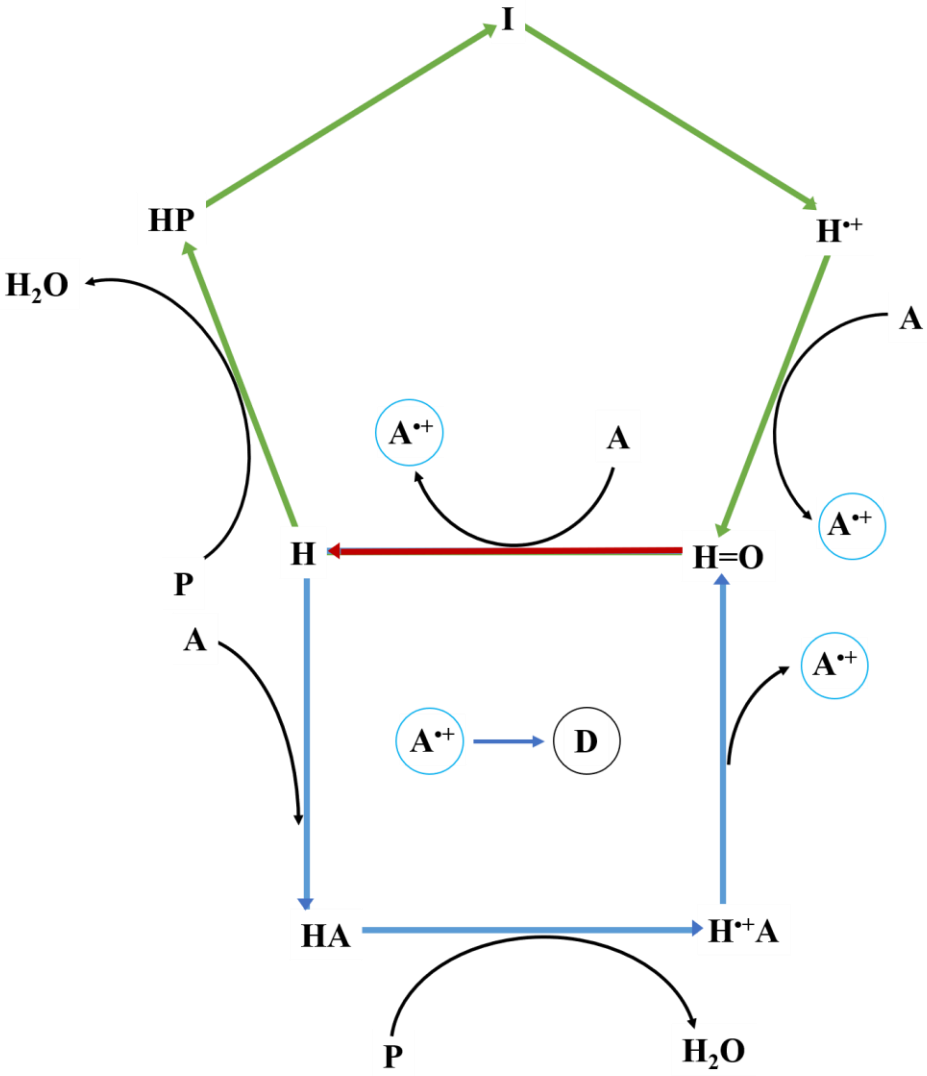

Scheme 5.1: The proposed mechanism of the peroxidase-like activity of haem. The green cycle is the general mechanism as presented for haem containing peroxidases [158]*. The blue cycle is the incorporated ABTS complexation cycle as proposed in literature* [5, 6]*. The mechanism presented offers the best explanation for the kinetic qualities of the peroxidase-like reaction of Fe(III)PPIX. H represents haem, HP represents peroxohaem, P represents hydrogen peroxide, $H^{\bullet+}$ represents $Fe^{\bullet+}$(IV)PPIX=O, A represents ABTS, H=O represents Fe(IV)PPIX=O, HA represents a Fe(III)PPIX.ABTS complex, I represents the active intermediate, $H^{\bullet+}A$ represents a $Fe^{\bullet+}$(IV)PPIX=O.ABTS complex, $A^{\bullet+}$ represents ABTS radical and D represents degraded products.*

6. Conclusion

Malaria is a disease that continues to persist in the modern world. As the *Plasmodium* parasite causing this disease continuously develops resistance against current antimalarial treatments, there is a necessity for the development of new antimalarial compounds. However, to assist in the proposal of novel antimalarial drugs, the mechanism by which current antimalarials elicits their activity needs to be known. The activity of quinoline and artemisinin derivatives is known to affect free haem released within malarial parasites by parasite induced degradation of haemoglobin of the erythrocytes it has infected. There is disparity on the specific mechanisms of these antimalarials, although it is known to either directly or indirectly influence the toxicity of the free haem moiety [92, 117]. Before the exact effect of antimalarial compounds on haem toxicity can be extrapolated, the toxicity of haem itself must be investigated. Iron protoporphyrin IX specifically is used for biological relevance. In this study, the toxicity of haem was elucidated by analysis of the peroxidase-like activity of this porphyrin moiety, to determine the mechanism best suited to explain how haem facilitates its toxicity.

A model-based analysis of kinetic data collected was conducted using NLLS regression. For this process, an in-house program $RunFit$ was coded in MatLab for analysis of multivariate kinetic data using the Nelder Mead simplex algorithm [140]. The purpose of the algorithm is to minimize a function value like SSQ, which represents the quantified error of the correlation of theoretical data to experimental values. Thus, the algorithm reduces the error of the fit to the point that a decrease in error is no longer possible (i.e. a minimum point is reached), after which an output of optimised parameters is yielded. As MatLab, and thus $RunFit$, is computationally expensive, DynaFit was utilised to optimise parameters for alleviation of the time consumed in the model fitting process. Regression statistics such as SSQ, rRMS and Chi-Square statistics were used to analyse the deviation of NLLS regression generated theoretical data from experimental data collected for portions of the peroxidase-like cycle. AIC, BIC and KLD were used for model fit comparison analysis achieved to determine which model best describes the reaction mechanism studied.

Probable models for the reaction of Fe(III)PPIX with H_2O_2 were subjected to NLLS regression analysis against the collected spectrophotometric data. Model 1 denotes the reaction of Fe(III)PPIX and H_2O_2 to form $Fe^{\bullet+}$(IV)PPIX in a one-step reaction. Model 2 incorporates the reversible complexation of Fe(III)PPIX and H_2O_2 to form a Fe(III)PPIX.H_2O_2 complex. The complex can convert to $Fe^{\bullet+}$(IV)PPIX=O. Addition of a second intermediate step yields model set 3. Formation of the Fe(III)PPIX.H_2O_2 complex is followed by a reversible conversion of the complex to an active intermediate I, which in turn can form $Fe^{\bullet+}$(IV)PPIX=O. NLLS fits obtained for model 1 showed that the model offers an inadequate description of the experimental data. Model 2 shows improvement in fits achieved, with the addition of $Fe^{\bullet+}$(IV)PPIX=O decay improving the NLLS fit significantly. A substantial improvement in NLLS fit is seen for model 3. For model extensions tested, model 3(ir)_original presents the best

explanation for the reaction of Fe(III)PPIX with hydrogen peroxide. The model extension is the general model 3 with irreversible conversion of Fe(III)PPIX.H_2O_2 to the active intermediate *I*.

Potential reactions of ABTS, other than that presented in Figure 1.5, have been investigated. Regarding the oxidation of ABTS with H_2O_2, the oxidant was found to be unable to oxidise ABTS for pH levels of 4.8 and 7.5. ABTS reacting with HNO_3 resulted in formation of $ABTS^{\bullet+}$, followed by $ABTS^{2+}$ production. As the acid has a lower electron affinity than $ABTS^{2+}/ABTS^{\bullet+}$, the formation of the dication species was attributed to the disproportionation of $ABTS^{\bullet+}$. MnO_4^- is used to oxidise ABTS for pH levels of 4.8 and 7.5, of which the results suggest that the disproportionation reaction is irrelevant at pH levels approaching physiologically relevant conditions. No significant degradation of ABTS at pH 4.8 and 7.5 was observed. $ABTS^{\bullet+}$ did show slow degradation for a pH of 4.8. For analysis of the peroxidase-like model, only $ABTS^{\bullet+}$ decay was considered a viable side reaction. The complexation of Fe(III)PPIX and ABTS to participate in the peroxidase-like cycle to form a second catalytic pathway was also included.

The potential reaction models for the peroxidase-like cycle of Fe(III)PPIX have been studied. Model set 4 incorporated the reaction as presented in Figure 1.5 of chapter 1. NLLS fits obtained from this model showed no correlation to experimental data. Model set 5 incorporates the complexation of Fe(III)PPIX and ABTS loosely based on the mechanisms proposed by Adams and de Almeida Ribeiro [5, 6]. Complexation of H_2O_2 to Fe(III)PPIX.ABTS was omitted from the reaction steps. NLLS fits obtained show that reversibility of the complexation of Fe(III)PPIX and ABTS is important for the model goodness-of-fit. Incorporating Fe(IV)PPIX=O decay did not significantly affect the fits obtained for 5_original models. However, addition of $ABTS^{\bullet+}$ decay improved model goodness-of-fits achieved. Model 6 includes the complexation omitted from model 5. NLLS fits for model 6 deviated noticeably from experimental data. Regression and model comparison statistics showed model 5 explains the reaction studied better. AIC, BIC and KLD statistics calculated verified the necessity of the reverse reaction of ABTS-Fe(III)PPIX complexation. Model 5(r)_ab is concluded to be the best presented model.

The model thus elicited as best describing the peroxidase-like cycle of haem involves the following reaction steps. First Fe(III)PPIX and H_2O_2 complexes irreversibly to form a Fe(III)PPIX.H_2O_2 complex. This complex converts to a reactive intermediate *I*, which in turn produces $Fe^{\bullet+}$(IV)PPIX. The radical porphyrin species reacts with ABTS to form Fe(IV)PPIX=O and $ABTS^{\bullet+}$. $ABTS^{\bullet+}$ undergoes degradation, but not disproportionation. Fe(IV)PPIX=O reacts with a second molecule of ABTS to form $ABTS^{\bullet+}$ and regenerate Fe(III)PPIX, thus completing the main cycle. The secondary cycle is initiated by the complexation of ABTS to Fe(III)PPIX. The complex reacts with H_2O_2 to generate a $Fe^{\bullet+}$(IV)PPIX=O.ABTS complex. The radical porphyrin reacts with the ABTS molecule attached to it to release Fe(IV)PPIX=O and $ABTS^{\bullet+}$, which concludes the second cycle.

Consequently, the peroxidase-like cycle of Fe(III)PPIX has been studied thoroughly to present a reaction mechanism that best describes the kinetic data. Care was taken to analyse the differing models presented by research groups for the reaction of Fe(III)PPIX and H_2O_2, as well as the complete peroxidase-like cycle, in order

to give a conclusive analysis regarding model comparisons. Results on the effect of the chromogen on the peroxidase-like cycle kinetics and plausible side reactions such as Fe(IV)PPIX=O decay has been tested to yield a better understanding of the toxicity of Fe(III)PPIX. A full kinetic model regarding the peroxidase-like activity of Fe(III)PPIX reaction is presented.

Regarding the reaction between Fe(III)PPIX and H_2O_2, we used the model that fit the best with the least complexity. However, the fact remains that models 3(r)_original and 3(r)_rad can still be tested in the peroxidase-like cycle for comparison to the results of peroxidase-like cycle analysis using model 3(ir)_original, as the regression statistics obtained for these models indicate that they can explain the experimental results as well as explained by 3(ir)_original. Furthermore, the study of ABTS disproportionation under acidic conditions presented peculiar results. The isosbestic point that formed under highly acidic conditions can be further probed to elicit insight into the properties of ABTS. With the presenting of a peroxidase-like model that can explain the experimental data, an avenue for future work would be the comparison of the model parameters yielded by NLLS regression to a system incorporating relevant antimalarial compounds to gain insight into the mechanism by which these compounds may modulate the toxicity of the iron porphyrin moiety.

7. References

1 N. Tangpukdee, C. Duangdee, P. Wilairatana and S. Krudsood, *Korean J. Parasitol.*, 2009, **47**, 93–102.

2 Geneva: World Health Organization, *World malaria report 2017*, 2017.

3 F. K. Koussounda, S. Jeyaraj, C. N. Nguetse, C. N. Nkonganyi, K. C. Kokou, M. K. E. Beka and F. Ntoumi, *Malar. J.*, 2017, **16**, 1–7.

4 C. Naing, M. A. Whittaker, V. N. Wai and J. W. Mak, *PLoS Negl. Trop. Dis.*, 2014, **8**, e3701.

5 A. S. I. Aly, A. M. Vaughan and S. H. I. Kappe, *Annu. Rev. Microbiol.*, 2009, **63**, 195–221.

6 P. Sinnis, *Infect. Agents Dis.*, 1996, **5**, 182–9.

7 A. M. Vaughan and S. H. I. Kappe, *Cold Spring Harb. Perspect. Med.*, 2017, **7**, a025486.

8 A. S. Paul, E. S. Egan and M. T. Duraisingh, *Curr. Opin. Hematol.*, 2015, **22**, 220–226.

9 C. P. Nixon, *Hum. Vaccin. Immunother.*, 2016, **12**, 3189–3195.

10 A. Bartoloni and L. Zammarchi, *Mediterr. J. Hematol. Infect. Dis.*, 2012, **4**, 1–10.

11 World Health Organization, *Haemoglobin concentrations for the diagnosis of anaemia and assessment of severity*, 2011.

12 WHO Global Database on Anaemia, *Worldwide prevalence of anaemia 1993-2005*, 2008.

13 A. J. Marengo-Rowe, *Proc. (Bayl. Univ. Med. Cent).*, 2006, **19**, 239–245.

14 S. C. Oaks, V. S. Mitchell, G. W. Pearson and C. C. J. Carpenter, *Malaria: Obstacles and Opportunities*, National Academy Press, Washington DC, 1991.

15 M. Paoli, R. Liddington, J. Tame, A. Wilkinson and G. Dodson, *J. Mol. Biol.*, 1996, **256**, 775–792.

16 A. V Pandey, V. K. Babbarwal, J. N. Okoyeh, R. M. Joshi, S. K. Puri, R. L. Singh and V. S. Chauhan, *Biochem. Biophys. Res. Commun.*, 2003, **308**, 736–743.

17 S. E. Francis, D. J. Sullivan and D. E. Goldberg, *Annu. Rev. Microbiol.*, 1997, **51**, 97–123.

18 S. Kumar and U. Bandyopadhyay, *Toxicol. Lett.*, 2005, **157**, 175–188.

19 S. B. Brown, T. C. Dean and P. Jones, *Biochem. J.*, 1970, **117**, 741–744.

20 I. Solomonov, M. Osipova, Y. Feldman, C. Baehtz, K. Kjaer, I. K. Robinson, G. T. Webster, D. McNaughton, B. R. Wood, I. Weissbuch and L. Leiserowitz, *J. Am. Chem. Soc.*, 2007, **129**, 2615–2627.

21 Y. Zhu, T. Hon, W. Ye and L. Zhang, *Cell Growth Differ.*, 2002, **13**, 431–439.

22 Y. Zhu, T. Hon and L. Zhang, *Biochem. Biophys. Res. Commun.*, 1999, **258**, 87–93.

23 Y. Zhu, H. C. Lee and L. Zhang, *DNA Cell Biol.*, 2002, **21**, 333–346.

24 A. Sengupta, T. Hon and L. Zhang, *Brain Res. Mol. Brain Res.*, 2005, **137**, 23–30.

25 S. Sassa and T. Nagai, *Int. J. Hematol.*, 1996, **63**, 167–178.

26 B. Porstmann, T. Porstmann and E. Nugel, *J. Clin. Chem. Clin. Biochem.*, 1981, **19**, 435–439.

27 L. Zhang, *Heme Biology - The Secret Life of Heme in Regulating Diverse Biological Processes*, World Scientific Publishing, Singapore, 2011.

28 P. Ponka, *Am. J. Med. Sci.*, 1999, **318**, 241–256.

29 R. C. Wek, *Trends Biochem. Sci.*, 1994, **19**, 491–6.

30 H. Atamna, J. Liu and B. N. Ames, *J. Biol. Chem.*, 2001, **276**, 48410–48416.

31 I. Kimura, Y. Nakayama, M. Konishi, T. Kobayashi, M. Mori, M. Ito, A. Hirasawa, G. Tsujimoto, M. Ohta, N. Itoh and M. Fujimoto, *J. Neurochem.*, 2010, **112**, 1156–1167.

32 N. Wijayanti, N. Katz and S. Immenschuh, *Curr. Med. Chem.*, 2004, **11**, 981–986.

33 U. A. Meyer, M. M. Schuurmans and R. L. Lindberg, *Semin. Liver Dis.*, 1998, **18**, 43–52.

34 M. R. Moore, in *Tetrapyrroles*, Springer New York, New York, NY, 2009, pp. 1–28.

35 H. Atamna, *Ageing Res. Rev.*, 2004, **3**, 303–318.

36 H. M. Schipper, *Exp. Gerontol.*, 2000, **35**, 821–830.

37 H. M. Schipper, S. Cissé and E. G. Stopa, *Ann. Neurol.*, 1995, **37**, 758–768.

38 F. A. Wagener, H.-D. Volk, D. Willis, N. G. Abraham, M. P. Soares, G. J. Adema and C. G. Figdor, *Pharmacol. Rev.*, 2003, **55**, 551–571.

39 G. Balla, H. S. Jacob, J. W. Eaton, J. D. Belcher and G. M. Vercellotti, *Arterioscler. Thromb. a J. Vasc. Biol.*, **11**, 1700–1711.

40 S. W. Ryter and R. M. Tyrrell, *Free Radic. Biol. Med.*, 2000, **28**, 289–309.

41 J. M. Gutteridge and A. Smith, *Biochem. J.*, 1988, **256**, 861–865.

42 Y. Lavrovsky, C. S. Song, B. Chatterjee and A. K. Roy, *Mech. Ageing Dev.*, 2000, **114**, 49–60.

43 P. B. Letarte, K. Lieberman, K. Nagatani, R. A. Haworth, G. B. Odell and T. A. Duff, *J. Neurosurg.*, 1993, **79**, 252–255.

44 S. H. Vincent, *Semin. Hematol.*, 1989, **26**, 105–113.

45 T. H. Schmitt, W. A. Frezzatti and S. Schreier, *Arch. Biochem. Biophys.*, 1993, **307**, 96–103.

46 J. Balla, G. Balla, V. Jeney, G. Kakuk, H. S. Jacob and G. M. Vercellotti, *Blood*, 2000, **95**, 3442–3450.

47 A. van Langendonckt, F. Casanas-Roux, M.-M. Dolmans and J. Donnez, *Fertil. Steril.*, 2002, **77**, 561–570.

48 R. L. Aft and G. C. Mueller, *J. Biol. Chem.*, 1984, **259**, 301–305.

49 G. Camejo, C. Halberg, A. Manschik-Lundin, E. Hurt-Camejo, B. Rosengren, H. Olsson, G. I. Hansson, G. B. Forsberg and B. Ylhen, *J. Lipid Res.*, 1998, **39**, 755–766.

50 Y. Lavrovsky, M. L. Schwartzman, R. D. Levere, A. Kappas and N. G. Abraham, *Proc. Natl. Acad. Sci. U. S. A.*, 1994, **91**, 5987–5991.

51 F. A. Wagener, A. Eggert, O. C. Boerman, W. J. Oyen, A. Verhofstad, N. G. Abraham, G. Adema, Y. van Kooyk, T. de Witte and C. G. Figdor, *Blood*, 2001, **98**, 1802–1811.

52 S. M. H. Sadrzadeh, E. Graf, S. S. Panter, P. E. Hallawaysq and J. W. Eaton, *J. Biol. Chem.*, 1984, **259**, 14354–14356.

53 R. Tenhunen, H. S. Marver and R. Schmid, *J. Biol. Chem.*, 1969, **244**, 6388–6394.

54 C. Li and R. Stocker, *Redox Rep. Commun. Free Radic. Res.*, 2009, **14**, 95–101.

55 S. Shibahara, R. Muller, H. Taguchi and T. Yoshida, *Proc. Natl. Acad. Sci.*, 1985, **82**, 7865–7869.

56 V. F. Fairbanks, in *Manual of Clinical Hematology*, 2002, p. 17.

57 M. M. Chen, L. Shi and D. J. Sullivan, *Mol. Biochem. Parasitol.*, 2001, **113**, 1–8.

58 D. J. Sullivan, I. Y. Gluzman and D. E. Goldberg, *Sci. (New York)*, 1996, **271**, 219–22.

59 E. Hempelmann and H. M. Marques, *J. Pharmacol. Toxicol. Methods*, 1994, **32**, 25–30.

60 T. J. Egan, *J. Inorg. Biochem.*, 2007, **102**, 1288–1299.

61 E. Hempelmann, *Parasitol. Res.*, 2007, **100**, 671–676.

62 A. N. Hoang, K. K. Ncokazi, K. A. de Villiers, D. W. Wright and T. J. Egan, *Dalt. Trans.*, 2010, **39**, 1235–1244.

63 M. A. Ambele and T. J. Egan, *Malar. J.*, 2012, **11**, 1–13.

64 A. N. Hoang, R. D. Sandlin, A. Omar, T. J. Egan and D. W. Wright, *Biochemistry*, 2010, **49**, 10107–10116.

65 A. Dorn, S. R. Vippagunta, H. Matile, A. Bubendorf, J. L. Vennerstrom and R. G. Ridley, *Biochem. Pharmacol.*, 1998, **55**, 737–747.

66 C. D. Fitch, G. Cai, Y. Chen and J. D. Shoemaker, *Biochim. Biophys. Acta*, 1999, **1454**, 31–37.

67 J. M. Pisciotta, I. Coppens, A. K. Tripathi, P. F. Scholl, J. Shuman, S. Bajad, V. Shulaev and D. J. Sullivan, *Biochem. J.*, 2007, **402**, 197–204.

68 S. Kapishnikov, A. Weiner, E. Shimoni, P. Guttmann, G. Schneider and N. Dahan-pasternak, *Proc. Natl. Acad. Sci.*, 2012, **109**, 11188–11193.

69 D. Jani, R. Nagarkatti, W. Beatty, R. Angel, C. Slebodnick, J. Andersen, S. Kumar and D.

Rathore, *PLoS Pathog.*, 2008, **4**, e1000053.

70 A. Brausam, S. Eigler, N. Jux and R. van Eldik, *Inorg. Chem.*, 2009, **48**, 7667–7678.

71 N. Abu Bakar, N. Klonis, E. Hanssen, C. Chan and L. Tilley, *J. Cell Sci.*, 2010, **123**, 441–450.

72 N. Klonis, O. Tan, K. Jackson, D. Goldberg, M. Klemba and L. Tilley, *Biochem. J.*, 2007, **407**, 343–354.

73 M. F. Zipplies, W. A. Lee and T. C. Bruice, *J. Am. Chem. Soc.*, 1986, **108**, 4433–4445.

74 M. C. de Almeida Ribeiro, O. Augusto and A. M. da Costa Ferreira, *J. Chem. Soc. Dalt. Trans.*, 1995, **23**, 3759–3766.

75 M. Foley and L. Tilley, *Pharmacol. Ther.*, 1998, **79**, 55–87.

76 P. Loria, S. Miller, M. Foley and L. Tilley, *Biochem. J.*, 1999, **339**, 363.

77 M. C. D. A. Ribeiro, O. Augusto and A. M. D. C. Ferreira, *J. Inorg. Biochem.*, 1997, **65**, 15–23.

78 M.-M. Mesulam, *J. Histochem. Cytochem.*, 1976, **24**, 1273–1280.

79 M.-M. Mesulam, *J. Histochem. Cytochem.*, 1978, **26**, 106–117.

80 ATSDR, *Toxicological Profile for Benzidine*, 2001.

81 B. Branchi, C. Galli and P. Gentili, *Org. Biomol. Chem.*, 2005, **3**, 2604–2614.

82 Sigma, *o-Dianisidine dihydrochloride product information*, 1976, vol. 837.

83 E. A. Shalaby and S. M. M. Shanab, *Indian J. Geo-Marine Sci.*, 2013, **42**, 556–564.

84 B. Ou, D. Huang, M. Hampsch-Woodill, J. A. Flanagan and E. K. Deemer, *J. Agric. Food Chem.*, 2002, **50**, 3122–3128.

85 L. Cerretani and A. Bendini, in *Olives and olive oil in health and disease prevention*, Elsevier Inc., 2010, p. 625 635.

86 M. Drozd, M. Pietrzak, J. Pytlos and E. Malinowska, *Anal. Chim. Acta*, 2016, **948**, 80–89.

87 PubChem, Structures of chromogens discussed, https://pubchem.ncbi.nlm.nih.org.

88 B. S. Wolfenden and R. S. Willson, *J. Chem. Soc. Perkin Trans.*, 1982, **2**, 805–812.

89 N. J. Miller, C. Rice-evans, M. Davies, V. Gopinathan and A. Milner, *Clin. Sci.*, 1993, **84**, 407–412.

90 M. A. Turnbow and C. W. Garner, *BioFeedback*, 1993, **15**, 271–273.

91 A. Cano, J. Hernandez-Ruiz, F. Garcia-Canovas, M. Acosta and M. B. Arnao, *Phytochem. Anal.*, 1998, **9**, 196–202.

92 C. J. Sammy, Thesis, *Investigations into the Peroxidase Activity of Ferriprotoporphyrin IX and its Complexes with Clinically Relevant Antimalarial Drugs*, Stellenbosch, 2017.

93 A. Brausam, S. Eigler, N. Jux and R. van Eldik, *Inorg. Chem.*, 2009, **48**, 7667–7678.

94 R. E. Childs and W. G. Bardsley, *Biochem. J.*, 1975, **145**, 93–103.

95 J. Janata and M. B. Williams, *J. Phys. Chem.*, 1972, **76**, 1178–1183.

96 A. F. G. Slater, *Pharmacol. Ther.*, 1993, **57**, 203–235.

97 A. Dorn, R. Stoffel, H. Matile, A. Bubendorf and R. G. Ridley, *Nature*, 1995, **374**, 269–271.

98 A. F. G. Slater and A. Cerami, *Nature*, 1992, **355**, 167–169.

99 P. B. Macomber, H. Sprinz and A. J. Tousimis, *Nature*, 1967, **214**, 937–939.

100 D. C. Warhurst and S. Gould, *Ann. Trop. Med. Parasitol.*, 1982, **76**, 257–264.

101 A. Yayon, Z. I. Cabantchik and H. Ginsburg, *Proc. Natl. Acad. Sci. U. S. A.*, 1985, **82**, 2784–2788.

102 C. A. Homewood, D. C. Warhurst, W. Peters and V. C. Baggaley, *Nature*, 1972, **235**, 50–52.

103 T. J. Egan, D. C. Ross and P. A. Adams, *FEBS Lett.*, 1994, **352**, 54–57.

104 S. Moreau, B. Perly, C. Chachaty and C. Deleuze, *Biochim. Biophys. Acta*, 1985, **840**, 107–116.

105 D. Balasubramanian, C. M. Rao and B. Panijpan, *Science (80-.).*, 1984, **223**, 828–830.

106 A. C. de Dios, R. Tycko, L. M. B. Ursos and P. D. Roepe, *J. Phys. Chem.*, 2003, **107**, 5821–5825.

107 A. Leed, K. DuBay, L. M. B. Ursos, D. Sears, A. C. de Dios and P. D. Roepe, *Biochemistry*, 2002, **41**, 10245–10255.

108 L. B. Casabianca, D. An, J. K. Natarajan, J. N. Alumasa, P. D. Roepe, C. Wolf and A. C. de Dios, *Inorg. Chem.*, 2008, **47**, 6077–6081.

109 J. N. Alumasa, A. P. Gorka, L. B. Casabianca, E. Comstock, A. C. de Dios and P. D. Roepe, *J. Inorg. Biochem.*, 2011, **105**, 467–475.

110 A. C. de Dios, L. B. Casabianca, A. Kosar and P. D. Roepe, *Inorg. Chem.*, 2004, **43**, 8078–8084.

111 J. Gildenhuys, T. Le Roux, T. J. Egan and K. A. De Villiers, *J. Am. Chem. Soc.*, 2013, **135**, 1037–1047.

112 D. J. Sullivan, I. Y. Gluzman, D. G. Russell and D. E. Goldberg, *Proc. Natl. Acad. Sci. U. S. A.*, 1996, **93**, 11865–70.

113 A. V Pandey, H. Bisht, V. K. Babbarwal, K. C. Pandey and V. S. Chauhan, *Biochem. J.*, 2001, **355**, 333–338.

114 S. R. Meshnick, *Int. J. Parasitol.*, 2002, **32**, 1655–1660.

115 A. Brossi, B. Venugopalan, L. Dominguez Gerpe, H. J. Yeh, J. L. Flippen-Anderson, P. Buchs, X. D. Luo, W. Milhous and W. Peters, *J. Med. Chem.*, 1988, **31**, 645–50.

116 A. R. Butler, B. C. Gilbert, P. Hulme, L. R. Irvine, L. Renton and A. C. Whitwood, *Free Radic.*

Res., 1998, **28**, 471–6.

117 S. R. Meshnick, Y. Z. Yang, V. Lima, F. Kuypers, S. Kamchonwongpaisan and Y. Yuthavong, *Antimicrob. Agents Chemother.*, 1993, **37**, 1108–14.

118 M. D. Scott, S. R. Meshnick, R. A. Williams, D. T. Chiu, H. C. Pan, B. H. Lubin and F. A. Kuypers, *J. Lab. Clin. Med.*, 1989, **114**, 401–6.

119 N. Wei and S. M. Sadrzadeh, *Biochem. Pharmacol.*, 1994, **48**, 737–41.

120 P. A. Berman and P. A. Adams, *Free Radic. Biol. Med.*, 1997, **22**, 1283–8.

121 G. H. Posner, D. Wang, J. N. Cumming, C. H. Oh, A. N. French, A. L. Bodley and T. A. Shapiro, *J. Med. Chem.*, 1995, **38**, 2273–5.

122 M. Wittner, J. Lederman, H. B. Tanowitz, G. S. Rosenbaum and L. M. Weiss, *Am. J. Trop. Med. Hyg.*, 1996, **55**, 219–22.

123 Y. L. Hong, Y. Z. Yang and S. R. Meshnick, *Mol. Biochem. Parasitol.*, 1994, **63**, 121–8.

124 P. A. Adams and P. A. Berman, *J. Pharm. Pharmacol.*, 1996, **48**, 183–187.

125 M. Chugh, V. Sundararaman, S. Kumar, V. S. Reddy, W. A. Siddiqui, D. S. Kenneth and P. Malhotra, *Proc. Natl. Acad. Sci.*, 2013, **110**, 5392–5397.

126 J. Wang, C.-J. Zhang, W. N. Chia, C. C. Y. Loh, Z. Li, Y. M. Lee, Y. He, L.-X. Yuan, T. K. Lim, M. Liu, C. X. Liew, Y. Q. Lee, J. Zhang, N. Lu, C. T. Lim, Z.-C. Hua, B. Liu, H.-M. Shen, K. S. W. Tan and Q. Lin, *Nat. Commun.*, 2015, **6**, 10111.

127 J. Achan, A. O. Talisuna, A. Erhart, A. Yeka, J. K. Tibenderana, F. N. Baliraine, P. J. Rosenthal and U. D'Alessandro, *Malar. J.*, 2011, **10**, 1–12.

128 R. N. Price, A. C. Uhlemann, A. Brockman, R. McGready, E. Ashley, L. Phaipun, R. Patel, K. Laing, S. Looareesuwan, N. J. White, F. Nosten and S. Krishna, *Lancet*, 2004, **364**, 438–447.

129 A. B. S. Sidhu, D. Verdier-Pinard and D. A. Fidock, *Science (80-.).*, 2002, **298**, 210–213.

130 S. A. Peel, P. Bright, B. Yount, J. Handy and R. S. Baric, *Am. J. Trop. Med. Hyg.*, 1994, **51**, 648–658.

131 J. D. Sewry and M. E. Brown, *Thermochim. Acta*, 2002, **390**, 217–225.

132 G. Puxty, M. Maeder and K. Hungerbühler, *Chemom. Intell. Lab. Syst.*, 2006, **81**, 149–164.

133 A. de Juan and R. Tauler, *Crit. Rev. Anal. Chem.*, 2006, **36**, 163–176.

134 K. P. Burnham and D. R. Anderson, *Model Selection and Multimodel Inference: A Practical Information-Theoretic Approach*, Springer-Verlag, New York, 2nd edn., 1998.

135 S. Norman and M. Maeder, *Crit. Rev. Anal. Chem.*, 2006, **36**, 199–209.

136 J. R. Knutson, J. M. Beechem and L. Brand, *Chem. Phys. Lett.*, 1983, **102**, 501–507.

137 M. Meloun, S. Bordovská, T. Syrový and A. Vrána, *Anal. Chim. Acta*, 2006, **580**, 107–121.

138 P. Kuzmič, *Anal. Biochem.*, 1996, **237**, 260–273.

139 MathWorks, MatLab R2018b, https://www.mathworks.com/help/matlab/ref/rand.html.

140 J. A. Nelder and R. Mead, *Comput. J.*, 1965, **7**, 308–313.

141 L. Thøgersen, J. Olsen, D. Yeager, P. Jørgensen, P. Salek and T. Helgaker, *J. Chem. Phys.*, 2004, **121**, 16–27.

142 J. E. Dennis and R. B. Scnabel, *Numerical methods for unconstrained optimization and nonlinear equations*, SIAM, 2007, vol. 136.

143 D. W. Marquardt, *J. Soc. Ind. Appl. Math.*, 1963, **11**, 431–441.

144 J. A. L. Kenneth V. Price, Rainer M. Storn, *Differential Evolution: A Practical Approach to Global Optimization*, Springer-Verlag, 2005, vol. 53.

145 D. Brynn Hibbert and P. Thordarson, *Chem. Commun.*, 2016, **52**, 12792–12805.

146 D. Vina, E. Uriarte, F. Orallo and H. Gonzalez-Diaz, *Mol. Pharm.*, 2009, **6**, 825–835.

147 Y. S. Ho, *Carbon N. Y.*, 2004, **42**, 2115–2116.

148 S. Kullback and R. A. Leibler, *Annu. Math. Stat.*, 1951, **22**, 79–86.

149 J. I. Myung, Y. Tang and M. A. Pitt, *Methods Enzymol.*, 2009, **454**, 287–304.

150 J. I. Myung and M. A. Pitt, *Methods Enzymol.*, 2004, **383**, 351–66.

151 R. Horn, *Biophys. J.*, 1987, **51**, 255–263.

152 D. Posada and T. R. Buckley, *Syst. Biol.*, 2004, **53**, 793–808.

153 D. R. Anderson, K. P. Burnham and W. L. Thompson, *J. Wildl. Manage.*, 2000, **64**, 912–923.

154 H. Akaike, *J. Econom.*, 1981, **16**, 3–14.

155 D. R. Cox and N. Reid, *The Theory of the Design of Experiments*, Chapman & Hall/CRC, New York, 2000.

156 D. Simberloff, *Am. Soc. Nat.*, 1983, **122**, 626–635.

157 B. Meunier, *Chem. Rev.*, 1992, **92**, 1411–1456.

158 H. K. Baek and H. E. van Wart, *Biochemistry*, 1989, **28**, 5714–5719.

159 P. Jones, D. Mantle and I. Wilson, *J. Chem. Soc. Dalt. Trans.*, 1983, **17**, 161.

160 T. C. Bruice, M. F. Zipplies and W. A. Lee, *Proc. Natl. Acad. Sci.*, 1986, **83**, 4646–4649.

161 T. Tatsuma and T. Watanabe, *Anal. Chem.*, 1991, **63**, 1580–1585.

162 S. B. Brown, T. C. Dean and P. Jones, *Biochem. J.*, 1970, **117**, 733–739.

163 P. Jones, *J. Biol. Chem.*, 2001, **276**, 13791–13796.

164 K. de Villiers, C. H. Kaschula, T. J. Egan and H. M. Marques, *J. Biol. Inorg. Chem.*, 2007, **12**,

101–117.

165 C. Asher, K. A. De Villiers and T. J. Egan, *Inorg. Chem.*, 2009, **48**, 7994–8003.

166 B. Brown, H. Hatzikonstantinou and D. G. Herries, *Int. J. Biochem.*, 1980, **12**, 701–707.

167 J. Keilin, *Biochem. J.*, 1955, **59**, 571–579.

168 P. A. Adams, *J. Chem. Soc. Perkin Trans.*, 1990, **2**, 1407–1414.

169 T. L. Brown, H. E. Lemay, B. E. Bursten, C. J. Murphy, S. J. Langford and D. S. Sagatys, *Chemistry, The Central Science: A Broad Perspective*, Pearson Australia, 2nd edn., 2010.

170 T. Engel and P. Reid, *Thermodynamics: Statistical Thermodynamics and Kinetics*, Pearson Prentice Hall, 2nd edn., 2010.

171 S. L. Scott, W.-J. Chen, A. Bakac and J. H. Espenson, *J. Phys. Chem.*, 1993, **97**, 6710–6714.

172 R. K. Haynes, K. Cheu, H. Chan, H. Wong, K. Li, M. M. Tang, M. Chen, Z. Guo, Z. Guo and K. Sinniah, *ChemMedChem*, 2012, **7**, 2204–2226.

173 P. Atkins, *Physical Chemistry*, WH Freeman and Company, New York, 6th edn., 1997.

174 Y. Song, J. Jiang, J. Ma, S. Y. Pang, Y. Z. Liu, Y. Yang, C. W. Luo, J. Q. Zhang, J. Gu and W. Qin, *Environ. Sci. Technol.*, 2015, **49**, 11764–11771.

Addendum:

File – run.m

```
load abts1 % load the datasets

global time absorbance k ext iconc steps coamount rcamount hop
% declare variables present in different script files with single values

time=abts1(:,1);
absorbance=abts1(:,2);
steps=length(time);
timevariables % calls on script file with name timevariables.m to run
iconc=[]; % initial concentration

coamount= % amount of species ;
rcamount= % amount of rate constants ;
k=zeros(1,rcamount);
ext=zeros(1,coamount);

k=[ % insert rate constant guesses here ];
ext= [ % insert extinction coefficient guesses here ];
iconc= [ % insert initial reagent concentrations here ];

bobo=0;
hop=0;

while 1
        simplex % calls on simplex.m file
        hop=hop+1;
        bobo=bobo+1;
        % hop and bobo ensure that the first fit is for rate constants only
        % followed by the turnwise fitting of rate constants and extinction
        % coefficients
        if bobo>=2
            break
        end
end
```

File – timevariables.m

```
global time tspan
tstart=time(1);
tend=time(end);
tint=time(end)-time(end-1);
tspan=tstart:tint:tend;
% declare all relevant time related variables
```

File – simplex.m

```
%% general constants and setup

global absorbance ext k rateconstants rcODE coamount rcamount steps ordrc rcnew hop
tspan iconc


rateconstants=zeros(rcamount+1,rcamount);
S=zeros(steps,coamount);
Sabs=zeros(steps,coamount); % Absorbance matrix
lsqSS=zeros(rcamount+1,1); % SSQ matrix
alpha=1;
gamma=2;
rho=0.5;
sigma=0.5;

options=odeset('RelTol',1e-12,'AbsTol',1e-15); % ODE tolerances


%determine rate constant sets, or vertices of simplex
rateconstants(1,:)=k;
for n=2:1:(rcamount+1)
    for m=1:1:rcamount
        rateconstants(n,m)=rateconstants(n-1,m)+0.021*rand(1)*rateconstants(n-1,m);
    end
end

%determine least squares for rate constant sets generated
for n=1:1:(rcamount+1)
    for m=1:1:rcamount
        rcODE(m)=rateconstants(n,m);
    end
    [~,calc_conc]=ode23t('abc',tspan,iconc,options);
     % abc.m contains the ODEs to be solved
    for i=1:1:coamount
        for j=1:1:steps
            S(j,i)=calc_conc(j,i)*ext(i);
        end
    end
    Sabs=sum(S,2);
    lsqSS(n,1)=sum((absorbance-Sabs).^2);
    S=zeros(steps,coamount);
    Sabs=zeros(steps,1);
end

%create matrix containing lsq values and corrosponding rate constants
rclsqexp=zeros(rcamount+1,rcamount+1);
rclsqexp(:,1)=lsqSS;
for n=1:1:rcamount
    for m=1:1:rcamount+1
        rclsqexp(m,n+1)=rateconstants(m,n);
    end
end
ordrc=sortrows(rclsqexp); % put best first and worst last

%set endpoint value for simplex loop
ender=zeros(1,rcamount);
for n=1:1:rcamount
```

```
    ender(n)=0.5;
end
sobo=0;
%% loop
while ender>0
    %% first insert testfit conditions and recalculate least squares

    ordrc=sortrows(ordrc);
    rcnew=ordrc(1,2:end); % best current rate constants
    if hop>0
       sobo=sobo+1;
       iterate=rem(sobo,2);
        if iterate>0
            fitsima
            % calls on fitsima.m file for extinction coefficient refinement

            % need to recalculate SSQ for each rate constant set using
            % the refined extinction coefficients
            for n=1:1:(rcamount+1)
                for m=1:1:rcamount
                    rcODE(m)=ordrc(n,m+1);
                end
                [~,calc_conc]=ode23t('abc',tspan,iconc,options);
                for i=1:1:coamount
                    for j=1:1:steps
                        S(j,i)=calc_conc(j,i)*ext(i);
                    end
                end
                Sabs=sum(S,2);
                lsqSS(n,1)=sum((absorbance-Sabs).^2);
                S=zeros(steps,coamount);
                Sabs=zeros(steps,1);
            end
            ordrc(:,1)=lsqSS;
        end
    end

    %% for break criteria
    countrc=0;
    for n=1:1:rcamount
        if ender(n)>0.9999
            if ender(n)<1.0001
                countrc=countrc+1;
            end
        end
    end

    if countrc>=rcamount % if refinement is complete
       break
    end
    if sobo>=100000 % if process takes too long
        break
    end

    for n=1:1:rcamount
        ender(n)=0.5;
    end


    %% next determine new points to be considered
```

```
cent=zeros(rcamount,rcamount);
for n=1:1:rcamount
    for m=1:1:rcamount
        cent(n,m)=ordrc(n,m+1);
    end
end
centroid=sum(cent)/(rcamount);
lsqSP=zeros(2+rcamount,1);



%reflection
reflect=centroid+alpha*(centroid-ordrc(end,2:end));
for n=1:1:rcamount
    if reflect(n)<0
        reflect(n)=rand()*1.0;
    end
end
rcODE=reflect;
[~,calc_conc]=ode23t('abc',tspan,iconc,options);
for i=1:1:coamount
    for j=1:1:steps
        S(j,i)=calc_conc(j,i)*ext(i);
    end
end
sabs=sum(S,2);
lsqSP(1)=sum((absorbance-sabs).^2);
sabs=zeros(steps,1);S=zeros(steps,coamount);
if lsqSP(1)<ordrc(end,1)
    %second worst

        %best
        ender=reflect./ordrc(end,2:end);
        ordrc(end,1)=lsqSP(1);
        ordrc(end,2:end)=reflect;
        continue

end







%contraction
contract=centroid+rho*(ordrc(end,2:end)-centroid);
rcODE=contract;
[~,calc_conc]=ode23t('abc',tspan,iconc,options);
for i=1:1:coamount
    for j=1:1:steps
        S(j,i)=calc_conc(j,i)*ext(i);
    end
end
sabs=sum(S,2);
lsqSP(2)=sum((absorbance-sabs).^2);
sabs=zeros(steps,1);S=zeros(steps,coamount);

    if lsqSP(2)<ordrc(end,1)
```

```
            ender=contract./ordrc(end,2:end);
            ordrc(end,1)=lsqSP(2);
            ordrc(end,2:end)=contract;
            continue
        end



    %shrinking
    shrink=zeros(rcamount,rcamount);
    for n=1:1:rcamount
        for m=1:1:rcamount
            shrink(n,m)=ordrc(1,m+1)+sigma*(ordrc(n+1,m+1)-ordrc(1,m+1));
        end
    end
    for n=1:1:rcamount
        rcODE=shrink(n,:);
        [~,calc_conc]=ode23t('abc',tspan,iconc,options);
        for i=1:1:coamount
            for j=1:1:steps
                S(j,i)=calc_conc(j,i)*ext(i);
            end
        end
        sabs=sum(S,2);
        lsqSP(2+n)=sum((absorbance-sabs).^2);
        sabs=zeros(steps,1);S=zeros(steps,coamount);
    end
    enders=zeros(rcamount);
    if lsqSP(1)>=ordrc((end-1),1)
        if lsqSP(2)>=ordrc(end,1)
            for n=1:1:rcamount
                enders(n,:)=shrink(n,:)./ordrc(n+1,2:end);
            end
            ender=sum(enders)/rcamount;
            ordrc(2:end,1)=lsqSP(3:end);
            ordrc(2:end,2:end)=shrink;
        end
    end


end

rcnew=sum(ordrc(:,2:(rcamount+1)))/(rcamount+1);
lsqs=sum(ordrc(:,1))/(rcamount+1);
```

File – abc.m

```
%% MODEL PROPOSAL Example:

% Hm --> heme
% Per --> hydrogen peroxide
% C1 --> heme-peroxide complex
% C2 --> porphyrin radical
% ABTS  --> 2,2'-Azinobis-(3-ethylbenzothiazoline-6-sulphonate)
% ABTSr --> ABTS radical
% D  --> degraded products
```

```
% Hm + Per <--> C1 --> C2
% C2 + 2ABTS --> Hm + 2ABTSr
% ABTSr --> D
% thus

function dydt=abc(ab,b)
global rcODE

Hm    = b(1);
Per   = b(2);
C1    = b(3);
C2    = b(4);
ABTS  = b(5);
ABTSr = b(6);


dydt =  [-Hm.Per.rcODE(1)+C1.rcODE(2)+C2.ABTS^2.rcODE(4)
         -Hm.Per.rcODE(1)+C1.rcODE(2)
         Hm.Per.rcODE(1)-C1.rcODE(2)-C1.rcODE(3)
         C1.rcODE(3)-C2.ABTS^2.rcODE(4)
         -C1.ABTS^2.rcODE(4)
         -ABTSr.rcODE(5)];
end
```

File – fitsima.m

```
global rcnew ext time absorbance steps coamount rcODE conc

% use conc in fitting function 'testext'
rcODE=rcnew;
options=odeset('RelTol',1e-11,'AbsTol',1e-12);

[~,calc_conc]=ode23t('abc',tspan,iconc,options);
conc=zeros(steps,coamount);

for n=1:1:coamount
    conc(:,n)=calc_conc(:,n);
end

lb=[0 0 0]; % set lower bound
up=[100000 2 100000]; % set upper bound

opts=optimset('Display','off'); % turn off reporting a message for every iteration
calc_ext=lsqcurvefit('testext',ext,time,absorbance,lb,up,opts);
% calc_ext calls testext.m file

ext=calc_ext; % new refined extinction coefficients
```

File – testext.m

```
function F=testext(x,t)
```

```
global time ext conc coamount steps

time=t;
ext=x;

E=zeros(steps,coamount);

for n=1:1:coamount
    for m=1:1:steps
        E(m,n)=conc(m,n)*ext(n);
    end
end
F=sum(E,2);
% F is the function used to refine extinction coefficients
```